

<b>REPORT DOCUMENTATION PAGE</b>			Form Approved OMB NO. 0704-0188	
Public Reporting burden for this collection of information is estimated to average 1 hour per response, including the time for reviewing instructions, searching existing data sources, gathering and maintaining the data needed, and completing and reviewing the collection of information. Send comment regarding this burden estimates or any other aspect of this collection of information, including suggestions for reducing this burden, to Washington Headquarters Services, Directorate for information Operations and Reports, 1215 Jefferson Davis Highway, Suite 1204, Arlington, VA 22202-4302, and to the Office of Management and Budget, Paperwork Reduction Project (0704-0188,) Washington, DC 20503.				
1. AGENCY USE ONLY (Leave Blank)		2. REPORT DATE 30. April. 2004		3. REPORT TYPE AND DATES COVERED Final Progress Report 1. April 2000 – 30 Sep 2003
4. TITLE AND SUBTITLE Search for plasma instability driven THz radiation source			5. FUNDING NUMBERS DAAD 19-00-1-0121	
6. AUTHOR(S) E. Gomik, G. Strasser, R. Zobl, M. Coquelin, M. Kast				
7. PERFORMING ORGANIZATION NAME(S) AND ADDRESS(ES) Institut für Festkörperphysik Technische Universität Wien Floragasse 7, A-1040 Wien Austria			8. PERFORMING ORGANIZATION REPORT NUMBER E 362/5	
9. SPONSORING / MONITORING AGENCY NAME(S) AND ADDRESS(ES)  U. S. Army Research Office P.O. Box 12211 Research Triangle Park, NC 27709-2211			10. SPONSORING / MONITORING AGENCY REPORT NUMBER  41118.2-PH	
11. SUPPLEMENTARY NOTES The views, opinions and/or findings contained in this report are those of the author(s) and should not be construed as an official Department of the Army position, policy or decision, unless so designated by other documentation.				
12 a. DISTRIBUTION / AVAILABILITY STATEMENT  Approved for public release; distribution unlimited.			12 b. DISTRIBUTION CODE	
13. ABSTRACT (Maximum 200 words) A novel concept for the generation of Terahertz generation based on current driven plasma instabilities in low-dimensional semiconductor quantum structures was investigated. The design principle is the combination of a step potential quantum well with a resonant tunneling diode, grown by MBE in the AlGaAs/GaAs material system. The interplay of heavy vertical current injection into the step well region with fast carrier extraction by the RTD is intended to create a partial population inversion in the electron distribution leading to the energetic resonance of two plasmon modes in the stepwell i.e. plasma instability. Intersubband emission around $100 \text{ cm}^{-1}$ was first observed on a single step quantum well structure. Modifications on the doping, injector region, barrier thickness, well shape and material system were then extensively studied to optimize the radiation output. A direct proof of the proposed plasmon generation process was the observation of an additional current peak mediated by resonant plasmon emission in resonant tunneling diodes with long emitter drift regions. A cascading of the active cells ranging from a fivefold repetition up to 30 stages was finally implemented to maximize the emission. Finally plasma instability mediated emission was identified in samples consisting of 10 and 30 cascades.				
14. SUBJECT TERMS plasma instability THz sources  semiconductor quantum structures			15. NUMBER OF PAGES 73	
			16. PRICE CODE	
17. SECURITY CLASSIFICATION OR REPORT UNCLASSIFIED	18. SECURITY CLASSIFICATION ON THIS PAGE UNCLASSIFIED	19. SECURITY CLASSIFICATION OF ABSTRACT UNCLASSIFIED	20. LIMITATION OF ABSTRACT  UL	

NSN 7540-01-280-5500

Standard

Form 298 (Rev.2-89)

Prescribed by ANSI Std. Z39-18

# **SEARCH FOR PLASMA INSTABILITY DRIVEN THZ-SOURCE**

## **Final Progress Report**

**E. Gornik, G. Strasser, M. Kast, C. Pacher, M. Coquelin, R.Zobl**

**May, 2004**

## **U.S. ARMY RESEARCH OFFICE**

**CONTRACT NO /GRANT NUMBER: DAAD 19-00-1-0121**

**ARO proposal Nr. 411118-PH**

**INSTITUT FÜR FESTKÖRPERELEKTRONIK, TECHNISCHE  
UNIVERSITÄT WIEN, AUSTRIA**

**APPROVED FOR PUBLIC RELEASE;**

**DISTRIBUTION UNLIMITED**

The views, opinions, and/or findings contained in this report are those of the authors and should not be construed as an official department of the army position, policy, or decision, unless so designed by other documentation.

# Summary

The main goal of the project is the realization of semiconductor devices for the emission of coherent THz radiation. The novel concept is based on radiation emission from a current driven plasma instability (PI) in a confined plasma. The main advantage of this collective phenomenon is the lacking of a need of an optical feedback resonator. Therefore such devices are promising candidates for high power Terahertz sources operating up to very high temperatures due to the intrinsic robustness of the electrically excited plasmons against various scattering mechanisms.

The basic structure is realised in the AlGaAs/GaAs material system and consists of the combination of a step quantum well with a resonant tunnel diode (RTD): a high carrier density in the wide area of the step potential well realizes an efficient plasmon resonator. A deep narrow region of the well is designed to contain at least three quantized energy levels. Heavy vertical current injection in the upper level together with fast electron extraction from the middle level by the RTD is aimed to achieve partial population inversion in the structure as a prerequisite for a plasma instability.

Due to the complex nature of the concept a twofold approach was chosen for the experimental approach: on the one hand samples were grown to directly induce the PI effect, on the other hand structures were designed to isolate and investigate separately specific features of the PI concept.

It is demonstrated that confined plasmons can be excited by current injection in parabolically graded wells. The collective nature of the emitted farinfrared radiation proofs the concept of depolarization shift which is a cornerstone of the PI concept.

It is further shown that several plasmon types can coexist in low-dimensional structures and that their interaction is in agreement with the theory (e.g. the Kohn theorem)

The cascading of the unit cell is an efficient way for increasing the weak radiation output. More complex potential structures like parabolas and semiparabolas have been cascaded and exhibit FIR emission from a vertically injected current.

The application of an external magnetic field strongly reduces the effects of Auger-type electron-electron scattering in cascaded structures thus helping to achieve and increase population inversion in vertical injection schemes.

No experimental results are available so far about a plasma instability phenomenon in semiconductors prior to this project. A plasma effect in the current signature of a resonant tunneling diode structure has clearly been identified: an additional current peak from plasmon assisted tunneling is an indication of the onset of a plasma instability phenomenon.

A first success was the detection of Terahertz emission stemming from intersubband transition in the original a plasma instability design, i.e. the single step quantum well + RTD. The actual effectiveness of the generation process and the competing non radiative relaxation channels are not really known. Very large emissive areas were processed and

measured due to very small emission signals. In large size samples the homogeneity of the current distribution is often lost. Non-ohmic features are washed out and current resonances are only visible by the derivatives of the measured IVs.

In the following many different design modifications (doping, injector region, tunneling barrier thickness, potential shape, material system) were investigated experimentally.

Cascading was finally adopted to increase FIR radiation output, starting with a fivefold repeated structure up to structures incorporating 30 cascaded steps.

To reach plasmon instability enhanced emission in more suitable range different approaches were followed. On the one hand the doping was softly reduced and design was changed, compared to previous structures, to reach this effect from the high current side. This approach lead to samples with two significant emission peaks. One could be identified as free carrier emission from the 2DEG. The second peak was caused by intersubband emission. A plasmon induced growth rate could not be found. On the other hand low doped and cascaded samples with significantly changed “unit cells”, based on different material systems, were grown, to reach this effect from the low current density side.

A significant improvement was reached due to use InGaAs instead of GaAs in the active region and GaAs instead of AlGaAs as drift region. A 10 cascade structure based on this material system showed an emission peak, which was shifted to higher energies with increasing bias and bias values could be found where the emission width got sharper due to a positive growth rate. This effect could be verified with a regrowth of this sample including 30 cascades. A clear tuning and resonant behaviour of the subband resonance was found for different samples as a function of current. While the emission intensity increases, the linewidth decreases and the energy position shows a constant value in the resonant situation. These results give for the first time a clear experimental evidence for the appearance of a plasma instability in agreement with theoretical predictions from the Boston College group.

## List of Publications

J.Ulrich, R.Zobl, K.Unterrainer, G.Strasser, E.Gornik, K.D.Maranowski, and A.C.Gossard; "Temperature Dependence of Far-infrared Electroluminescence in Parabolic Quantum Wells"; *Appl.Phys.Lett.***74**, 3158 (1999).

A.Scorupsky, C.G.Du, G.Feng, R.Zobl, G.Strasser, C.Rauch, C.Pacher, K.Unterrainer, and E.Gornik; "Plasmon-based Terahertz Emission from Quantum Well Structures"; *Appl.Phys.Lett.***75**, 1685 (1999).

R. Zobl, K. Unterrainer, G. Strasser, E. Gornik, "Magneto-optical Terahertz Emission from Plasmons in Parabolic Quantum Wells"; *Semicond. Sci. and Technol.* **15**, 315 (2000).

J. Ulrich, R. Zobl, K. Unterrainer, G. Strasser, E. Gornik; "Magnetic Field Enhanced Quantum Cascade Emission"; *Appl. Phys. Lett.* **76**, 19 (2000)

K. Kempa, E. Gornik, K. Unterrainer, M. Kast, and G. Strasser, "Resonant Tunneling Mediated by Resonant Emission of Intersubband Plasmons", *Phys. Rev. Lett.* **86**, 2850 (2001)

K. Kempa, Y. Zhou, J. R. Engelbrecht, P. Bakshi, H. I. Ha, J. Moser, M. J. Naughton, J. Ulrich, G. Strasser, E. Gornik, and K. Unterrainer, "Intersubband Transport in Quantum Wells in Strong Magnetic Fields Mediated by Single- and Two-Electron Scattering" *Phys. Rev. Lett.* **88**, 226803 (2002)

M. Coquelin, R. Zobl, G. Strasser, E. Gornik, P.Bakshi, K.Kempa, " Experimental observation of plasma instability in semiconductor heterostructures" to be published

## PhD Theses

R. Zobl, Far-infrared Emission from Plasmons in Semiconductor Quantum Structures (PhD Thesis, TU Wien, March 2002)

M. Coquelin (PhD Thesis, TU Wien, in progress)

## Reports

Report E 362/1 Technical Report

Report E362/2 Final Progress Report

Report E362/3 Interim Progress Report

Report E362/4 Interim Progress Report

## List of participating Scientific Personal

Prof.. Dr. E. Gornik: Principal Investigator

Dr. K. Unterrainer, Dr. G. Strasser: Research Associates

R. Zobl, M. Coquelin, M. Kast:PhD students

# Contents

## Introduction

Foreword.....	5
Aim of the project.....	5
Previous accomplishments.....	7
The building steps for plasma instability.....	9

## Experimental Part 1: general aspects

The intersubband resonance plasmon and the depolarization shift.....	10
Parabolically graded plasmon resonators.....	11
The parabola with flipper design: sample g389.....	14
The coexistence of plasmons in intersubband potential wells.....	15
Further investigations on magnetic field effects.....	18
Resonant tunneling in the domain of high carrier densities.....	26
A vertical cascaded structure other than square wells.....	29

## measurement setups.

Fourier transform infrared spectroscopy.....	33
InSb cyclotron resonance spectroscopy.....	35

## Experimental Part 2: Plasma instability

Quasidoping: the sample G428.....	38
Highly doped injector and collector regions: the sample G494.....	40
Cascading of PI modules: the sample G534.....	42
Reducing the current density and the plasmon frequency: G595.....	45
Low doping to allow for more cascades: G565.....	50
New designs and material systems. G564.....	53
Increasing the emission due to more cascades. the sample W2.....	61
Increasing the current densities again: G672.....	67

## References

# Introduction

## Foreword

Electromagnetic waves at terahertz frequencies or submillimeter wavelengths hold the potential of a wide variety of applications that include sensing, spectroscopy, imaging, heterodyne detection, and wireless data transmission in areas such as industrial process control, medical diagnostics, micro surgery, radio astronomy and communications [1]. Most of this applications still lack the existence of a compact, electrically driven, powerful, coherent solid state source emitting at frequencies between 1 and 10 THz, i.e. in the Far-infrared (FIR) at wavelengths between 300 and 30  $\mu\text{m}$ . While this project was ongoing first semiconductor lasers emitting in the 80  $\mu\text{m}$  range were realized based on the quantum cascade principle, thus overcoming some of the predicted main problems of this design in the FIR [2].

## Aim of the project

A state of the art QCL Laser operating in the 120  $\text{cm}^{-1}$  range must be cooled down to LHe temperatures and is driven by electrical pulses of some hundred nanoseconds duration at a kilohertz repetition rate [3, 4]. This is still a very low efficiency and output intensity due to the high intrinsic losses by free carrier absorption in the FIR and the dominance of electron-electron scattering as a relaxation channel. Its radiation intensity typically is absorbed to a point below detection limit in normal humid air over a distance of less than five inch.

In this project the realization of compact efficient and robust THz sources based on the radiative decay of confined plasmons in low dimensional semiconductor structures was investigated. The plasmon emission process is a promising concept for the use of collective carrier oscillations as active medium for stimulated emission. This concept was first proposed by Bakshi and Kempa [5, 6].

The basic idea is to generate plasma instabilities (PI) [7, 8] with the help of appropriate carrier injection and extraction schemes in quantum well structures. As the plasma instability can be described as the stimulated generation of plasmons, the micro-charge oscillations of such plasmons can become the source of electromagnetic radiation in the THz range. This plasma instability based concept differs from the conventional lasers since it is based on a collective phenomenon, in contrast to the single particle nature of the lasers. It is thus less susceptible to disruption due to higher temperatures and various scattering effects.

A partial inversion of the carrier distribution is required [9, 10] which is achieved by the use of heavy carrier injection into a confined active region where the plasmons are generated, followed by an energetically selective extraction scheme which maintains the inversion. Basic elements of the structures designed for the PI experiments are two coupled quantum wells, one of which acts as a plasma resonator that can sustain growing plasma oscillations and the other which acts as a plasmon emitter, providing a proper arrangement

of levels to assure efficient emission of plasmons into the resonator. A resonant tunneling diode filter, attached to the plasmon emitter maintains an efficient carrier extraction from the active region.

The band structure under bias for a typical unit cell for plasma instability is shown in Fig. 0.1: The basic idea kept for merely all the PI sample designs described in this report is to realize a three level scheme of finite and controllable size in which the first subband and the third subband of the plasmon emitter quantum well are occupied, while the second subband is kept partially empty [6]. Occupation of the third level is assured by heavy electron inflow from the plasmon reservoir area, while the occupation of the first level is due to the very fast intersubband transitions from the third subband via optical phonon emission. The energy separation between the third and first subband is chosen to be equal or larger to the energy of an LO-phonon. Since the LO-phonon scattering time is of the order of 200 fs this process is very effective. The second subband is designed in a way that the level can be aligned under typical bias conditions to the resonant level of the extractor resonant tunneling diode. This extraction, if efficient, assures a lower population due to resonant carrier extraction. The essential instability mechanism is then the resonance of two intersubband plasmon excitations, for example, when the depolarization down shifted plasmon emission frequency from subband 3 to 2 is in resonance with the depolarization upshifted plasmon absorption frequency from subband 1 to 2 [6].

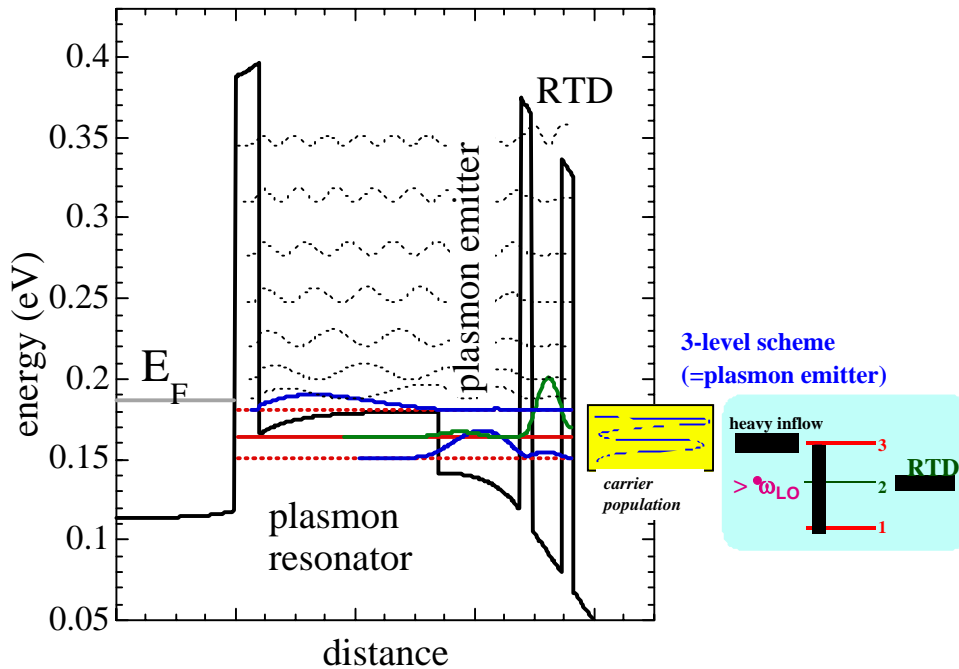
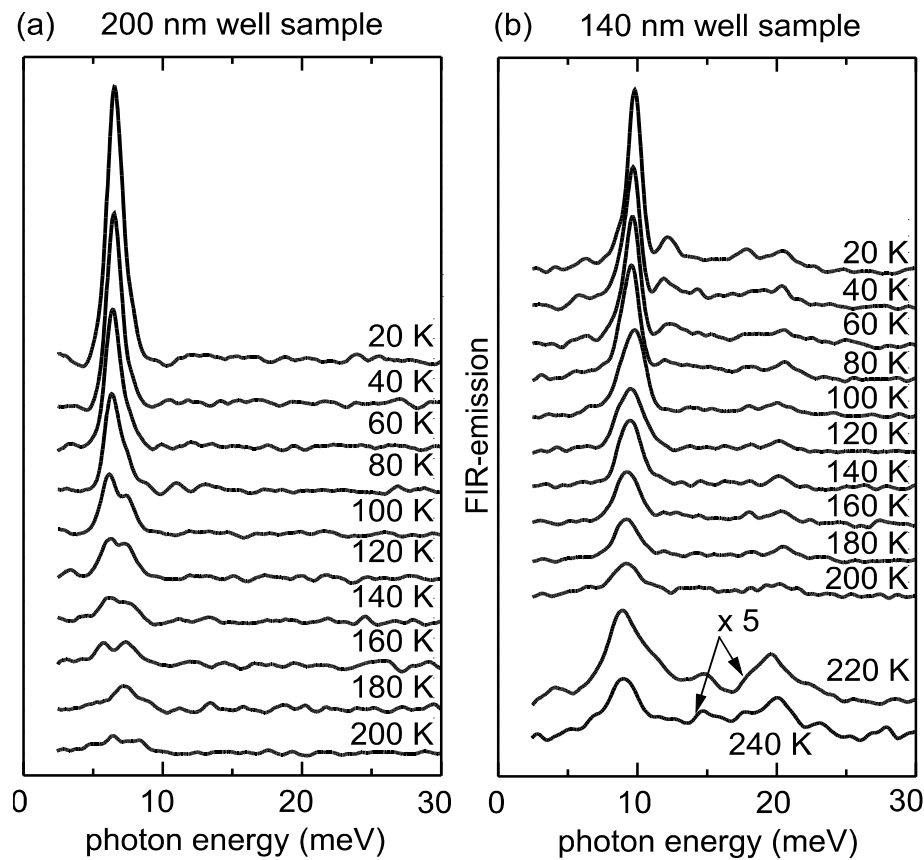


FIG. 0.1: Typical conduction band diagram of a plasmon generation device consisting of a plasmon resonator, a plasmon emitter (3-level scheme), and a resonant tunneling extraction diode. The insets show the expected population inversion with the 3 levels and the level structure with the carrier transitions (from report ARO N68171-96-C-9015).



## previous accomplishments

The radiative decay of plasmons from two-dimensional electron channels [11] and parabolic quantum wells [12] was observed emitting radiation in the THz region. Parabolically graded quantum wells are promising candidates for far-infrared sources operating above liquid nitrogen temperature. They are based on the radiative decay of plasmon oscillations with their emission frequency independent of electron-electron scattering and the electron concentration in the well. Therefore, the large temperature-induced variation of the electron distribution is expected to have little impact on the emission performance, which has been confirmed in absorption and emission spectroscopy up to more than 200 K [13], see Fig. 0.2 and the previous report ARO N68171-96-C-9015.



*FIG. 0.2: Temperature dependence of the far-infrared emission of parabolically graded plasmon resonators for 2 different well widths (140 nm and 200 nm). Emission is observed well above liquid Nitrogen temperature (from report ARO N68171-96-C-9015 & [13])*

Kersting et al. [14] have observed the emission from coherent plasmon oscillations even at room temperature from bulk carriers on a picosecond time scale. These results suggested that plasma oscillations could survive even at room temperature in doped semiconductors.

A first set of PI sample structures (G205, G301) based on the 3-level step quantum well design described above was grown and found to exhibit weak emission in the FIR, Fig. 0.3. It is clearly observed that intersubband emission (stemming from radiative 3-2 transitions in the scheme of Fig. 0.1) sets in above a certain current injection level [15].

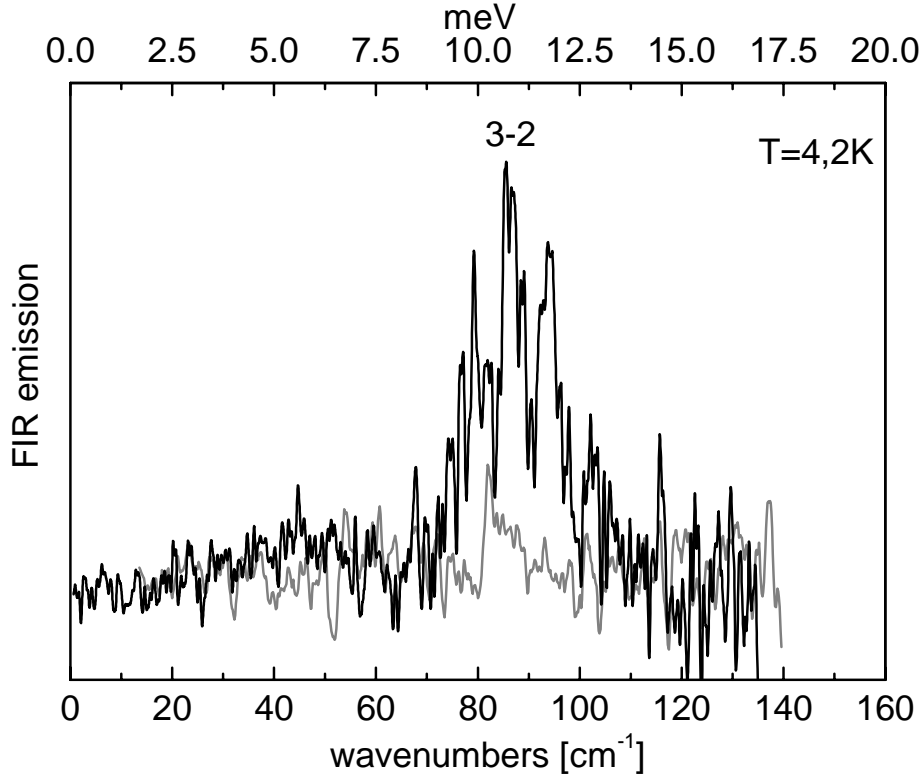


*FIG. 0.3: Intersubband emission around 11 meV photon energy is clearly detectable in the sample G301. Lower curve: below the critical voltage (0.4 V bias shown as grey curve) for extraction resonance of the RTD levels with the step well energy levels only broad free carrier emission is seen from the 2DEG. Upper curve: above the onset of resonant current situation (0.7 V bias shown, black curve) the much narrower emission from an intersubband transition is observed. The Plasma instability regime, however, was not yet reached with this structure (from report ARO N68171-96-C-9015)*

The design of this samples and the processing technology were the starting point for the PI sample structures covered in this report. The main items of G301 are bulk doping in the reservoir region and the lack of cascading.

Results on the emission experiments proving intersubband emission in the pW optical power range at about 12 meV photon energy with no further traces of a PI phenomenon are discussed in detail in the previous projects ARO N68171-96-C-9015 final progress report.

## **the building steps for plasma instability**

As one conclusion from the non-decisive results of G301 it was advisable to isolate different aspects of the very complex plasma instability concept for separate experimental research and verification. Simultaneously to the ongoing design of new PI samples structures were designed and measured to deal specifically with the following topics:

- the existence of the intersubband resonance plasmon in semiconductor quantum structures and the depolarization shift,
- parabolically graded plasmon resonators
- the simultaneous existence of several different types of plasmon modes in semiconductor quantum structures and their mutual interactions
- influence of an externally applied magnetic field
- resonant tunneling in the domain of high carrier densities
- the combination of a plasmon resonator with vertical current injection and cascading.

This experimental investigations are not presented in a chronological order but instead are summarized in the following experimental part 1.

The experimental part 2 then is an almost chronological report of all measurements on PI samples.

# Experimental Part 1: general aspects

## The Intersubband resonance plasmon and the depolarization shift

In the case of the intersubband resonance (ISR) plasmon the Coulomb interactions of two electron subbands are described as a virtual exchange of plasmons, i.e., when averaged over time some parts of the electron subband energies are stored in a quasiparticle. (in principle for the bulk plasmon the amount of energy stored in the ‘quasiparticle’ can be easily calculated, it is just the amount of the Fourier transformed electron-electron pair interactions summed up to the Debye wave vector. [16])

As with Cooper pairs the concept of virtual quasiparticle exchange [17] arises from the use of single electron base functions for the description of a many particle *eigenstate* of the crystal Hamiltonian. The ISR plasmon can therefore likewise be considered as a coherent superposition of two subband wavefunctions weighted with their respective subband electron sheet densities that undergo Rabi type oscillations under the action of their mutual Coulomb interaction.

*Physically* the depolarization effect arises because in the case of high carrier densities each electron in a quantum well feels a field which is different from the external field by the mean Hartree field of other electrons polarized by the external field.

*Conceptually* this may be modelled as a single electron transition feeding its excess energy into a plasmon mode whose radiative decay is then observable. The calculation of the depolarization shift for a two level system is also straightforward [18, 19] if a steady population of both levels is maintained by some pumping mechanism, e.g. by a steady state current injection into the upper level or optical pumping with laser light and a steady state relaxation rate to the lower level, keeping the densities at the upper and lower level at  $\rho_{11}$  and  $\rho_{00}$ , respectively:

$$\omega_p^2 \propto \frac{2(\rho_{00} - \rho_{11})e^2}{\epsilon\eta} \omega_{10} S_{11}$$

where  $\omega_p$  denotes the frequency detuning of the intersubband transition which is proportional to the bare intersubband frequency separation  $\omega_{10}$ , the *difference* of the carrier densities of the levels involved and the so called Coulomb length tensor defined by

$$S_{11} = \int_{-\infty}^{+\infty} dz \left( \int_{-\infty}^z dz' \chi_1(z') \chi_2(z') \right)^2$$

The depolarization shift therefore in general can have both signs and the observed optical frequencies  $\tilde{\omega}_{ij} = (\omega_{ij}^2 + \omega_p^2)^{1/2}$  are either blueshifted or redshifted, depending on whether the level population is close to thermalized, or inverted by some pumping process [20].

This shifts are a main issue for PI based solid state emitters and their experimental verification highly desirable [21].

It is noteworthy, however that the population of the various involved energy levels are an input parameter of the calculation schemes. Assumptions about these occupation numbers are obviously most easily made in a completely thermalized situation as in the laterally streamed parabolic wells. Highly sophisticated models are needed to calculate these level occupation numbers in vertical injection schemes. Such models were developed by the collaborating Boston group [22].

## Parabolically graded plasmon resonators.

While the phenomenon of the depolarization shift was already well documented in FIR absorption experiments [23] and quantitatively explained by calculations by Allen [18] and Ando [24] its experimental observation for the case of emission is a cornerstone for the realization of PI concept.

To learn as much as possible about plasmon resonators many different parabolically shaped potential wells were grown and investigated for their FIR emission behavior. Wells were designed for plasmon resonances in the range of 50 to 140 wavenumbers [26]. Fig. 1.1 shows the FIR emission resonances of three different wells for the same electrical input power. The curvature of the wells was designed for 6.2 meV (for the flattest well), 9.3 meV and 12.5 meV (for the most steeply curved well) harmonic oscillator energy.

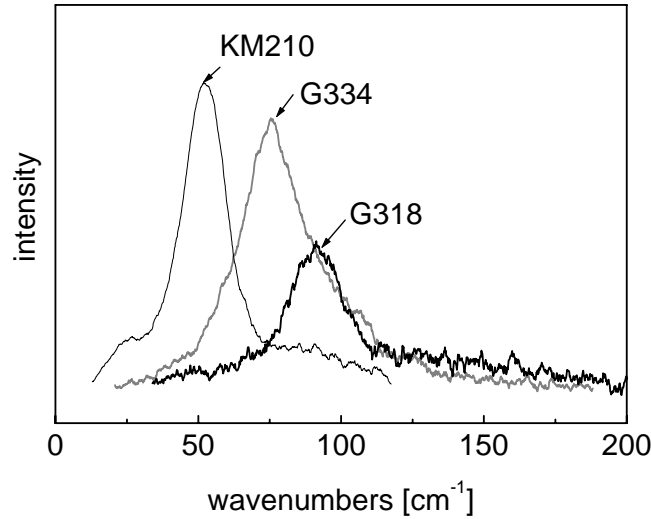


*FIG. 1.1: FIR emission for three different parabolic quantum wells. The grown potential curvature (nota bene not the well width) was designed for a harmonic oscillator resonance of 6.2 meV (for the flattest parabola, KM210), 9.3 meV(G334) and 12.5 meV (for the most strongly curved parabola, G318). The electrical input power was the same for all three wells. The emission intensities in this case reflect the thermalized electron energy distribution [26].*

In these experiments the current is pumped laterally through the wells, i.e. along the active layer. In this case the energy transfer into the plasmon mode is from electrons in the wells, which are accelerated by the applied electrical field. Their distribution can be considered thermalized with an assigned electron temperature high above the lattice temperature. The radiation intensities seen in Fig. 1.1 may therefore also be considered a scanning through the electron energy distribution.

The outstanding importance of parabolic resonators simply lies in the fact that these are the only quantum systems so far, where the *collective* nature of observed FIR emission is beyond doubt. The importance of parabolically graded potentials is further increased by the Kohn theorem [25] which allows for the completely analytic calculation of the observable collective resonances which can then be compared to the result of a full blown self consistent numerical calculation scheme.

Imperfections of the wells like vertical sidewalls or a flat region in the center of the well were found to account only for small deviations from the ideal harmonic oscillator behavior of perfect wells [27]. Fig. 1.2 shows typical results. The experiment is explained in the figure capture.

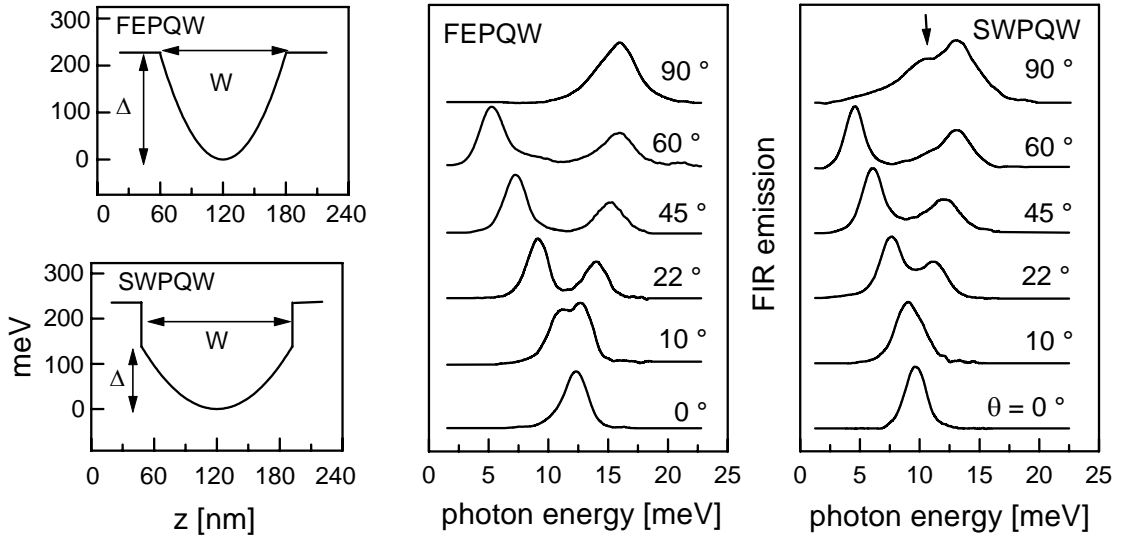
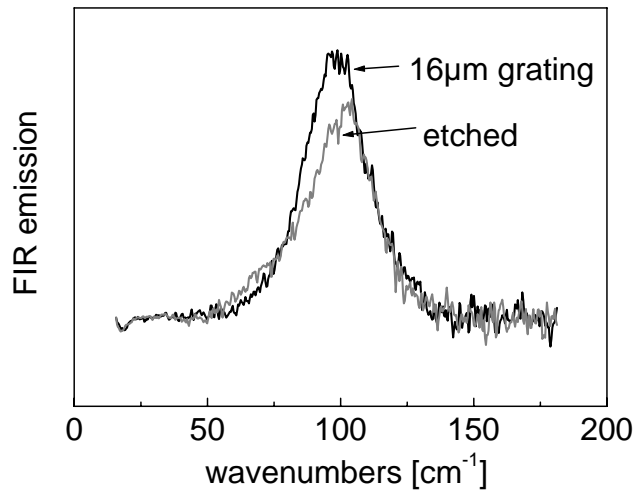


FIG. 1.2: Comparison of an ideal parabolic resonator with a partially parabolic resonator with vertical sidewalls. In this experiment an constant external magnetic field is applied that is tilted at different angles with respect to the growth axis of the samples. A mode anticrossing occurs in this case and two main peaks occur. Any imperfections of the wells create satellite peaks under these conditions whose intensities are increased by the anticrossing, quite analogously to amplification by heterodyning. Small imperfections are found in this way in the figure (see the arrow), but the dominant frequencies remain quite robust those of the Kohn mode [27].

A stacking of parabolic potential wells increases the observed linewidth as shown for a fivefold stack of parabolic wells in Fig. 1.3. From this a slight variation of the growth parameters from well to well may be concluded. As in the previous experiments this structure is not designed for vertical current injection but again is streamed laterally. The observed increase in linewidth can be attributed to an inhomogeneous broadening by slight deviation of the well properties from well to well.

An additional result of these measurements was the experimental confirmation that two types of radiation outcoupling may perform equally well for all the discussed sample structures emitting in the FIR region. Fig. 1.3 compares the emission obtained from the fivefold stack sample by a 16 micron period metallic grating coupler evaporated on top of the sample surface to the emission obtained by using the same grating as an etching mask and etching completely down *through* the fivefold active region. In this case radiation outcoupling is only from the edges of the etched out sample fingers. Since the wavelength of the radiation, however, is much bigger than the period and size of the etched fingers, the first order of diffraction still gives a maximum of the emitted radiation perpendicular to the sample surface. The surface depletion length - a main concern when considering edge coupling - is therefore found to be much shorter than the typical length scale for self absorption of the spontaneous FIR emission [28]. The etch-through design was adopted in the following for merely all PI sample structures.



*FIG. 1.3: A fivefold stack of identical parabolically graded wells shows a considerable increase of FWHM linewidth while the center frequency is still in agreement with the calculated and designed position. Slight deviations of the well parameters and interactions of the electron slab from well to well inhomogeneously broaden the emission line. Two different outcoupling methods are compared: For the same electrical input power and the same emissive area a sample with a 16  $\mu\text{m}$  period metallic grating coupler on top gives approximately the same detected output power as an edge coupler design obtained by using the same grating as an etching mask and completely etching top down through the active region [26]. Outcoupling by etched out fingers was adopted in the following also for the PI structures.*

Results however were reasonably well for the first growth of an extended cascaded structure, incorporating more than 30 parabolic wells and intended for vertical resonant current injection as discussed later (sample G479).

Results so far encouraged the implementation of parabolic resonators in more sophisticated active cell designs like the sample G389 described below as well as a further investigations of the effects of magnetic fields on plasmon emitters.

### The parabola with flipper design: sample G389

Increasing experience at our institute in growing and designing parabolically shaped plasmon resonators suggested trials with the following mechanism: To a plasmon reservoir shaped as a semiparabola a region is added where a dynamic charge inhomogeneity can develop to the plasmon bath excited by a dc current fed through the cell.

The basic bandstructure of such a scheme is shown in Fig. 1.4. The structure consists of a narrow barrier, separating the doped region to the left reservoir from the parabolically profiled active region. The curvature of this parabolic confining potential has been chosen so that the Kohn resonance (i.e. the plasmon in the parabolic region) is at 12 meV.

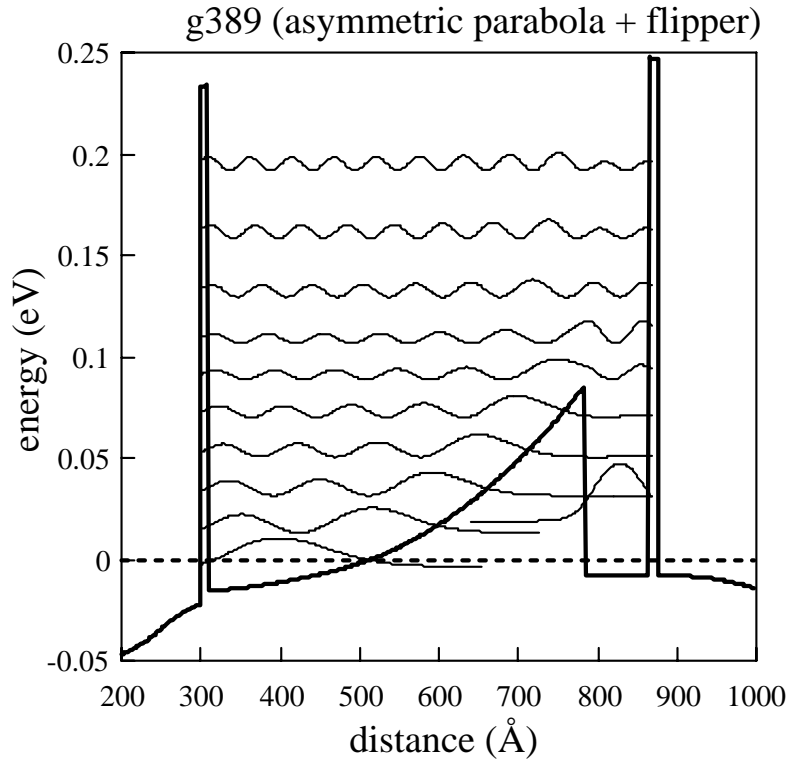


*FIG. 1.4: The energy of the conduction band edge versus distance of the modified step quantum well, i.e. the parabola & flipper pocket design. The solid lines represent the squared wave functions of the quantized states.*



Immediately to the right of the parabola is a linearly graded region of the pocket. Finally a narrow barrier separates the pocket from the outside doped region. This barrier and the pocket simulate the dynamic inhomogeneity region.

To calculate the possibility of an instability in this design the RPA formalism is again applied [29]. A robust instability at a resonant energy of 13.7 meV is found. Due to nonlinear effects this instability supports large charge oscillations. To understand this one has to assume that initially the pocket is empty. Then the corresponding energy position of the pocket is at its lowest value. As the pocket fills with electrons from the left through a starting current injection the energy position of the pocket increases. In the process, the potential wedge, which rises even faster, strongly reduces the charge in-flow into the pocket. As the inflow of charge in the pocket diminishes, the current outflow through the right barrier begins to empty the pocket. Consequently the screening decreases, causing the potential energy position of the pocket to approach its minimum value again. This, in turn, lowers the wedge, and with the in-flow of charge into the pocket, a new cycle begins. This periodic charge buildup in the pocket occurs at the expense of the charge in the parabolic region, and will enhance charge sloshing there, leading to an enhancement of the instability in the asymmetric parabolic well.

Measurements of the IV characteristics and their comparison to the results of a calculation based on the RPA method were already reported in the previous project report. The predicted instability occurs at a bias above 0.15 V. The experimental data showed very good agreement to the calculated results, verifying the basic functionality of the structure.

In order to investigate especially the influence of the flipper region a simplified version, i.e. an asymmetric parabola without flipper, the sample G390 was also grown to compare its behavior to G389. The results of transport measurements on this sample also were previously reported.

A thorough experimental search for emission from these two designs which had already started in the previous project and was intensified in the running project brought no conclusive result. No traces of FIR emission both of the simple design G390 and the sophisticated design G389 were found.

## **The coexistence of plasmons in intersubband potential wells**

Many-body effects in low-dimensional semiconductor structures containing always remain a three-dimensional problem [30]. The elementary excitations in a 2DEG therefore include both collective motions of the carriers perpendicular to the well (the ISR plasmon) as well as along the active layer (i.e. the 2D-plasmon [31]). While these inplane oscillations usually are not observed in intersubband emission experiments and in most cases are neglected in the underlying theoretical calculations they nevertheless always exist and represent a competitive relaxation channel of considerable oscillator strength.

A first example for the existence of several independent plasmon modes is the simultaneous observation of the intersubband plasmon and the intrasubband plasmon, i.e.

the so called 2D-plasmon [31, 32], as given by their emission spectra in Fig. 1.5. The parabolic structure for this experiments differs neither by the growth procedure nor by the sample processing from the parabolas described earlier, except for a designed Kohn resonance at almost 20 meV and a smaller period (900 nm) grating coupler. This narrow-period coupler while less effective for coupling out the ISR emission line is mandatory for transforming the traveling inplane waves into standing waves that can couple to light. This then gives the observed 2D-plasmon emission line at 9.4 meV.

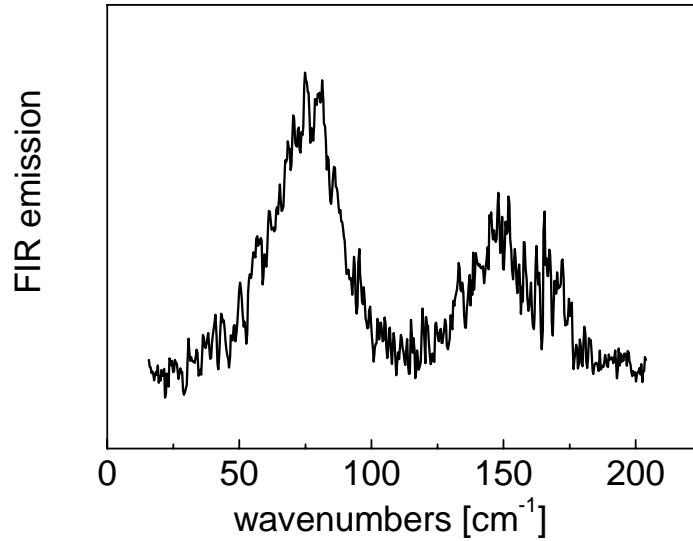


*FIG. 1.5: The coexistence of the ISR plasmon (emission at  $150\text{ cm}^{-1}$ ) and the 2D-plasmon (emission at  $75\text{ cm}^{-1}$ ) in a parabolic quantum well. Growth procedure and sample processing of this parabola basically do not differ from the previous experiments, except for a narrower spaced metallic grating coupler (800 nm period) to make the 2D plasmon radiative through Bragg reflection of the inplane traveling waves. While electric input power (100 mW) is comparable to the previous experiments, grating coupler efficiency is strongly reduced for the ISR plasmon [26].*

PI effects based on the presence of 2D-plasmons are also discussed in the literature (e.g. for very short gate field effect transistors by Michail Shur [33, 34]) but were not pursued further in the running project.

It is tempting to force the coexistence of plasmons by external means such as a magnetic field. Exactly in the same way as the intersubband resonance is influenced at high carrier densities by constructive electron-electron interactions the cyclotron resonance becomes a collective phenomenon providing an easy means to *tune* the frequency of an ideal plasmon mode via an external controllable parameter, i.e. via the magnetic field. Most interesting certainly is the point where the intersubband plasmon resonance and the cyclotron

resonance nominally coincide. In parabolic quantum wells the interaction of the modes depends on the tilt angle of the applied magnetic field [35]. In agreement with the Kohn theorem, however, the two modes always exhibit an anticrossing behavior [36] and never can be brought into resonance, as already seen in the previous Fig. 1.2.

This makes *ideal* parabolic wells under thermal quasi-equilibrium conditions not suited for the excitation PI phenomena but does not exclude their implementation in more sophisticated designs such as e.g. the parabola with flipper G389, see above.

As a spin off from the tilted magnetic field experiments on parabolic quantum wells [26, 27] they yield a method for the calibration of a blackbody source whose output power can be determined by a fitting procedure instead of the measurement with a calibrated detector [37, 38], which usually lacks exact knowledge of the collection efficiency of the experimental setup. The procedure is explained in detail in Ref. 27 and sketched in Fig. 1.6.

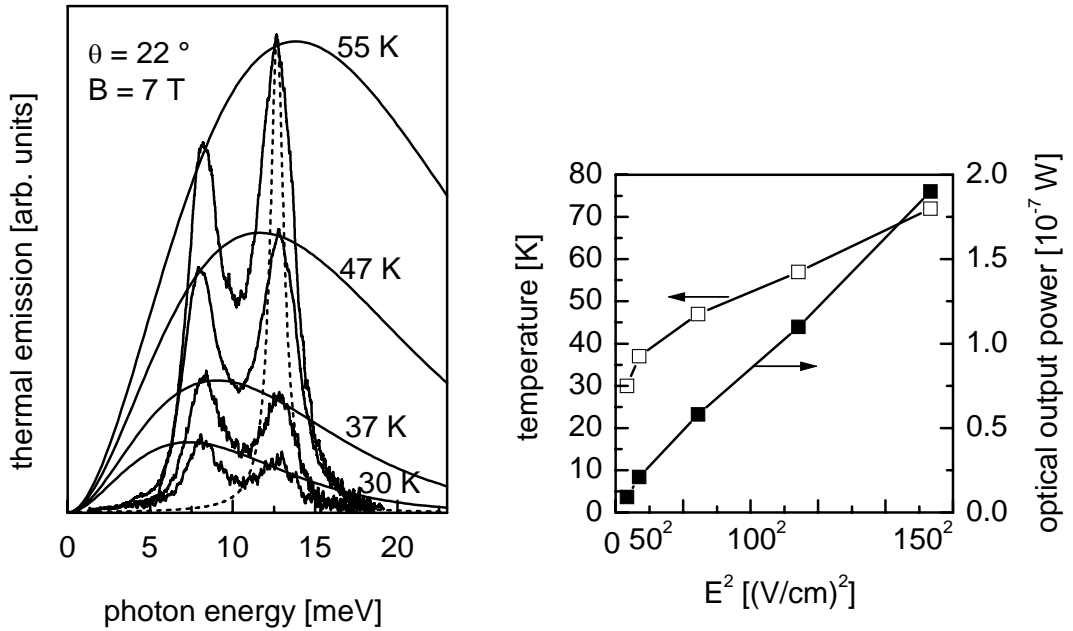


FIG. 1.6: Optical output power calibration by fitting blackbody radiation curves to the measured spectra in a tilted magnetic field at four different electrical input powers. Due to the two strong plasmon peaks an uncalibrated detector can be used for the procedure. The dashed line represents a Lorentzian model of the emission lines with their actual FWHM linewidth of 1.1 meV). The four electron temperatures  $T_e$  are assigned corresponding to blackbody fitting curves as following from Planck's radiation law. (right): Electron temperatures and optical output power vs.  $E^2$ . No saturation in emission intensity is found.

## Further investigations on magnetic field effects

Electron-electron scattering [39] is the prime mechanism which restores thermodynamic equilibrium in an electron gas. It can play an important role in intersubband transport in quantum wells with sufficiently high carrier densities [40, 41]. It was also suggested as the dominant mechanism of intersubband carrier relaxation in quantum cascade structures designed to emit in the THz frequency range [42]. In such structures, electron-LO phonon scattering is suppressed, since the energy separation of the subbands is less than the optical phonon energy (36 meV). In both the QCL like structures as well as our PI structures maintaining a nonequilibrium steady state of the electron distribution is of crucial importance. A modification of the density of states by the application of a magnetic field parallel to the growth direction of PI structures might help suppress Auger scattering processes which are considered a prime candidate for nonradiative intersubband relaxation.

We have investigated the effects of magnetic fields both in transport and emission experiments on QCL like structures which were grown in our institute, exhibiting strong Terahertz emission [43]. Since quite intensive research was carried out on this peculiar structure it is described in more detail in the following.

The terahertz emission in the experiment presented here stems from the 2 to 1 transition in a 26 nm wide quantum well [44]. Electrons are injected into subband 2 and extracted from subband 1 by resonant tunneling. The band structure given in Fig. 1.7 is basically a downscaled version of a mid-infrared quantum cascade structure.

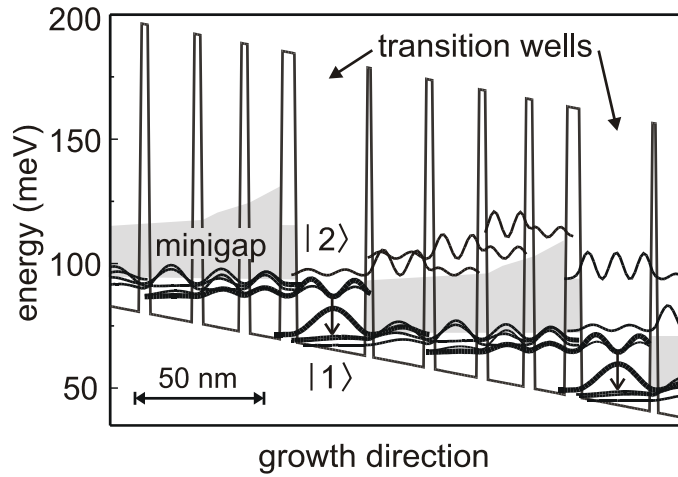


*FIG. 1.7: Two periods of the band structure of the quantum cascade structure designed for emission of terahertz radiation. The well and barrier widths starting with the transition well given in nanometers are: 26, **2.5**, 19.5, **3**, 16, **3**, 14, **3**, 12.5, **6**. Barrier widths are printed bold face and those widths corresponding to doped wells ( $n = 1 \times 10^{16} \text{ cm}^{-3}$ ) are underlined. The moduli squared of the envelope wavefunctions are plotted at their corresponding eigen energies [44].*

The whole structure is made up of 50 periods of a chirped  $\text{Al}_{0.15}\text{Ga}_{0.85}\text{As}/\text{GaAs}$  superlattice. The radiative 2-1 transition in the widest (26 nm) quantum well has a matrix element of 5.7 nm. At an appropriate electric field (22 mV/period), electrons are resonantly injected from the first miniband of the injector (4 wells) into the second subband ( $E_2$ ) of the transition well. The electrons escape from the ground subband ( $E_1$ ) via resonant tunneling whereas tunneling from  $E_2$  downstream is inhibited by the minigap of the adjacent injector. The second miniband at the operation bias is Wannier-Stark localized and does not contribute to carrier transport. The two center wells of the injector are lightly doped to ensure a constant electric field across the structure.

Results on electroluminescence experiments when various magnetic field strengths are applied to the structure are shown in Fig. 1.8.

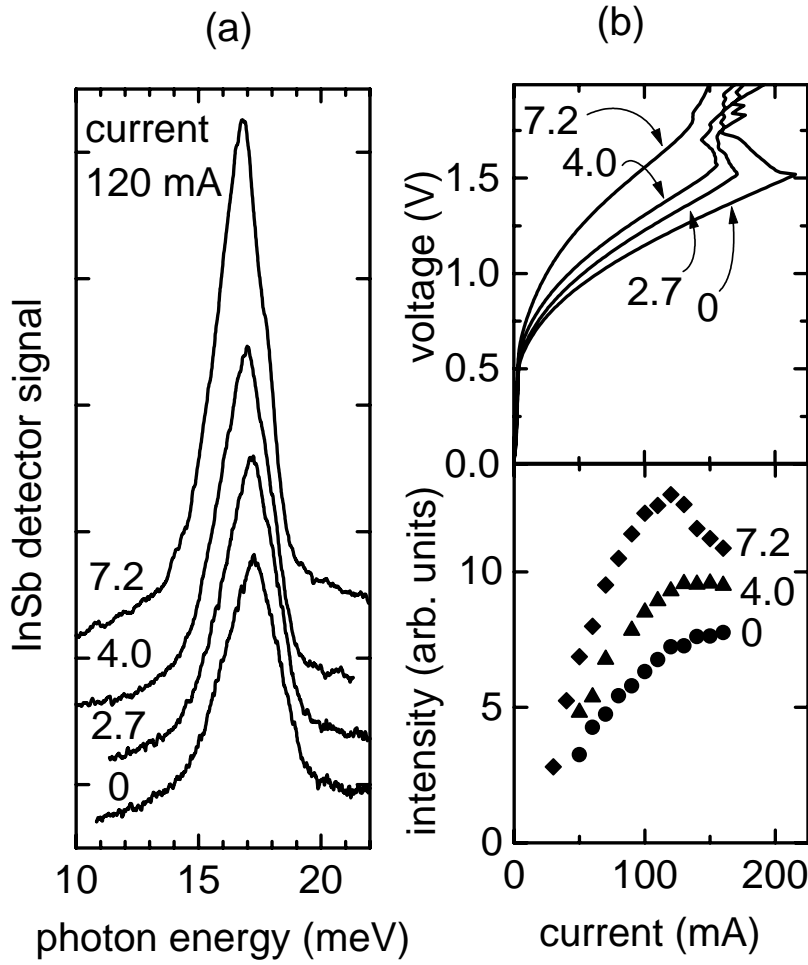


FIG. 1.8 (a): Intersubband electroluminescence spectra at a constant current for various magnetic fields given in Tesla. The spectra are plotted with arbitrary offsets. (b) Voltage versus current characteristics (top) and light intensity versus current characteristics (bottom). The intensity has been extracted from the spectra as the integrated area below the emission peak.

We employed the InSb-cyclotron resonance spectrometer to record electroluminescence spectra. The magnetic field of the emitter magnet is perpendicular to the epitaxial layers and can be adjusted independently of the detector magnetic field from 0 T to 7.5 T. Voltage pulses of 22  $\mu$ s length at a repetition rate of 23 kHz are applied between the top and bottom contacts using the HP-pulser. The spectra are obtained scanning the detector magnetic field while leaving the emitter magnetic field constant.

It was theoretically predicted earlier [45], that the application of a magnetic field normal to the epitaxial layers would suppress intersubband Auger-scattering since the continuous energy spectrum breaks up into discrete Landau-levels. The magnetic field dependence of the luminescence intensity shows strong oscillations. These magneto-intersubband oscillations are caused by the modulation of the transition rate via resonant inter-Landau-level transfer.

The spectrum at 0 T as displayed in Fig. 1.8 (a) shows a single peak centered at a photon energy of 17.3 meV, exactly like the sample discussed in the previous section. The peak is identified as the emission from the 2-1 transition. Once more, the measured full linewidth at half maximum of 2.4 meV is not the true emission linewidth, but it results from the convolution with the detector function.

Application of a magnetic field enhances the emission intensity by a factor of two at  $B = 7.2$  T (Fig. 1.8 (a)). This effect is understood as a consequence of the discretization of the energy spectrum.

In the parabolic dispersion relation in the absence of a magnetic field elastic scattering processes from subband 2 to 1 are possible, while in the discretized dispersion, at an arbitrary magnetic field the Landau ladders originating from subband 1 and 2 are not resonant (Fig. 1.9 (a)). The same rationale applies for electron-electron scattering processes, where the energy  $\Delta E$  that one electron loses is transferred to the second electron (Fig. 1.9 (b)).

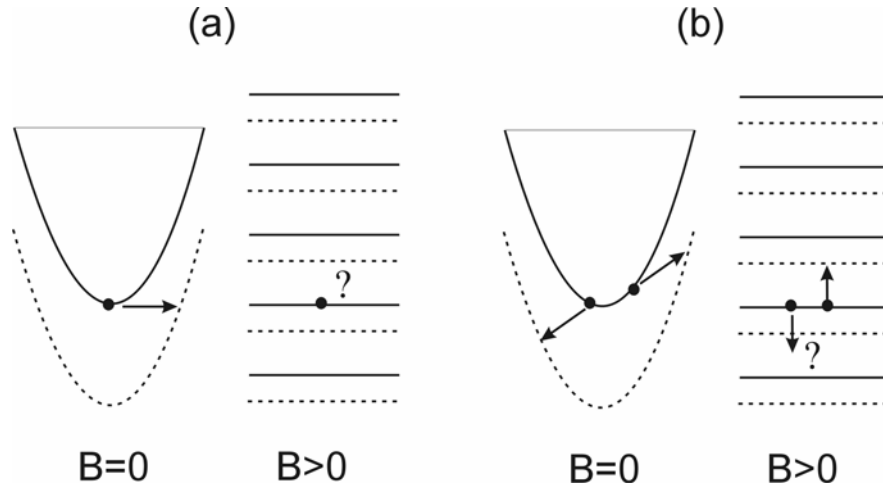


FIG. 1.9: Quenching of disorder related elastic scattering processes (a) and electron-electron scattering (b) in a magnetic field.

Without a magnetic field, the energy conservation requirement for electron-electron intersubband processes is fulfilled for a continuum of energy changes  $\Delta E$ . However, for a non-vanishing magnetic field the only allowed energy changes  $\Delta E$  are multiples of the cyclotron resonance energy  $\eta\omega_c$ . Since the electron-electron scattering rate scales inversely with the associated change in energy and momentum [39], it is more and more suppressed with increasing Landau-level splitting. The emission intensity is proportional to the current  $I$  and to the internal quantum efficiency, that is the spontaneous emission rate  $\Gamma^{spon}$  over the total rate  $\Gamma^{spon} + \Gamma^{nr}$

$$P_{opt} = \eta N \frac{\Gamma^{spon}}{\Gamma^{spon} + \Gamma^{nr}} \frac{\eta\omega}{e} I$$

where  $\eta$  is a collection efficiency ( $\sim 10^{-4}$ ) and  $N$  is the number of periods. The total rate is profoundly governed by the non-radiative rate. Hence, the observed enhancement of emission intensity is a direct measure of the suppression of the intersubband scattering rate from subband 2 to 1.

In our interpretation of the effect, we assume that the miniband transport in the injector, as well as the resonant tunneling injection into subband 2, and the escape from subband 1, remain unchanged in the presence of a magnetic field. This assumption is reasonable because the effective mass and therefore the energy shift  $\frac{1}{2}\eta\omega_c$  is equal in all GaAs wells of the injector and in the transition well. The slight red shift of the emission peak in the magnetic field Fig. 1.8 (a) is an artefact of the measurement set-up. The detector is detuned by a small stray field from the magnet at the sample.

Examining the intensity versus current characteristics given in Fig. 1.8 (b) we find an enhancement in a magnetic field by about the same factor for currents below 120 mA. At the highest magnetic field of 7.2 T the intensity drops when the current is increased above 120 mA. This is a consequence of the misalignment of the structure. If the 2-1 intersubband scattering rate is quenched by means of a magnetic field, a higher voltage must be applied to maintain the same current. This can be seen in the voltage versus current characteristics in Fig. 1.8 (b) and in the voltage versus magnetic field characteristics in Fig. 1.10 (b). Eventually, the bias reaches the region of negative differential conductance where the injection into subband 2 and therefore also the emission break down.

The emission peak is significantly narrowed in the presence of a magnetic field. The field free width of 2.4 meV in our spectra decreases by 17% down to 2.0 meV at a magnetic field of 7.2 T. When we subtract the detector linewidth of  $\sim 1.3$  meV, the true narrowing is about 36%. The true emission linewidth at 7.2 T is smaller than the detector linewidth. Therefore, the double peaked structure of the detector function [46] is resolved as a shoulder at the high energy side of the peak. The line narrowing in a magnetic field cannot solely be explained by the change in intersubband lifetime. If we assumed that the intersubband lifetime doubles in a magnetic field of 7.2 T, whereas the in-plane dephasing time remains unchanged, we would derive an intersubband lifetime of 0.8 ps from the reduction of linewidth. This value is more than one order of magnitude below the estimates from the emission efficiency [47]. Thus we conclude that the in-plane dephasing time,

which presumably determines the linewidth, is also reduced by the Landau-quantization. In the presence of a magnetic field in-plane dephasing always involves scattering between Landau-levels. Hence, the dephasing time is identical to the Landau level lifetime. The latter is known to increase proportional to the magnetic field [48].

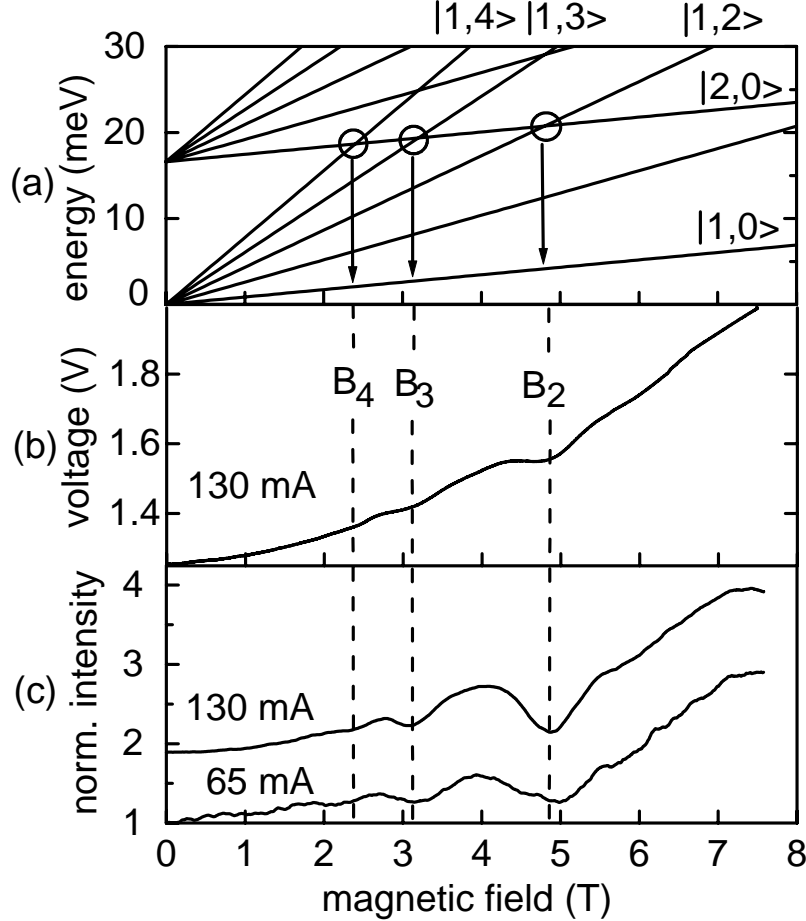


FIG. 1.10 (a): Energy levels in a magnetic field (Landau-fans) plotted for a subband separation of  $E_2 - E_1 = 16.6$  meV. The scale was chosen so that  $E_1 = 0$ . At the magnetic fields  $B_2$ ,  $B_3$ ,  $B_4$ , magneto-intersubband resonances (marked with circles) enhance the scattering rate from subband  $|2,0\rangle$  to  $|1,0\rangle$ . (b) voltage and (c) light intensity plotted against magnetic field at constant currents as indicated. These characteristics have been recorded scanning the sample magnetic field while leaving the detector constantly tuned to the photon energy of the emission line. The intensities are normalized with respect to the value at zero magnetic field and at 65 mA.

As depicted in Fig. 1.10 (c), the emission intensity is not a monotonic function of the magnetic field, but it exhibits strong oscillations. At fields of 2.2 T, 3.2 T, and 4.9 T we find dips in the emission intensity. Similar oscillations, though smaller in amplitude, are present in the sample resistance. The voltage across the sample (Fig. 1.10 (b)) shows dips



at the same fields. We interpret our data in terms of a modulated intersubband scattering rate. There have been analogous explanations for oscillations in the (interband-) electroluminescence intensity in a resonant tunneling structure [49] and in superlattices [50]. In those cases the scattering rate was modulated by a magneto-phonon resonance [49, 50] or by a magneto-exciton resonance (), whereas, we consider the magneto-intersubband resonance. Whenever an integer number of Landau-levels fits into the intersubband energy difference  $E_2 - E_1$ , the lowest Landau-level of the second subband, denoted as  $|2,0\rangle$ , aligns with the  $N$ th Landau-level of the first subband  $|1,N\rangle$ . The circles in Fig. 1.10 (a) mark such situations. Resonant tunneling between Landau-levels opens up an additional non-radiative relaxation channel via the Landau-ladder ( $|1,N\rangle, |1,N-1\rangle, \dots |1,0\rangle$ ). The faster total  $|2,0\rangle$ - $|1,0\rangle$  intersubband relaxation leads to an increase in the sample conductivity and thus to a higher current. In our experiment, however, the current is kept constant, and a drop in the applied voltage is observed instead. The electroluminescence intensity drops since the injected carriers are distributed among the levels  $|2,0\rangle$  and  $|1,N\rangle$ , and those in  $|1,N\rangle$  do not contribute to the intersubband emission.

According to the equation

$$E_2 - E_1 = \frac{\eta e B_N}{m_0^*} N$$

we determine the energy difference  $E_2 - E_1$  by identifying the positions of the three observed intensity minima with the characteristic fields  $B_N$ , ( $N = 2, 3, 4$ ) for which level  $|1,N\rangle$  aligns with the level  $|2,0\rangle$ . Using the effective mass  $m^*$  of GaAs we get an energy difference of  $E_2 - E_1 = 16.6$  meV which agrees with the measured emission photon energy of 17.3 meV. The oscillations do not shift with the injection current and with the associated change in the upper subband population and Fermi-level. Therefore, unlike Shubnikov-de Haas-oscillations, they cannot stem from resonances of the Fermi-level with the Landau-levels.

It should be pointed out that direct resonant transfer between Landau-levels of different indices is forbidden. However, such transfer with a change of Landau-level index up to  $\Delta N = 9$  has been observed in photocurrent measurements on superlattices by Grahn [51]. Oscillations of the in-plane magneto-resistance of two-dimensional electron systems have been explained in the same way by enhanced intersubband scattering at Landau-level crossover [52]. Raikh and Shahbazyan [53] include in their theoretical model short-range disorder caused by interface roughness or impurities to mediate the momentum transfer required for inter-Landau-level scattering.

We have shown that the application of a magnetic field enhances the efficiency and reduces the linewidth of terahertz intersubband electroluminescence. These two effects together could facilitate stimulated terahertz-emission in a quantum cascade structure. Disorder scattering and electron-electron scattering which are considered as the governing non-radiative process are suppressed by Landau-quantization of the in-plane electron motion. We suggest that in-plane size quantization, as in a quantum dot cascade, would equally boost the emission performance. The efficiency as a function of magnetic field

exhibits oscillations stemming from a modulation of the scattering rate by a magneto-intersubband resonance.

The relevance of electron-electron scattering in terahertz quantum cascade structures has been a topic of lively discussion. Theoretical calculations based of Fermi's golden rule [39] and on a random-phase-approximation formalism [41] predict that scattering times in wide quantum wells can be as small as  $\sim 1$  ps. In an experiment on terahertz cascade emitters, the sublinear dependence of terahertz emission intensity on the injection current was explained by electron-electron scattering [54]. However, the comparably low electron sheet density around  $\sim 10^{11} \text{ cm}^{-2}$  in these samples was a source of doubt, if electron-electron scattering is really the dominant contribution.

A closer look at the magneto-transport experiments described above (Fig. 1.8) may resolve the above question. Electron-electron scattering is an elastic two particle process. This allows to distinguish it from the disorder related, elastic one particle processes. The latter can only take place when the Landau levels originating from subband 1 and 2 are resonant, in the notation of ()when  $N$  in the above equation is an integer. In contrast, an electron-electron scattering process of the type  $2,2 \rightarrow 1,1$  [55] can happen under consideration of energy conservation, when the Landau levels of system 1 is located exactly in the middle between two Landau levels of the system 2. In this case, one electron is scattered to the higher Landau level of system 1 gaining an energy of  $\frac{1}{2}\eta\omega_c$ , and the other electron is scattered to the lower Landau level of system 1 losing the same amount of energy. This process resembles to half integer resonances ( $N = \frac{1}{2}, \frac{3}{2}, \frac{5}{2}, \dots$ ) illustrated in Fig. 1.11.

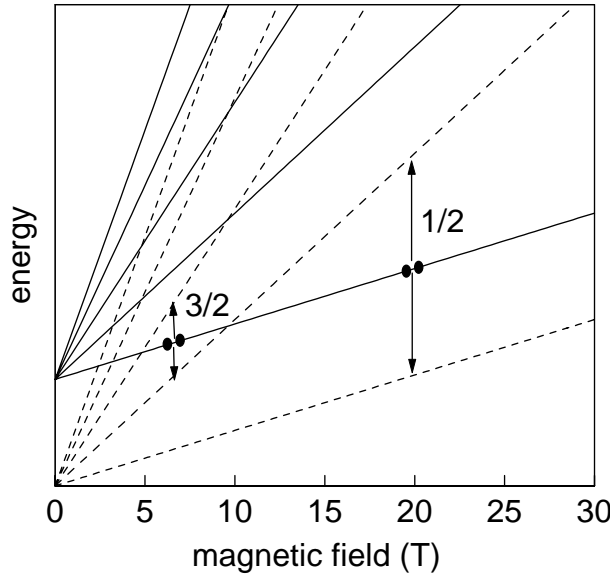
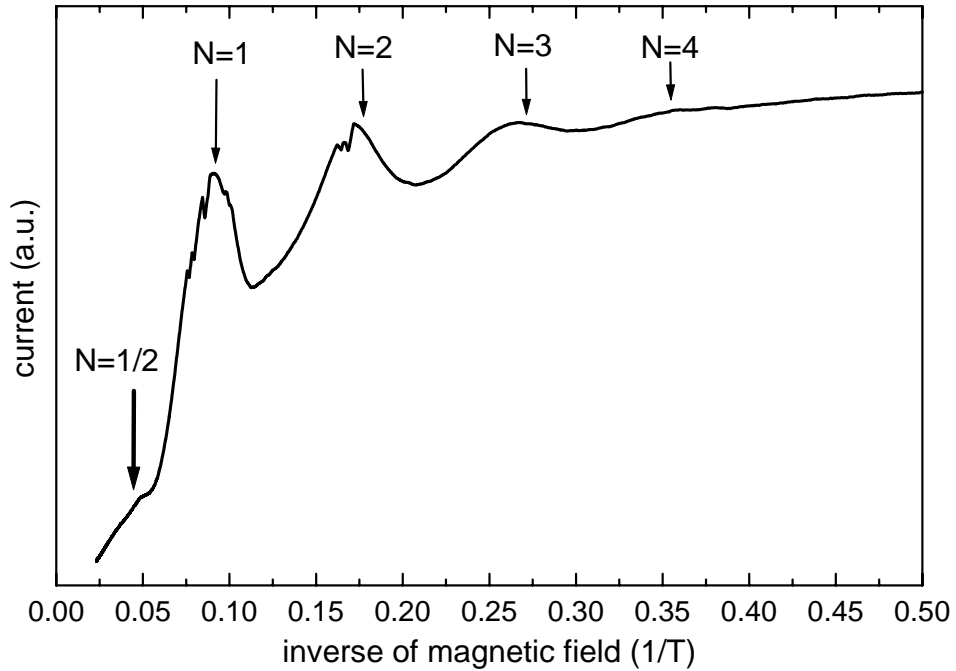


FIG. 1.11: Landau-fans originating from the subband 1 (dashed lines) and 2 (straight lines). The  $N = 1/2$  and  $3/2$  electron-electron scattering processes are marked with arrows.

As obvious from the previous data presented in Fig. 1.10 (b) & (c), these processes cannot be very strong because only the integer resonances are clearly visible. The highest probability to observe a half integer peak, which would be a clear indication of electron-electron scattering, can be expected for the  $N = \frac{1}{2}$  peak, since the peak amplitude increases with decreasing  $N$ . Looking for this resonance, high (pulsed) magnetic field experiments up to  $B = 40$  T have been performed on a pure AlAs sample [56], which exhibits sharp and magneto-intersubband resonances. The data plotted in Fig. 1.12 shows clear evidence of the  $N = \frac{1}{2}$  resonance. Its amplitude, however, is considerably smaller than that of the integer resonances. For electron-electron scattering, Kempa et al. [56] predict comparable amplitudes of the half integer and integer resonances, taking into account that both processes require a change of the electron momentum. The experiment thus reveals, that electron-electron processes are present in the sequential transport governed by 2-1 intersubband scattering, but they are not the dominant mechanism.



*FIG. 1.12: Current versus inverse magnetic field of pure AlAs sample. The resonances are labeled with the corresponding value of  $N$  [56].*

In spite of the convincing experimental results about the usefulness of magnetic fields for the suppression of Auger scattering processes in quantum cascade structures magnetic field experiments on PI structures failed for the following reason:

- In the low current domain these structures never showed any detectable FIR emission whose strength could have been enhanced by the application of a magnetic field. All PI structures remained dark.

- In the high current density domain which necessarily means high overall currents for the large sample areas involved the experiments are hampered by the Lorentz force on the bonding wires used for electrically contacting the samples. At larger pulse currents the wires usually could not stand the stress by the pulsing Lorentz force and broke.

### **resonant tunneling in the domain of high carrier densities**

The oscillatory motion of electrons in quantum mechanics is usually described by the evolution in time of wavepackets formed out of the stationary probability distributions found as solutions of the time-independent Schroedinger equation. In the many electron case this probability functions are usually reinterpreted as real carrier densities. Their oscillation in time now may be considered as a plasmon mode. While a single electron does not interact with itself, the simple reinterpretation of probability amplitudes, however, lacks to account for electron-electron interactions. The resulting dynamic screening effects instead shift the frequencies of every oscillatory motion of the electron system, as most prominently observed as the depolarization shifted intersubband resonance plasmon in FIR emission studies.

It is not a priori clear how big the influence of dynamic screening effect is on resonant tunneling and whether resonant tunneling by itself is a collective effect or at least supported by collective effects.

We have studied tunneling through resonant tunneling diodes (RTD) with very long emitter drift regions (up to 2  $\mu\text{m}$ ) [57]. In such diodes, charge accumulation occurs near the double barrier on the emitter side, in a self induced potential pocket. This leads to a substantial enhancement of the wave function overlap between states of the pocket and the RTD, and, consequently, to increased off-resonance current mediated by various scattering processes[58, 59, 60]. For the RTD with the longest drift region (2  $\mu\text{m}$ ), an additional strong current peak is observed between the first and second resonant peaks. We attribute this feature to intersubband transitions mediated by resonant emission of intersubband plasmons. **This is thus the first direct experimental proof of the plasmon decay mechanism proposed by Bakshi and Kempa.**

Three different samples were grown with emitter regions of 0.1  $\mu\text{m}$  (sample A) 1  $\mu\text{m}$  (sample B) and 2  $\mu\text{m}$  (sample C). Their measured IVs are shown in Fig. 1.13. The curves are rather similar except for the appearance of a strong peak (marked by an arrow ) between the first and second resonant peak in the sample with the longest drift region.

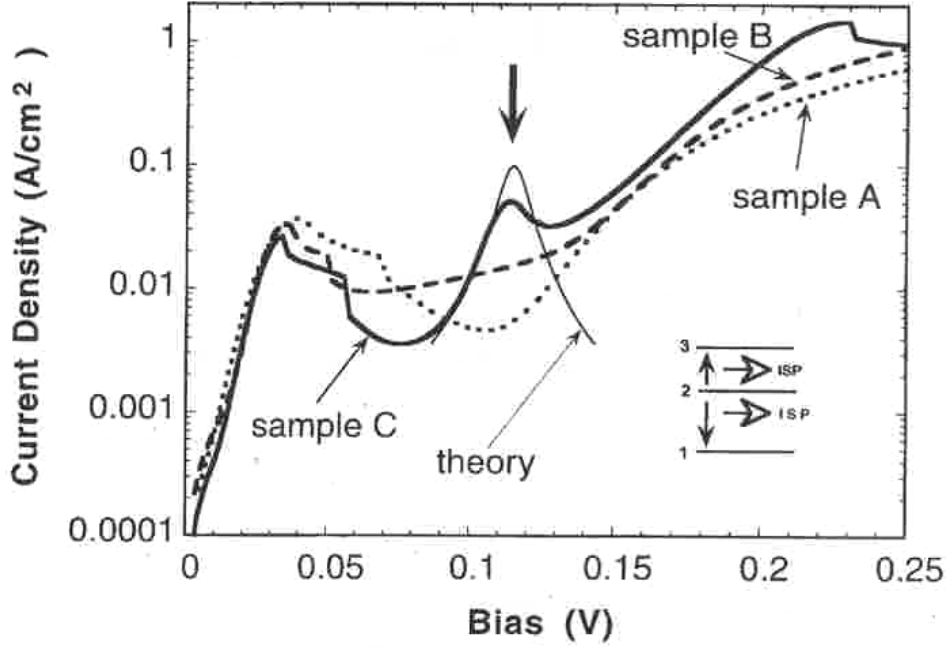


FIG. 1.13: Current density vs. the applied bias for three different emitter drift lengths of the RTDs. Inset shows a scheme of intersubband transitions in sample C, which lead to formation of the additional peak indicated by the arrow [57].

The results of self consistent band structure calculations for an externally applied bias corresponding exactly to the additional resonant bump in the current voltage characteristic of sample C are depicted in Fig. 1.14 and show the formation of a potential pocket on the emitter side of the RTD for the long drift region sample, in which carriers can accumulate. This accumulation of carriers increases the non resonant leakage of carriers through the emitter side barrier of the RTD and hence increases the number of carriers *within* the RTD. The large number of electrons inside the RTD now allows for electron-electron (i.e. Auger) scatterings [39] to mediate the intersubband electron transport necessary for electrons traversing the RTD under the bias conditions in Fig. 1.13.

The interpretation of the observed enhanced transition rate as it is also confirmed by detailed calculations for the structure C [61] involves the picture of the resonance of two intersubband plasmons [62]: Considering two intersubband levels in a non inverted carrier distribution situation absorption of energy by the two level system is upshifted by the depolarisation shift as discussed earlier. The depolarization shift measures the fraction of the absorbed energy transferred to the collective motion of electrons. The remaining portion of the absorbed energy is used to transfer a single electron between the two subbands.

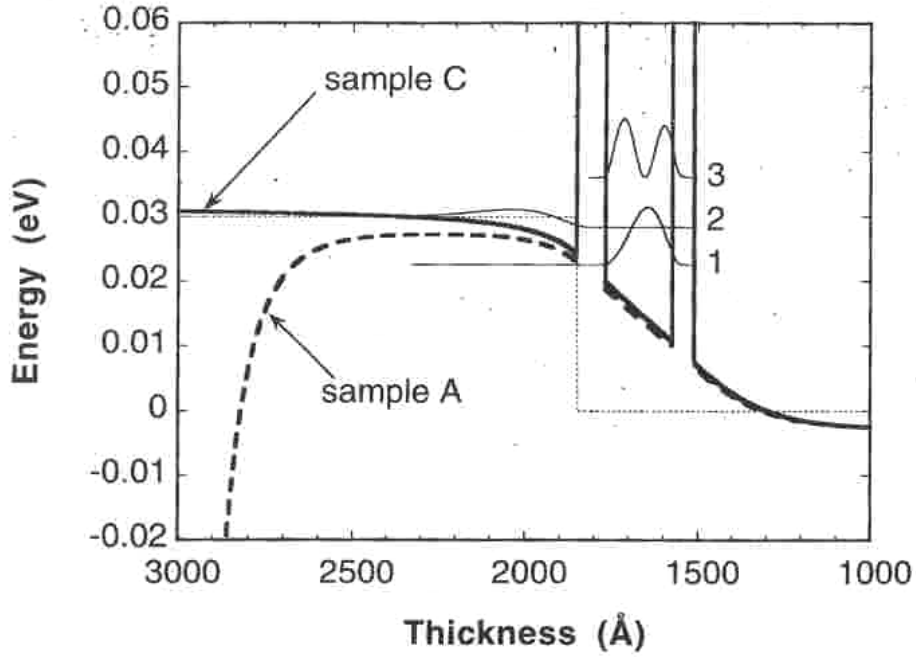


FIG. 1.14: The conduction band edge for samples A and C versus distance in the vicinity of the double barrier for the bias corresponding to the additional peak shown in Fig. 1.13. Dotted line represents the quasi-Fermi level. The thin solid lines show squares of the wave functions of the relevant subbands [57].

When the population is inverted the depolarization shift becomes negative for the net downward transitions of single electrons, i.e. the excess energy again is transferred to the plasmon mode. Thus collective oscillations associated with intersubband plasmon (ISR) resonance are generated whenever electrons are transferred between subbands.

The most efficient buildup of these collective excitations can occur if both, downwards and upwards, electron transitions occur simultaneously. This can happen in a three-subband scenario [6] with a large population in the middle (2) subband, and almost empty bottom (1) and top (3) subbands. In this situation the spectral response consists of two peaks, one due to the ISP of the upper pair (3-2), upwards depolarization shifted, and one due to the ISP of the lower pair (2-1), downwards polarization shifted from the corresponding intersubband separation. For a certain definite difference of the two interlevel pairs the two intersubband peaks merge. This is an attractive crossing, reflecting the resonant (stimulated) emission of *two* ISP. This can provide an efficient mechanism for off-resonant current enhancement in RTDs. The observed off-resonant current peak is fully consistent with the model of Bakshi and Kempa for PI [6]. The bias sensitivity, which leads to the peak formation in the IV-characteristics, is a result of the stringent requirement for a proper subband configuration. This subband configuration, shown schematically in the inset of Fig. 1.13 can always be achieved in our RTD at a particular bias, not far from the middle point between the two current resonant peaks.

### a vertical cascaded structure other than square wells

We have previously demonstrated THz emission from parabolic quantum wells up to lattice temperatures structures of 200 K, where electrons are injected laterally in the parabolic well of carriers depending on the carrier energy. In contrast to square wells, an extraction at low energies is specially critical, because the tunneling barrier gets thicker for lower energies, a direct consequence of the shape of the wells. There is a tradeoff between an ideal parabolic shape giving an ideal equidistant subband spacing for all subbands and a thinner tunneling barrier giving higher current densities. A higher current gives more emission, before the structure starts to break into high and low field domains.

The problem of ineffective removal of electrons from the ground state in each well can be alleviated somewhat by replacing the single barrier by a short period superlattice which acts as an electron energy filter. The basic operating principle of a superlattice energy filter is shown schematically in Fig. 1.15. The superlattice consists of multiple quantum wells with monotonically varying thicknesses coupled by thin tunneling barriers. Each narrower quantum well has a higher energy for its lowest bound state so that, at zero bias (Fig. 1.15 (a)) a stair case of energy levels is created. If the superlattice has been properly

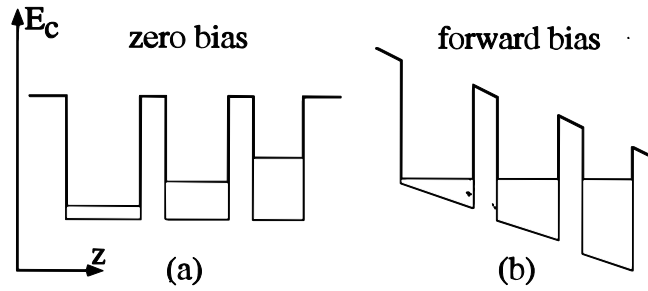


*FIG. 1.15: Schematic band diagrams of a simple superlattice energy filter for (a) zero bias and (b) forward bias.*

designed, this staircase of levels will align under a forward bias and allow for a comparatively large tunneling current to flow under operating biases. At other biases, when the levels are not aligned, the electron current is drastically reduced since there is not a series of available energy states for tunneling and the overall thickness of the filter structure is quite large (around 200 Å).

Fig. 1.16 shows the conduction band structure of a triple parabolic well with different grades of asymmetric thicknesses. For the case without external bias (Fig. 1.16) we can see the parabolic behavior at low energies and the shift of the former equidistant intersubband energies from the left to the right side, the more asymmetric the parabolic well.

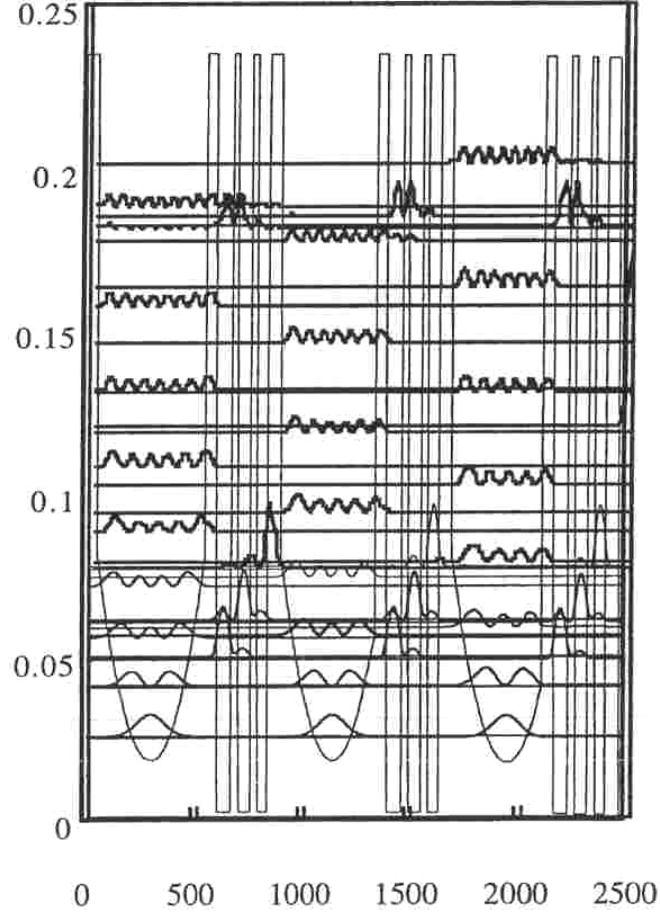


*FIG. 1.16: 3 parabolic wells without external bias, the degree of asymmetry is increasing from left to right. The figure shows energy (eV) as a function of the growth coordinate (in Angstrom) and the square of the wave functions.*

Fig. 1.17 shows the identical structure with an external bias. The tradeoff between parabolic behavior and reasonable tunneling currents can be seen by looking onto the distance from the lowest state in the parabolic well and the first square well in the injector region. The distance from the center of the well to the first well is given in Fig. 1.16 (in Angstrom).



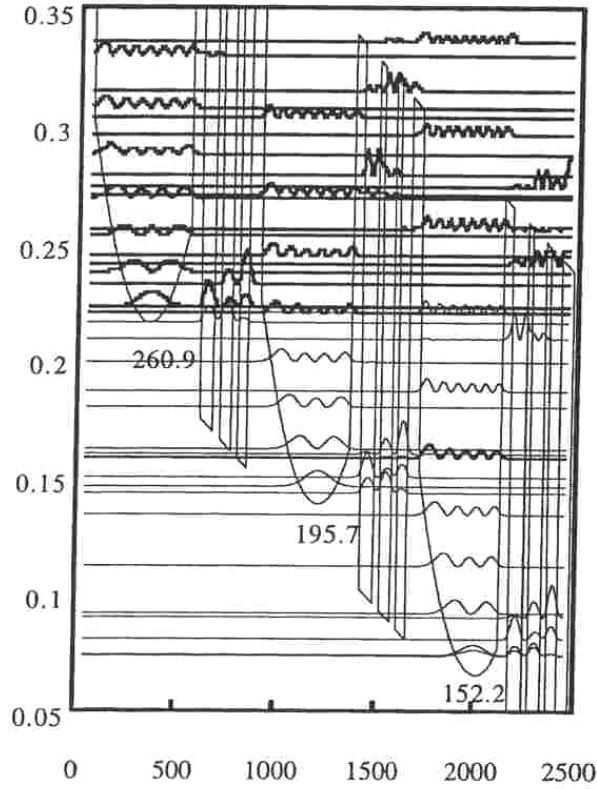


FIG. 1.17: Parabolic wells with external bias, the degree of asymmetry is increasing from left to right. The distance from the center of the well to the first well is given in Angstrom.

The realization of multi-parabolic quantum well structures is done by molecular beam epitaxy. Parabolic quantum wells, from the grower's point of view, can be realized in two ways [63]:

- Analog growing by continuously changing the flux of the Aluminum by increasing/decreasing the cell temperature
- Digital grading the composition of the semiconductor by using a unit of e.g. 2 nm and appropriate mixing of layers of GaAs and AlGaAs with a fixed Aluminum composition.

This digitization allows for the combination of slow variations in the Aluminum content, like in parabolic wells, with abrupt changes, like in double barrier resonant tunneling diodes, superlattice structures, or more sophisticated designs like quantum cascade devices. We have chosen the latter technique with a digital step size of 15 Angstroms.

The first realized sample consists of a parabolic quantum well with 300 Angstrom from the barrier to the center of the well on the injection side and 105 Angstrom on the extraction side. The curvature of the parabolic well is the same on both sides. In the existing structure 35 identical parabolic wells are cascaded and separated by a tunneling injector structure. The structure was grown on highly n-doped material to realize a homogeneous

electron injection. A top layer with a carrier concentration of about  $1\text{-}2 \times 10^{18}/\text{cm}^3$  is to ensure a defined carrier injection. The well material is doped homogeneously to achieve an overall doping concentration in the active region of about  $1 \times 10^{16}/\text{cm}^3$  electrons. The barrier material is not doped intentionally.

For current-voltage measurements the samples are processed into small cylindrical mesas to probe the electrical behavior of the structure. Fig. 1.18 shows the current vs voltage and current density vs voltage behavior at low temperatures for two different mesa sizes to demonstrate the homogeneous injection of the electrons into the structure. The current densities are literally identical, then only detectable differences are in the regime, where the structure breaks up into high and low field domains. This well known behavior reproduces a variety of peaks. The exact number of peak has to be 35, so each well should be resolvable. The different mesa sizes are given in Fig. 1.18. The IV measurements are performed at cryogenic temperatures.

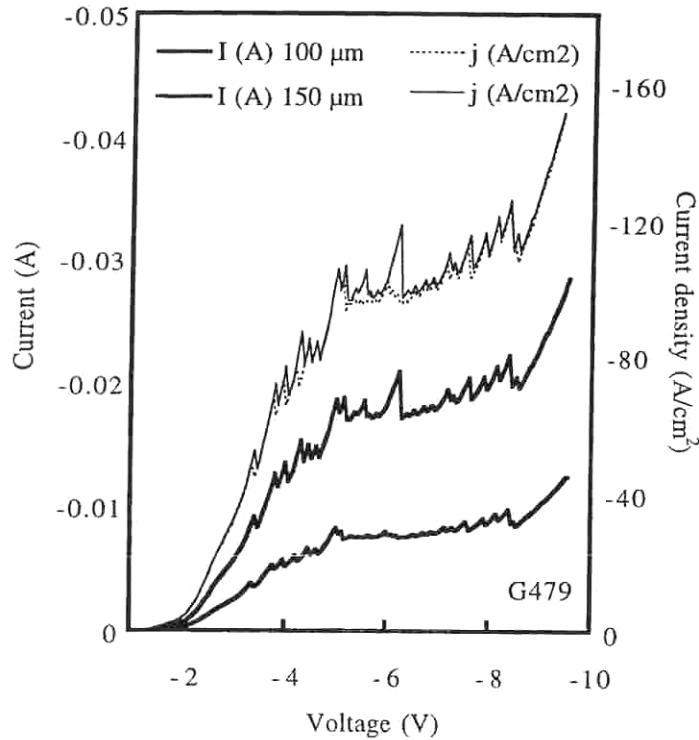


*FIG. 1.18: Current voltage characteristics and current density vs. external bias for two circular mesa structures processed into sample G479. Textbooklike behavior proofs high efficiency of the chirped superlattice design for resonant tunneling phenomena: A section of strongly superlinear current increase through alignment of energy levels is followed by a breaking up into high and low field domains at higher bias. The mesa diameter are 100 and 150 microns, respectively. The merely identical current density plots for the two different mesa sizes indicate a highly homogeneous current distribution within the samples. The measurements are performed at liquid Helium temperatures*

First emission experiments were performed with the cascaded plasmon structure sample G479 to repeat experimental results of Maranowski et al. [64]. We have processed the sample into stripes of  $25\text{ }\mu\text{m}$  width and  $1000\text{ }\mu\text{m}$  length. The emission sample consisted of 8 stripes giving a total emission area of about  $0.228\text{ mm}^2$ .

The emission spectrum, Fig. 1.19 is measured with an InSb detector. The spectrum consists of a main peak at  $150\text{ cm}^{-1}$  corresponding to the plasmon energy of the parabolic band structure. This result is in agreement with the measurements by Maranowski et al. [64]. The additional emission line at  $60\text{ cm}^{-1}$  can be identified as due to transitions between shallow impurity states as it corresponds to the impurity ionization energy close to  $5\text{ meV}$ .

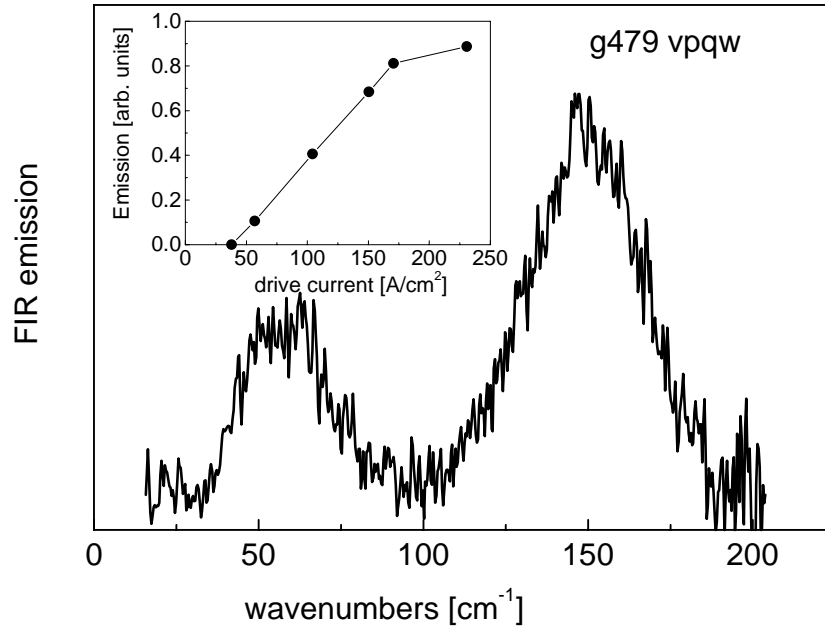


FIG. 1.19: Emission spectrum of 35 cascaded parabolas (sample G479) at  $4.2\text{ K}$  measured with an InSb detector. Inset shows linear increase of emission peak power below the bias where structure breaks up into domains of high and low electric fields (see Fig. 1.18)

## measurement setups.

In the later stages of the project two independent measurement setups were available to record terahertz emission spectra which are explained in the following:

### Fourier transform infrared spectroscopy

Emission spectra of the terahertz devices are recorded with a Fourier-transform infrared (FTIR) spectrometer [65], schematically depicted in Fig. 1.20. The light is divided by a beam splitter into two beams perpendicular to each other, forming the two arms of a Michelson interferometer. At the end of one arm is a fixed mirror, at the other end is a

movable mirror. The two beams are recombined, and directed to the detector. The interferogram, i.e. the detector signal as a function of mirror position, is recorded. The spectrum is obtained by Fourier transformation of the data. The spectral resolution is only limited by the mirror path length. The maximum available resolution is 0.016 meV. The spectral range, on the other hand, is determined by the sampling rate or by the density of data points in one mirror scan. One advantage of Fourier transform spectroscopy over conventional (narrow band) spectroscopy is its high sensitivity. The detector receives always a large broadband signal - on average half the maximum signal at zero path difference of the two beams.

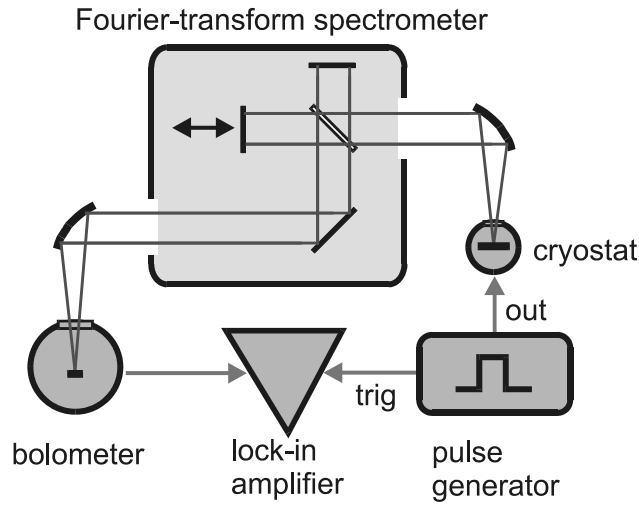


*FIG. 1.20: Fourier-transform infrared spectrometer and set-up for mid-infrared and terahertz emission measurements.*

The system used in the emission experiments is a NICOLET (Magna IR 850) equipped with a Si-beamsplitter for terahertz radiation. The low-signal spontaneous emission measurements were done in the amplitude modulation step scan mode. The mirror stops at discrete positions and the detector signal is registered at the modulation frequency by a lock-in amplifier. The modulation technique reduces the noise significantly. Spontaneous terahertz emission is particularly weak, because of the small emission rate, proportional to  $(\eta\omega)^3$  and the small photon energy (and thus the small amount of heat generated by one photon on the bolometer). It is in the range of a few nanowatts. To measure the spectra, long averaging times of 1 s per data point had to be applied.

The complete set-up is sketched in Fig. 1.20. The liquid He-flow cryostat which contains the sample is equipped with a window (aperture: 25.4 mm) made of polyethylene or TPX-polymer for terahertz radiation. The emitted light is collected by a Au-plated off-axis parabolic mirror. The light is transmitted through the spectrometer, and then focussed by another parabolic mirror on the bolometer. The spectra in the terahertz frequency regime are heavily distorted by water absorption in the atmosphere. Therefore the whole beam path is sometimes purged with dry nitrogen gas.

## InSb cyclotron resonance spectroscopy

Terahertz emission spectroscopy is alternatively performed with a set-up based on an InSb-cyclotron resonance detector [46]. The spectral response of this photoconductive detector is peaked at the cyclotron energy  $\eta\omega_c$ . It originates from transitions between neighboring Landau-levels and between the associated shallow impurity levels. It can therefore be tuned by a magnetic field. The measurement set-up, depicted in Fig. 1.21, allows to apply magnetic fields to the emitter and detector independently. The radiation is guided from the emitter to the detector in a closed light pipe. The whole system is immersed in liquid He. The electronics consists of a pulse generator to drive the emitter and a lock-in amplifier to record the detector signal.

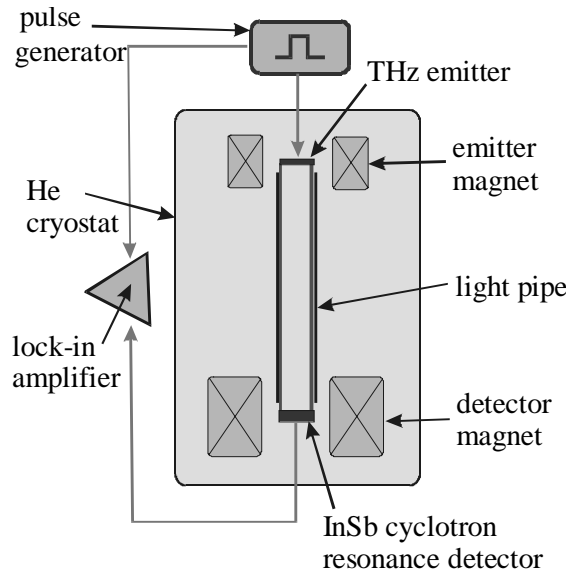


*FIG. 1.21: InSb-cyclotron resonance terahertz spectrometer*

A plot of the spectral response for the InSb detector is shown Fig. 1.22. The data was obtained with a narrowband GaAs-cyclotron resonance emitter. While the emitter is set to various fixed photon energies by choosing the emitter magnetic field, the detector is continuously tuned and thus represents a spectrometer. The spectral resolution is given by the splitting of the two peaks (Landau-level transitions and impurity transitions) of  $\sim 1.3$  meV. It can be increased to  $\sim 0.25$  meV by cooling the detector to 2 K, where the Landau-level peak vanishes due to carriers freeze-out.

The two methods, which have been employed for terahertz emission, the Fourier-transform spectrometer and the InSb cyclotron resonance spectrometer, have very different characteristics, as listed in Table 1.1 at the end of the chapter.

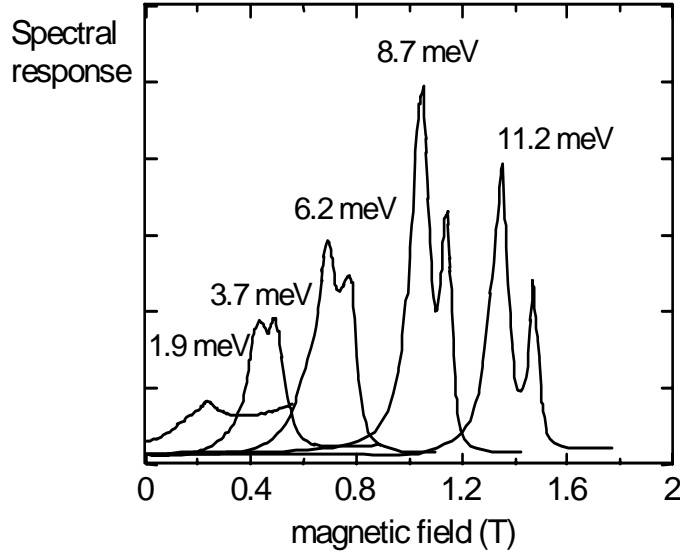


FIG. 1.22: InSb detector signal as a function of magnetic field for different emitter photon energies given in meV. The width of the emission line is 0.25 meV.

For a precise characterization of the peak shape and linewidth of a given emitter, the use of the Fourier-transform spectrometer is imperative for its higher resolution and larger spectral range. In addition, temperature dependent measurements are only possible in the flow-cryostat of the Fourier-set-up. However, water absorption and modulated reflected background radiation can seriously modify the spectra and generate artefacts. In the InSb-system, these kinds of distortion are absent since the light is transmitted through liquid He, and all parts of the spectrometer are cold. Intensity measurements comparing different samples rely on the reproducibility of the optical alignment (of sample lenses, beamsplitter and mirrors and detector), which is generally not guaranteed. In the InSb-system, no alignment is necessary, because no focusing elements are involved. The radiation is guided in a closed lightpipe from the emitter to the detector.

The sources of distortion listed for the InSb-system can be handled more easily. The electrical pick-up from the emitter- into the detector circuit is strongly suppressed by subtracting the signals for opposite detector current directions. The evaporation of He can be avoided by using small emitter samples which require comparably low electrical input powers. Since the terahertz quantum cascade structures do not require a magnetic field, the emitter magnet is usually switched off or used to compensate the stray field from the detector magnet. However, the emitter magnet can be readily employed to investigate the transport and emission of the cascade structure in a magnetic field). Applied perpendicular to the layers, a magnetic field changes the in-plane electronic motion without affecting the designed energy scheme in the growth direction. This should modify the non-radiative intersubband scattering processes.

While both setups have proven to be reliable spectroscopy tools for more or less conventional semiconductor heterostructures new types of problems were encountered on both setups when experimenting on the PI structures:

- refractive index modulation of the samples: under heavily pulsing condition the sample characteristics from the puls-on to puls-off state may differ considerably with respect to a carrier flooding of the active region and/or a broadening of the phonon spectrum by sample heating. In the FTIR this two effects severely modulate the absorption characteristics of the PI samples and the recorded spectra are therefore a mixture of real FIR emission of the samples and modulation of the background radiation absorption in the signal path. Due to instrumental algorithms used absorption peaks may appear as emission peaks in the spectral plots. The question emission vs absorption can not be clarified by *any* means as long as lockin technique is required for separation of the background spectrum, i.e. no boxcar technique possible. In this case comparative measurements in the InSb setup which is background radiation independent were required.
- It is especially difficult to deal at the same time with very small amounts radiation emission and large current densities and overall currents, respectively. There always has to be made a tradeoff between thermal constraints to the liquid helium setup and the best operating conditions for lockin-amplifiers
- impedance matching is not possible so coupling can not be avoided to zero. This hinders the determination of shifts of emission signals sitting on large background signals. In the high input power regime the speed advantages of the InSb setup often were lost due to He bubble formation. The resulting increase in measurement noise strongly increased the required measurement times.

<b>Characteristics</b>	<b>FTIR</b>	<b>InSb</b>
Spectral range	3 meV...40 meV	3 meV...27 meV
Maximum resolution	0.016 meV	1.3 meV
Typical acquisition time per scan	10 min (resolution: 1 meV) 40 min (resolution 0.25 meV)	10 min
Sources of distortion	– water absorption – room temperature radiation – optical alignment	– electrical pick-up – He-evaporation at high powers
Temperature range	4.2 K...300 K	4.2 K
Other	–	Application of magnetic field

*Table 1-1. Characteristics of the two terahertz spectrometers, the Fourier transform spectrometer with the Si-bolometer (FTIR), and the InSb-cyclotron resonance spectrometer*

# Experimental Part 2: Plasma instability

## Quasidoping: the sample G428

The emission measured on the sample G301 (see Introduction) brought no evidence for the appearance of a PI. The very weak emission signals hindered a systematic scanning of the dependence of the emission on the bias voltage to find any nonlinear dependence. The plasmon frequency of this structure is in the same spectral range as the observed subband separations. The doping of the active plasmon resonator of G301 was quite high with values of a few times  $10^{17} \text{ cm}^{-3}$ , but considered necessary to obtain the required bandstructure and a high Fermi level. Highly doped active regions, however may result in very high loss rates for plasma oscillations. To avoid high doping modulated bandstructures can be grown which mimic the effect of doping by a bandstructure engineered band bending, thus without introducing impurity scattering.

A new sample was therefore designed and grown (G428) without doping in the active region but compensating for the doping by a parabolic potential. The implementation of such a parabolic transition region also prevents unwanted bend bending under different bias conditions. The injection barrier in G428 was 1.2 nm AlGaAs with an Al concentration of 30% as compared to 4 nm of AlAs in the previous structures. The reduction of the injection barrier was aimed at a considerable increase of the current.

The result of transport measurements of G428 are shown in Fig. 2.1, where the current and the derivative of the current are plotted as a function of the bias voltage. In the positive bias

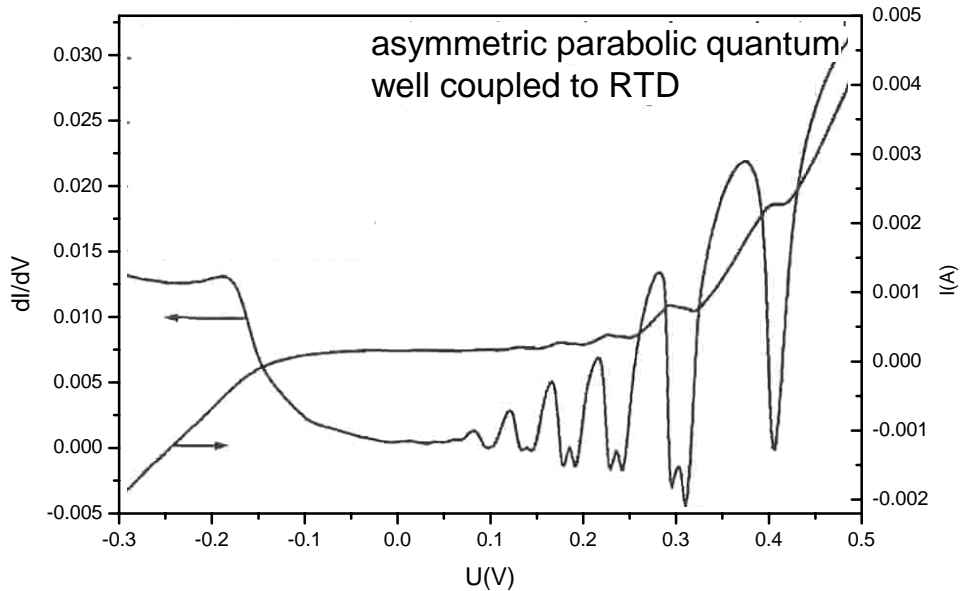


FIG. 2.1: Current and conductivity-voltage characteristic for sample G428. The sample is nominally undoped in the active region; quasidoping by a semiparabolic potential well region is used instead (see g389 likewise, Fig. 1.4)



direction a spectroscopy of the levels above the Fermi level is performed. Each peak in the current represents the passing through a resonant level. For negative bias (forward direction) the levels below the Fermi level are scanned. This bias provides the situation for the extraction through the levels in the RTD and the pocket. The resonances in the derivative have become larger than in the previous sample G301, but are still not visible clearly in the current. The extraction through the RTD is evident in the derivative at a bias of 0.2 V. This is the position to look for an instability.

The following emission measurements, however were not successful. Over a broad range of applied bias voltages no traces of intersubband like emission could be found.

The measured transport properties, instead, were compared with calculations of the collaborating Boston group [22]. The main aim was to get more insight in the efficiency of the extraction process and signatures of plasma instability in the current. The calculations provide IV-curves and the positions of the energy levels and their wavefunctions. It is important to note that the energy levels are shifting with bias and that it is quite difficult to predict precisely the position of the extraction resonance together with the optimum level separation needed for the instability.

In a first step to optimize the modeling procedure mesas of three different sizes, 10  $\mu\text{m}$ , 30  $\mu\text{m}$ , and 450  $\mu\text{m}$  were processed. A direct comparison of the IV-curves for the different mesas gives a possibility to extract IV-curves which are not influenced by the size dependent series resistances. The extracted conductivity independent of geometry effects is necessary for the comparison with calculations. Fig. 2.2 shows a comparison of a calculated IV-curve with an experimental curve for a 30  $\mu\text{m}$  mesa of G428 in forward bias direction. It is evident from Fig. 2.2 that the agreement is excellent.

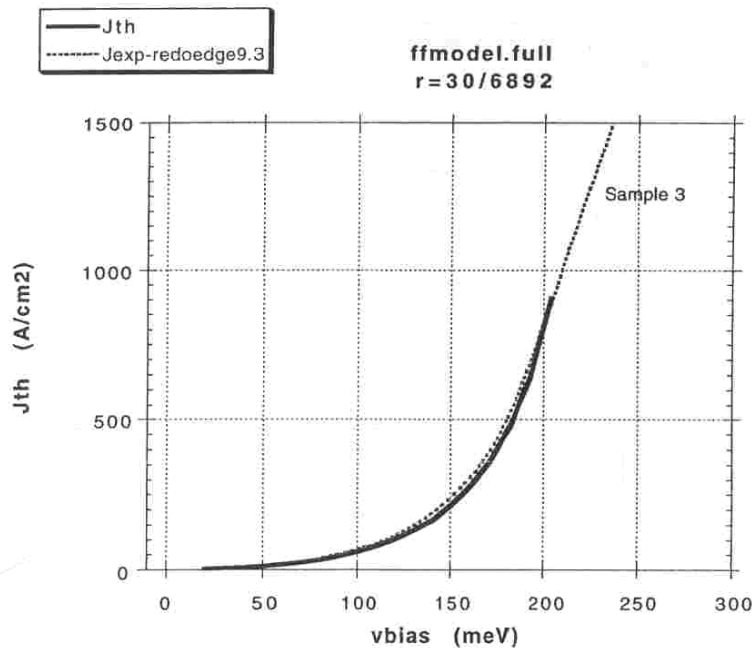


FIG. 2.2: Measured current density for sample G428 in forward direction in comparison with theoretical calculations (after Bakshi, private communications).

## highly doped injector and collector regions: the sample G494

The new sample G494 (Fig. 2.3) kept the quasidoped active region and parabola of G428 but with a higher real doping of the collector and injector regions, i.e.  $2.4 \times 10^{18}$  for G494.

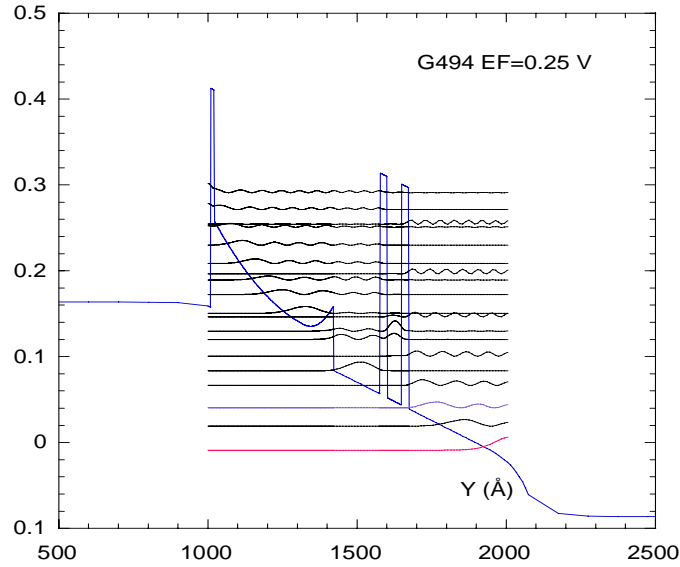


FIG. 2.3: Unit cell of the sample G494 including the electronic wave functions for an external field of 0.25 V

The bandstructure of sample G494 is shown in Fig. 2.3 under bias for the situation when the extractor level is close to resonance with the second level of the quantum well in the active region. However, it is evident from Fig. 2.3 that the current can also path through higher lying levels. This explains the fact that the current through the structure is quite high but the resonance due to the RTD ground state extraction is weak.

This behavior is clearly visible if one looks at the derivative of the IV-curves for the samples G428 and G494. Fig. 2.4 shows a comparison of the IV-derivatives of the two samples for  $10 \mu\text{m} \times 10 \mu\text{m}$  mesas at liquid helium temperatures. For positive bias the samples show similar behavior, the observed resonances are due to the interaction of the RTD state with the energy levels in the active region, where the current is flowing from the RTD into the active region. For negative bias a single broad structure appears which is hardly visible for the sample G428 but well pronounced for the sample G494. The higher doping of G494 also leads to higher currents. The broad structure can be assigned to the case where the RTD level is resonant with the second level of the active region in the well. This feature is a prerequisite of a strong carrier - carrier interaction in the different levels of the quantum well. The feature is rather weak and it is not clear whether it is correlated with resonant plasmon excitation. For sample G428 it appears at about 0.2 V and is very weak. For sample G494 the effect is considerably stronger and broader, appears at about 0.3 V and contains the same additional features. There is a weak minimum after the maximum, which could be a signature of charge accumulation due to plasmon excitation. Charge accumulation leads to a reduction of current.

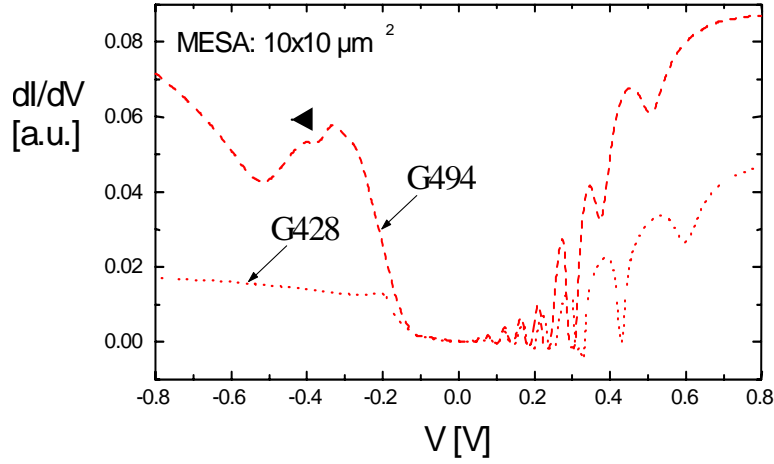


FIG. 2.4: IV derivatives of sample G428 and G494 for positive and negative bias.

The emission studies on sample G494 again were performed with the InSb photoconductive detector at liquid helium temperatures for series of bias conditions. As a first attempt to increase the overall emissive area mesas with  $6 \times 60 \mu\text{m}^2$  dimensions were fabricated and electrically connected in parallel. The results of emission measurements given in Fig. 2.5 show only a small signal at an energy around 15 meV with a FWHM of 8

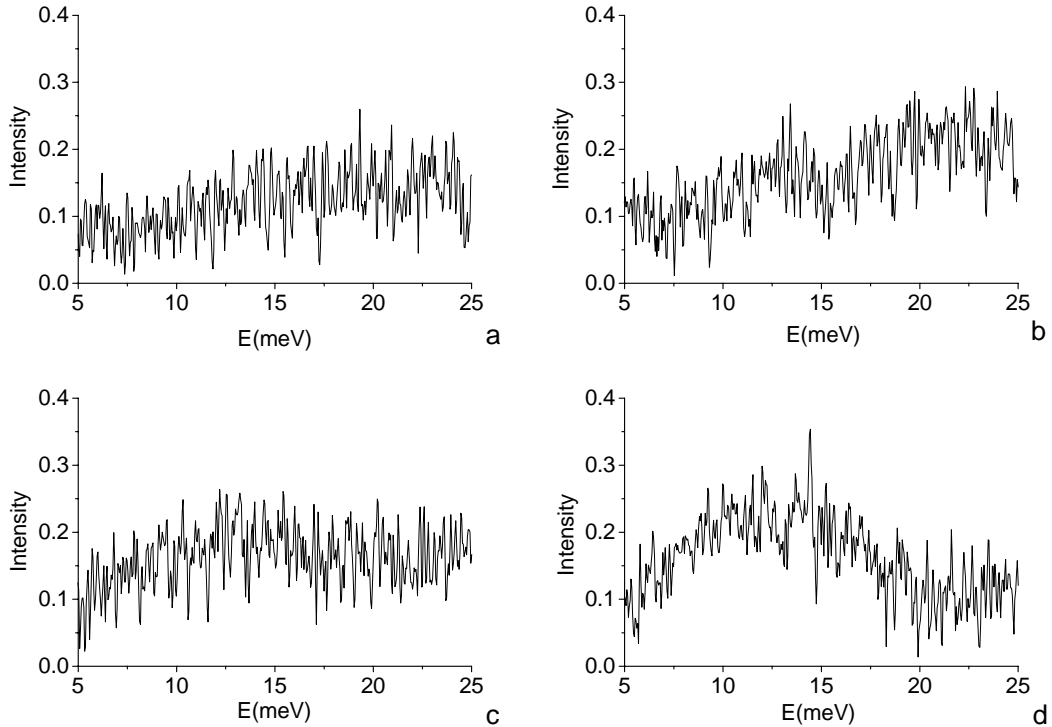
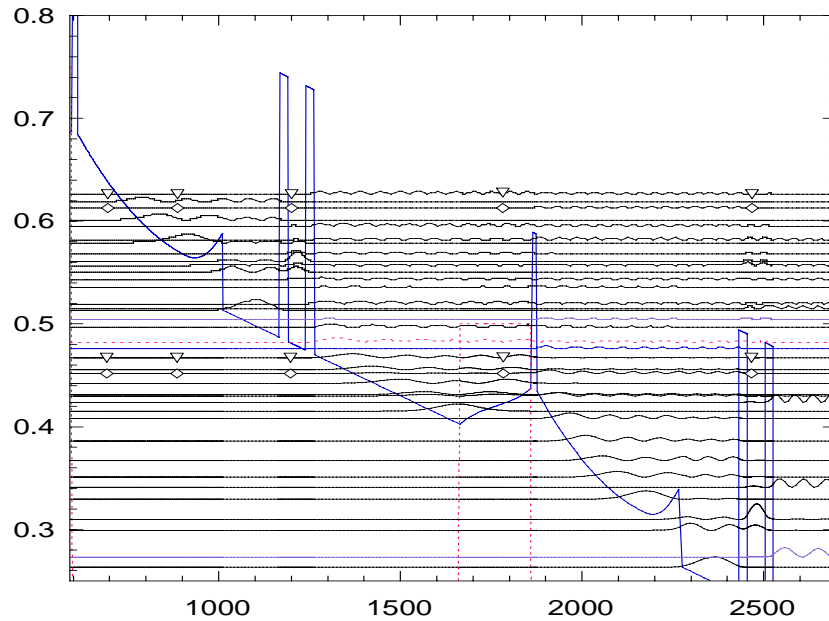


FIG. 2.5: Emission spectra of 15 mesas ( $6 \times 60 \mu\text{m}^2$ ) of sample G494, electrically switched in parallel at  $V=0.3 \text{ V}$  ( $16.8 \text{ A/cm}^2$ ),  $V=0.6 \text{ V}$  ( $52.0 \text{ A/cm}^2$ ),  $V=0.9 \text{ V}$  ( $87.1 \text{ A/cm}^2$ ),  $V=1.19 \text{ V}$  ( $122.0 \text{ A/cm}^2$ )

to 10 meV. Negative electric fields starting with the field value of the pronounced peak up to fields of about 1.2 V were used. The emission spectra show a very weak feature for the lower bias fields until a broad emission peak evolves at energies around 15 meV. The intensity is very weak, estimated of the order of  $10^{-10}$  W. The observed spectra are not correlated with subband transitions in the quantum well of the active region. The spacing of the subbands is about 25 meV, which corresponds to radiation emission in a frequency range where the InSb is not sensitive. Integral intensity measurements with a Ga doped Ge broadband detector show only a weak signal in the frequency range between 15 and 30 meV indicating no significantly higher emission at the higher energies.

### cascading of PI modules: the sample G534

One of the main issues was to increase the emission intensity by increasing the gain of the PI structure. One way of achieving this goal is by repeating the active structure. This cascading - as it is successfully applied for quantum cascade lasers - enables the same electron to run through the same active region  $n$  times,  $n$  referring to the number of stages in the sample. The structure on which cascading was first tried was a re-growth of the sample G494 described above. The unit cell of the new structure is shown in Fig. 2.6 for a specific external field.



*FIG. 2.6: Conduction band diagram for sample G534 under bias. 5 periods of the active structure of G494 were cascaded for this sample.*

For sample G494 contacts were made of highly doped GaAs-layers on both sides of the structure. This convenient technique cannot be used for a cascaded structure. For the cascaded scenario a different doping concept has to be applied. The structure (shown

unbiased in Fig. 2.7) was grown by molecular beam epitaxy in the digital alloy approach. A detailed layer sequence is given in the appendix. For this particular structure (G534) n-doped GaAlAs layers have been used to combine the bridging regions between the different stages. The aluminum concentration in these layers is increased linearly towards the injection barrier to remove any band offset at the border to the parabolic part of the structure.

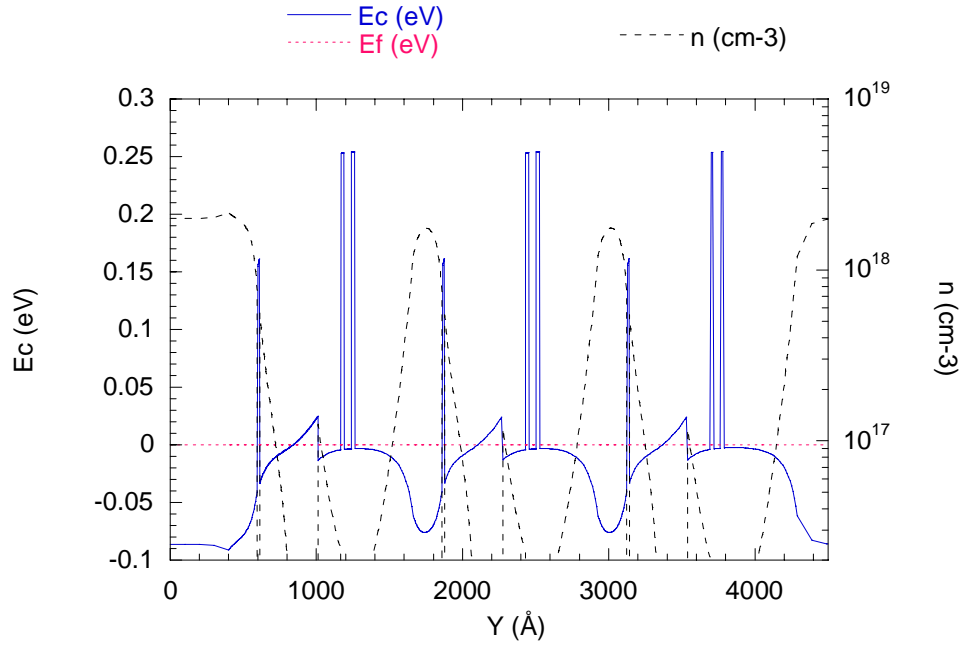


FIG. 2.7: Conduction band diagram for the cascaded sample G534 without external bias. The free carrier concentration (broken line) shows where the carriers are located.

A conduction band diagram without external bias shows the doping profile of this sample in Fig. 2.7. The active region and the RTD are clearly seen in the center of the structure, the bridging is done by introducing a high doped region between RTD and the injection barrier. The main problem in this design is the fact that there is a big uncertainty in the amount of doping to introduce in the bridging regions. When the doping concentration is too low, the structure must be overbiased to get sufficient current running. This overbias leads as a direct consequence to a misalignment in the extractor region, followed by a breaking of the extended states in strongly localized ones, as in low doped quantum cascade injectors. On the contrary introducing too much doping leads to the situation, where a constant electrical field conditions cannot be applied to the sample. In the worst case only one cascade can be depleted and the Fermi level remains constant within the rest of the active regions.

To prepare the samples for IV measurements, both highly doped layers (emitter and collector) have to be provided with ohmic contacts. Therefore they were processed in two steps. First the material over the deeper contact layer (collector) was partially removed by wet etching. Then the ohmic GeAuNiAu contacts were evaporated and after this alloyed,

by heating the samples at 430° C for three minutes. Before each step the surface was provided with a lithographic mask, to get 10 x 10  $\mu\text{m}^2$ , 30 x 30  $\mu\text{m}^2$  and 100 x 100  $\mu\text{m}^2$  mesas. After processing the samples were cleaved and bonded.

Fig. 2.8 shows the measured current voltage characteristics and the differential conductivity of the sample G534. At positive voltage there are the same oscillations found as in the sample G494, but washed out. At negative bias the main peak in the differential conductivity is now found at 1000 mV, while it was at 300 mV on the noncascaded but otherwise identical design G494. The positions of the peaks therefore do not scale by a factor of five thus matching the fivefold cascading of G534. From the current voltage characteristics of G534 we have to assume that only three cascades are depleted while the rest of the structure is flooded with electrons. This renders the conclusion that cascading so far was not very successful.

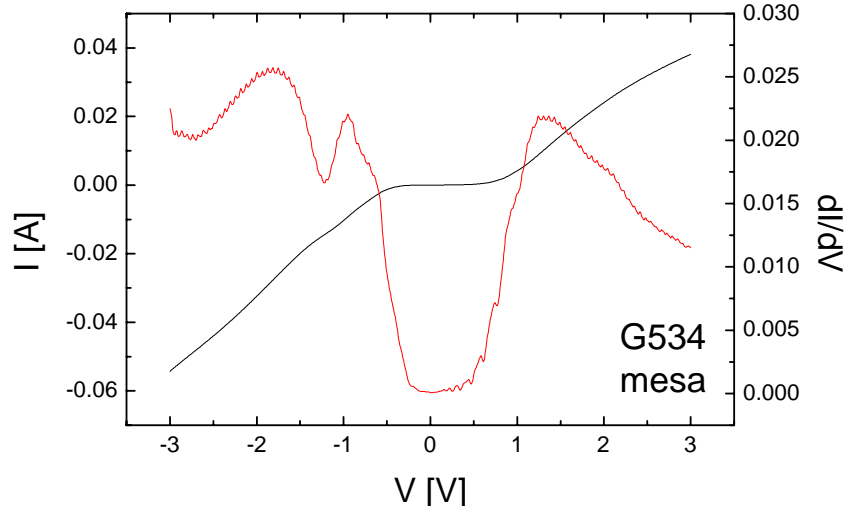


*FIG. 2.8: Current voltage characteristics and the derivative  $dI/dV$  versus voltage for a mesa structure of the fivefold cascaded sample G534*

The same emission experiments as for G494 were performed with the cascaded structure G534 which has basically a similar bandstructure and are shown in Fig. 2.9. The observed emission spectra look similar to the previous ones and show again a broad peak below 15 meV in good agreement with results of sample G494. The observed emission is most likely due to transitions between higher lying energy levels, i.e. above the quantum well levels. The expected increase of intensity by a factor of five, however, is not observed, the emitted intensities are similar for both samples.

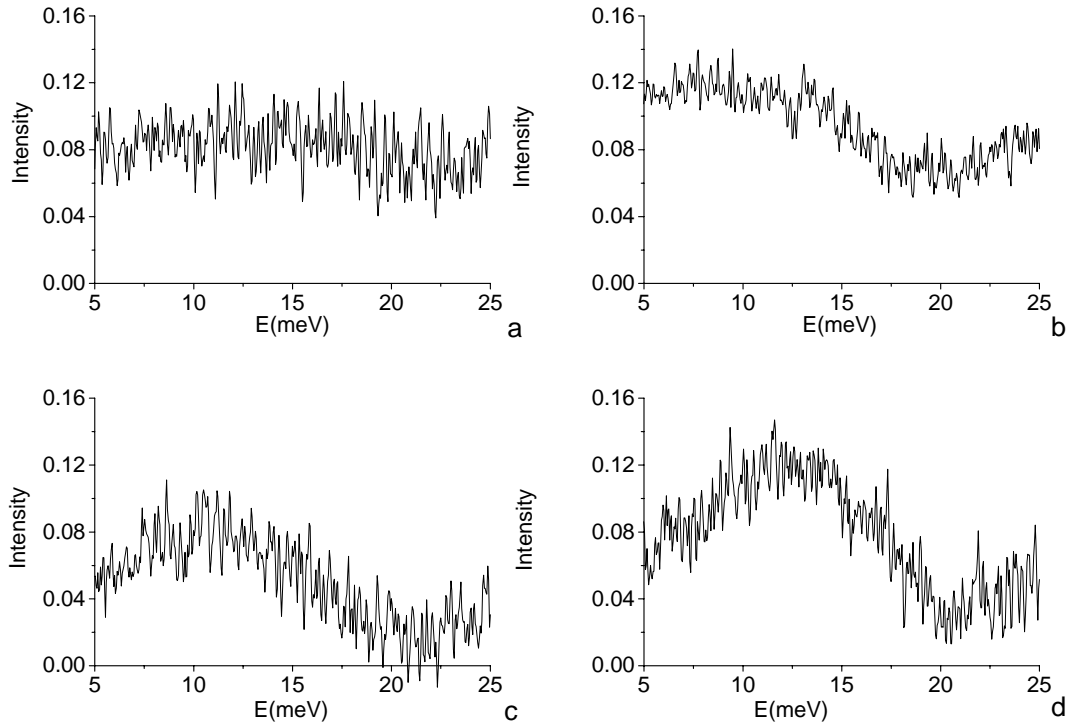


FIG. 2.9: Emission spectra of 11 mesas ( $6 \times 60 \mu\text{m}^2$ ) of sample G534, electrically switched in parallel at  $V=0.9 \text{ V}$  ( $56.9 \text{ A/cm}^2$ ),  $V=1.1 \text{ V}$  ( $83.1 \text{ A/cm}^2$ ),  $V=1.23 \text{ V}$  ( $100.8 \text{ A/cm}^2$ ),  $V=1.42 \text{ V}$  ( $126.5 \text{ A/cm}^2$ )

### G595: reducing current density and plasmon frequency

Due to the mentioned experimental limitations the high current density domain (where instability can occur at high frequencies) was not accessed in previous experiments. A new set of structures, the sample G595 as a modified version of G494 was designed to bring the instability phenomenon within the range of experimental observation.: The dimensions of the parabolic and the pocket regions were increased to reduce the intersubband energies, thus ensuring that instability will occur at lower frequencies, possibly in the detection region of the InSb setup: half of the digital grown parabolic injector region which lies next to the active region was replaced by an 10 nm wide layer with constant Al-content ( $x=0.0462$ ) and the width of the active region was increased from 15.5 nm to 18.5 nm

Simultaneously the thickness of the entry barrier was increased from 1.2 nm to 1.8 nm and the RTD barriers were increased from 2.4 nm to 2.8 nm and thus the extraction rate of the RTF slightly reduced. This was aimed at reducing the current flow while keeping a high density of carriers inside the active region. This would allow instabilities to occur at lower current densities, thus avoiding heating.

Fig. 2.10 shows the conduction band and the energy levels of the eigenstates in the injector region and the active region of G595 at working bias. The second level of the prewell and the RTD-level are in resonance. The expected energy of the emission is around  $E=27\text{ meV}$ .

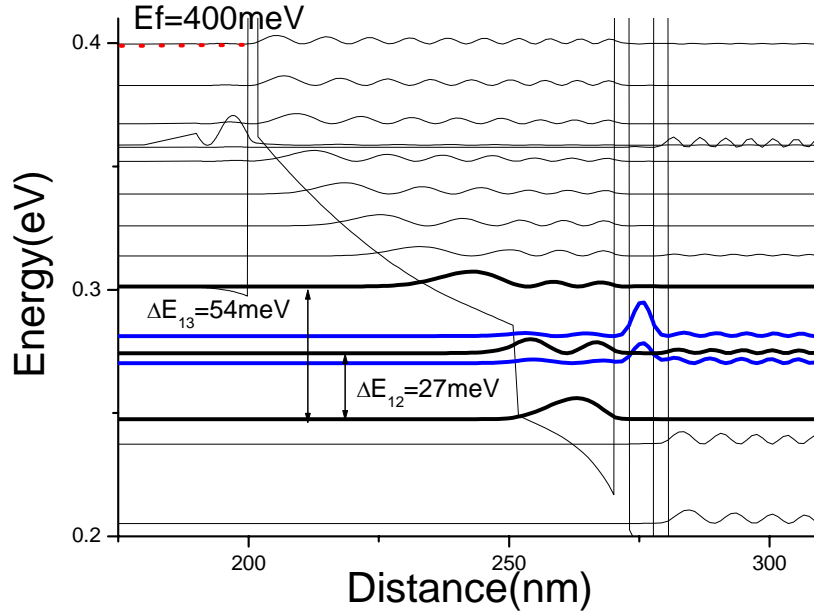


FIG. 2.10: Conduction band of the biased sample G595

Small mesas ( $10 \times 10\ \mu\text{m}$ ) were prepared to perform IV measurements at high current densities. They were processed in four steps to provide them with ohmic contacts. First the material over the back contact layer was removed by wet etching. Then ohmic GeAuNiAu contacts were evaporated and annealed at  $430^\circ\text{C}$  for three minutes. In a third step silicon nitride was deposited by using PECVD to isolate the sample and removed over the metallic contacts. Finally large CrAu-contacts were evaporated which are used to bond the sample. After processing the samples were cleaved, placed in a sample holder and bonded.

The measurements were performed at a Temperature of  $4.2\text{ K}$  in liquid helium. Fig. 2.11 shows the differential conductivity versus the bias voltage. At low bias voltages up to  $V=400\text{ mV}$  ( $\Delta V_I$ ) one finds low differential conductivity with pronounced oscillations. These oscillations indicate the quantization of the parabolic injection region.

At higher voltages ( $\Delta V_I$ ) the differential conductivity raises. This indicates the locking between the second level of the active region and the RTD level.



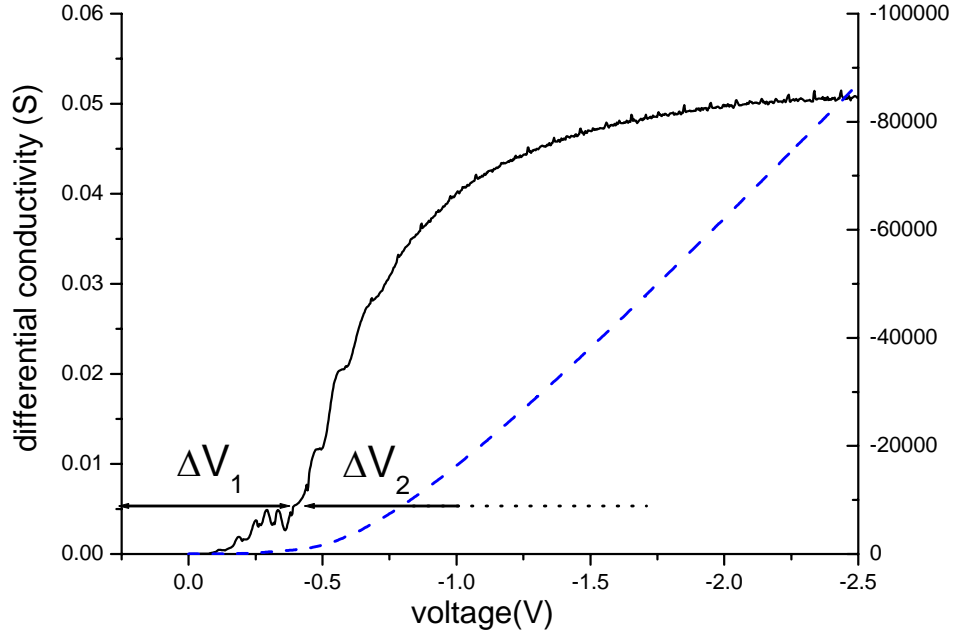


FIG. 2.11: Differential conductivity versus bias voltage of the sample G595 (periodic breakdown is from digitized measurements)

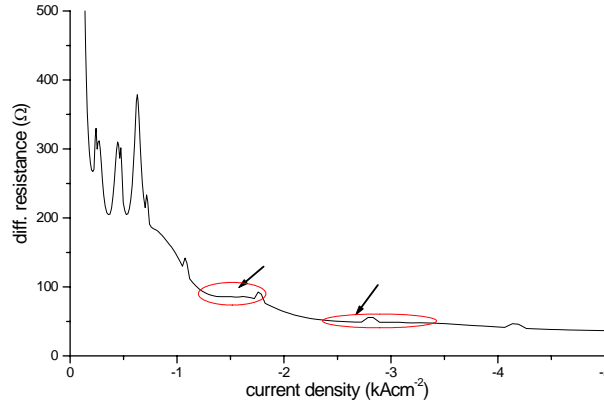


FIG. 2.12: Differential resistance versus current density of sample G595

Fig. 2.12 shows the differential resistance versus the current density. At low currents ( $< 1 \text{ kAcm}^{-2}$ ) one can see the quantization of the parabolic injection region. At higher currents two plateaus in the differential resistance are indicated by red ellipses (around  $1.5 \text{ kAcm}^{-2}$  and between  $2.5 \text{ kAcm}^{-2}$  and  $3.5 \text{ kAcm}^{-2}$ ). These current ranges could suggest plasma instability.

Fig. 2.13 shows current and differential conductivity versus positive bias voltage (reverse bias). There are the same well pronounced oscillations in the differential conductivity, which one can find for the former samples G428 and G494. These oscillations suggest biases where the RTD-level is resonant to the levels in the injection region. At  $V=2.1$  V the I-V shows a cut off. At this bias the second level of the pre well aligns with the parabolic driftregion.

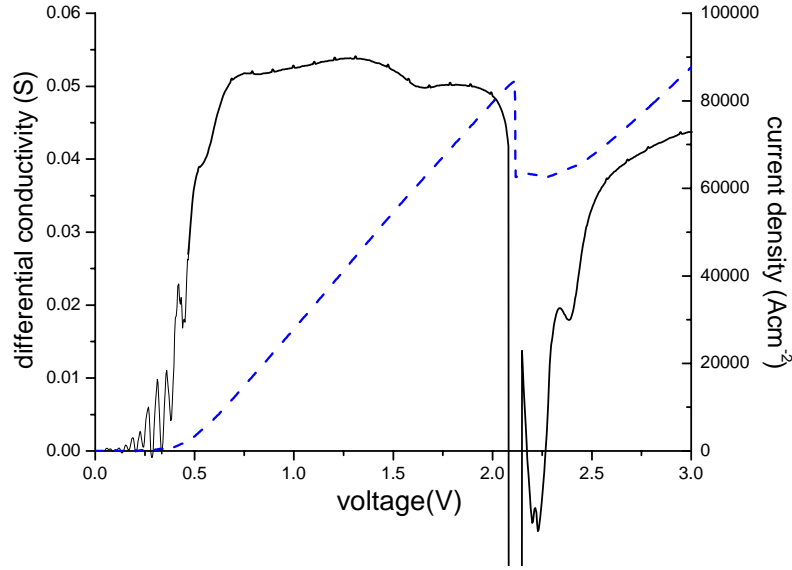


FIG. 2.13: Current and differential conductivity versus bias voltage of G595 (reverse bias)

Fig. 2.14 shows the emission obtained using both setups when the electrons enter the structure through the single barrier on the left side in Fig. 2.10. The three spectra in Fig. 2.14a are measured using the InSb-setup. The emission increases with the magnitude of the current. The total area of the emission strips is  $3.98 \times 10^{-3} \text{ cm}^2$ . There are two noteworthy features. At  $90 \text{ cm}^{-1}$  (about  $11 \text{ meV}$ , or  $2.75 \text{ THz}$ ) there is a strong peak, whose strength increases with current. A second feature at  $140 \text{ cm}^{-1}$  becomes clearly visible in the upper two curves. Based on the transport model and response calculations we interpret the peak around  $11 \text{ meV}$  to be due to the oscillation frequency of the electrons in the parabolic section of our active region (the Kohn resonance [25]). The second peak can be ascribed to an intersubband transition in the pocket region. The second feature has a half width of about  $1.25 \text{ meV}$ . This is much smaller than the line width of radiation from the earlier structure G301 [15]. That sample had internal doping in the active region, causing scattering and a resulting half width of  $2.5 \text{ meV}$  [15]. A reduction of line width by eliminating internal doping therefore has clearly been demonstrated by. The instrumental broadening contributes about  $0.5 \text{ meV}$  to the line width. Thus the collisional (including interface scattering) effects only amount to  $0.75 \text{ meV}$ , in G595. Achieving plasma instability growth of  $1 \text{ meV}$ , or more, should therefore suffice to have a positive net growth rate in such structures.

Fig. 2.14b shows the emission obtained from the fourier interferometer setup at much higher current densities ( $2200 \text{ Acm}^{-2}$ ). One can also find both peaks. While the maximum of the peak at lower energy is still at  $90 \text{ cm}^{-1}$ , the second peak is shifted to  $156 \text{ cm}^{-1}$  ( $19.5 \text{ meV}$ ). At these bias conditions the second peak is much broader than at lower current densities ( $4 \text{ meV}$ ). Therefore this emission is still caused by intersubband emission. It should be mentioned, that the energy of the intersubband emission is much lower than the expected  $27 \text{ meV}$ . This means, that the energy difference between the upper two levels of the three level system is too low to reach the needed conditions for the plasma instability.

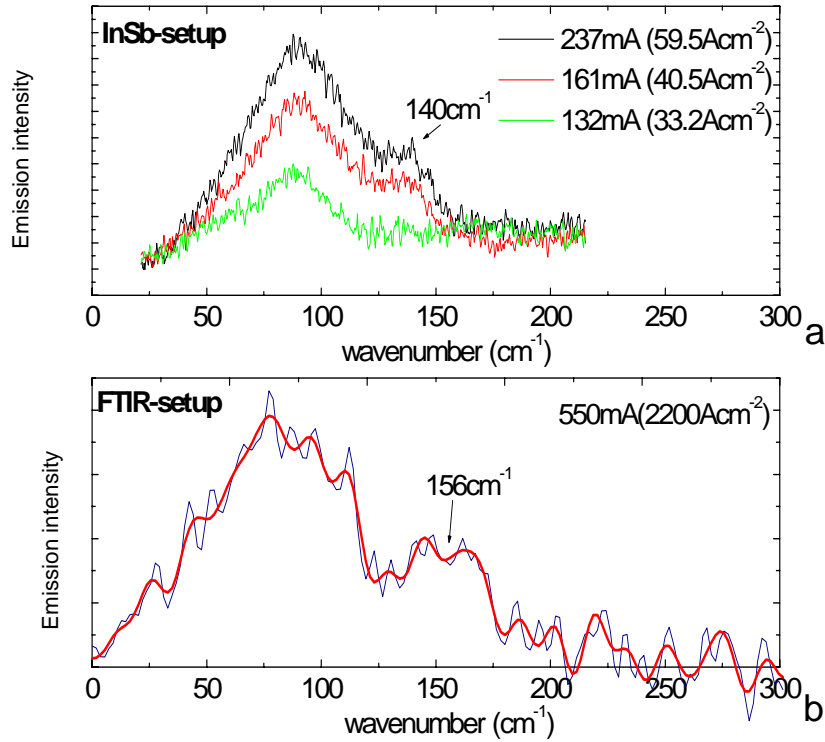


FIG. 2.14: Emission of G595 under normal operating bias direction

Fig. 2.15 shows the results for reverse bias (obtained from the InSb-setup), when the electrons enter the structure from the double barrier side. It should be noted that the RTD level is at a much higher energy, and the transport is not due to a ‘passage’ through a resonant level, but rather due to sequential tunneling. The four curves (from bottom to top) represent biases and currents (1.83 V, 0.148 A), (2.30 V, 0.245 A), (2.87 V, 0.359 A), and (3.94 V, 0.611 A), respectively. Again there is a broad peak at about  $90 \text{ cm}^{-1}$ , whose amplitude increases with the bias. This is the same frequency as for the forward bias (Fig. 11), and this strengthens the interpretation of this peak as due to the Kohn resonance, since it is controlled primarily by the curvature of the parabolic well- which remains rather fixed under various bias conditions, and not by the carrier density, which changes with the bias. The second feature at about  $140 \text{ cm}^{-1}$  again is due to intersubband transitions. It is less pronounced than that in Fig. 2.14a.

When the bias is increased further, the peak around  $90\text{ cm}^{-1}$  gets stronger, and the line width becomes narrower, indicating a nonthermal, collective origin to this feature. The bias cannot be increased too much further in this setup, without thermal damage to the sample.

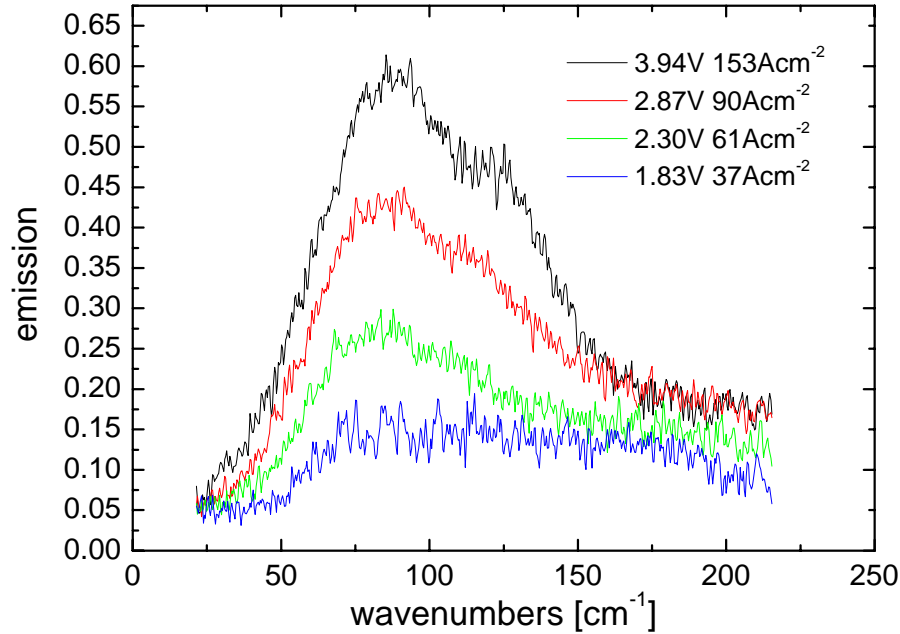


FIG. 2.15: Emission of G595 under reversed bias conditions.

### G565: low internal doping to allow more cascades

Previous experiments on cascaded structures (G534) showed, the it is not possible to apply a homogenous bias to all cascades if the internal doping is too high. Therefore to low doped samples were designed. The first design (Fig. 2.16), which was finally grown as sample number G565 consists of an improved variation of the previous samples with completely new designed bridging regions. The new “unit cell” was adapted to a structure were the distance between the levels  $E1$  and  $E3$  (in the GaAs pocket before the extractor) matches the optical phonon energy. At this particular bias ( $70\text{ meV}$  for one unit cell) the level  $E2$  aligns with the extractor level (ground level) of the resonant tunneling diode. Additionally this is the bias were flat-band condition occurs in the graded AlGaAs region in front of the GaAs pocket.

The doping was inserted in the graded parabolic region. 20 periods (cascades) of this particular structure have been grown into 2 highly doped GaAs layers to ensure good ohmic contacts to the structure. The growth was done on undoped GaAs material to reduce free carrier absorption in emission measurements as well as having the possibility to perform absorption studies at various frequencies. The first measurements we did on these samples are current voltage characteristics at low temperatures were we are able to demonstrate the working principle of the doping. The formation of low and high field

domains as in regular superlattice or quantum cascade structures shows that the external field can be applied to all 20 periods.

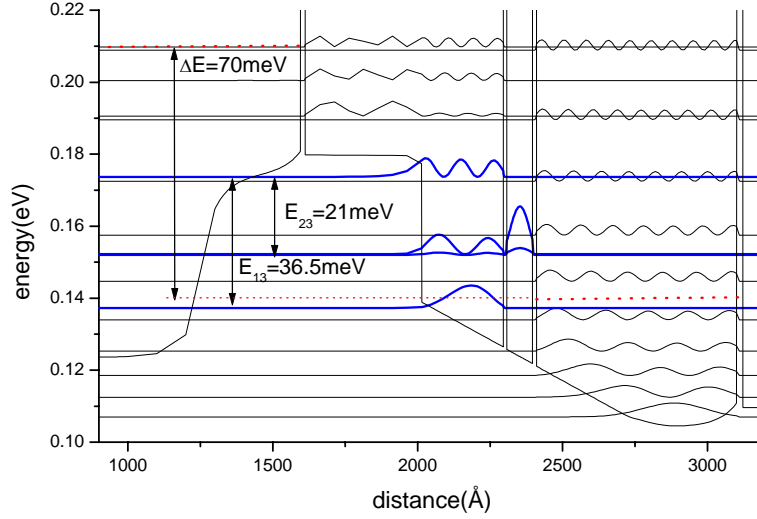


FIG. 2.16: Conduction band structure of G565 (working bias)

Fig. 2.17 shows the IV-curve of the reverse biased sample. One can see a domain formation region at low bias. In this bias range each cascade changes its bias behavior separately. Outside of this region each cascade is biased in the same way. This means that the low internal doping enables a coherent emission behavior of each cascade outside of the domain formation region.

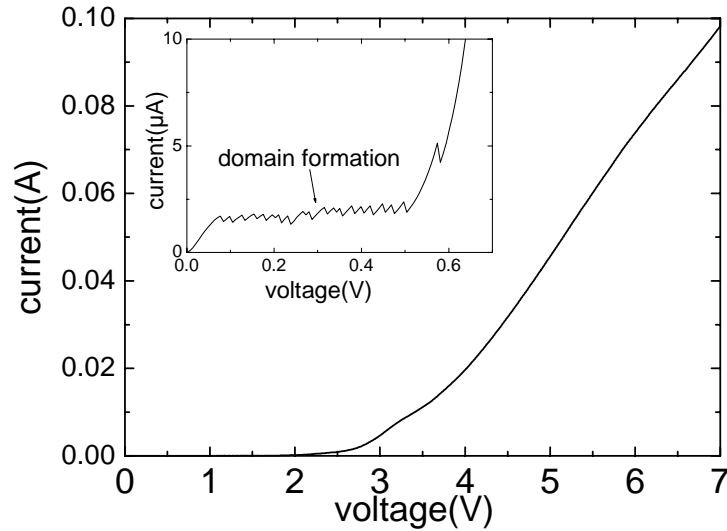


FIG. 2.17: IV of a  $100 \times 100 \mu\text{m}^2$  device of G565 positive bias

Fig. 2.18 shows the IV-curve in working direction. One finds also a domain formation region between bias voltages of 0.8 V and 1 V. At around 1V the current shows a strong rise. At this voltage the second level of the prewell links to the extraction level of the RTD. At a voltage of  $V=1.2$  V one finds another strong increase of the current, marked by  $V_{onset}$ . At biases higher than  $V_{onset}$  the current density reaches values which are needed to get measurable emission on large emission devices. The differential conductivity of the mesa device (Fig. 2.19) shows two peaks, marked by  $V_1$  and  $V_2$ . These peaks are good candidates for emission measurements. The first peak ( $V_1$ ) skews a domain formation region at bias voltages higher than 1.45 V. In this region the devices do not show a coherent behavior of all cascades.

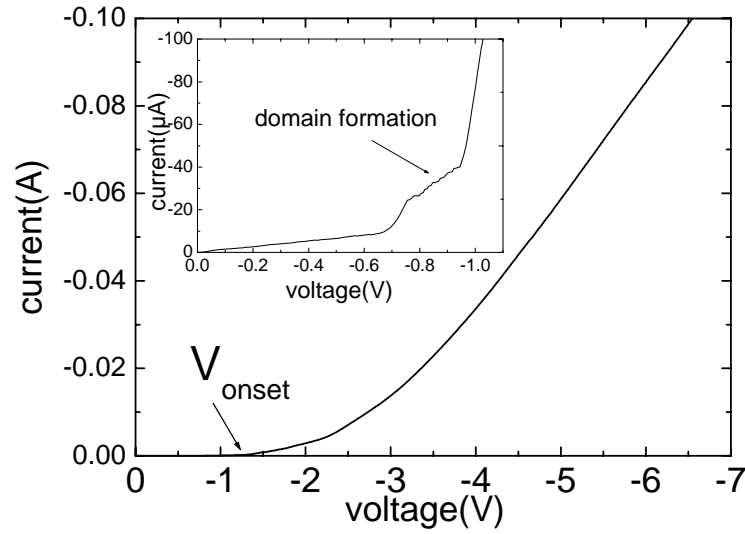


FIG. 2.18: IV of a  $100 \times 100 \mu\text{m}^2$  device of G565 negative bias

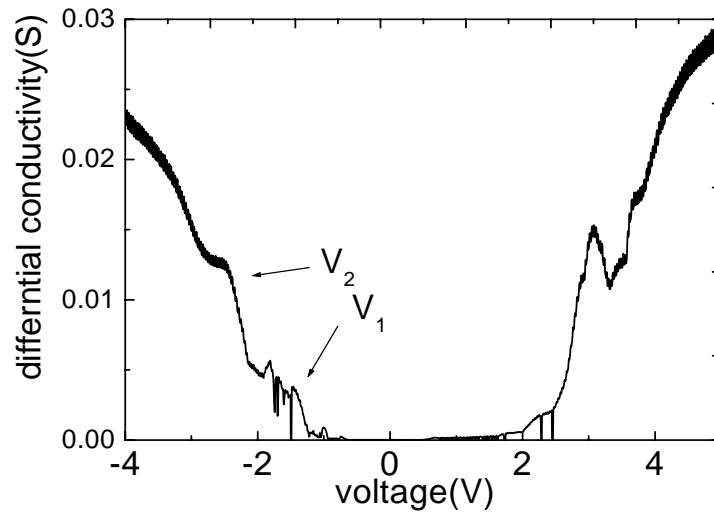


FIG. 2.19: Current density versus voltage of G565

Fig. 2.20 shows the current density of the mesa device in working direction obtained at  $T=10\text{ K}$  (dashed line) and  $T=40\text{ K}$  (solid line) compared with the current density of an emission sample (dotted line). The current density of the emission sample is even at low currents in good agreement to the current density of the hot mesa sample. This means that large emission devices cannot be cooled to  $4.2\text{ K}$ . This heating is caused by the high resistance of AlGaAs with low carrier concentration. Due to this heating it was not possible to get emission spectra.

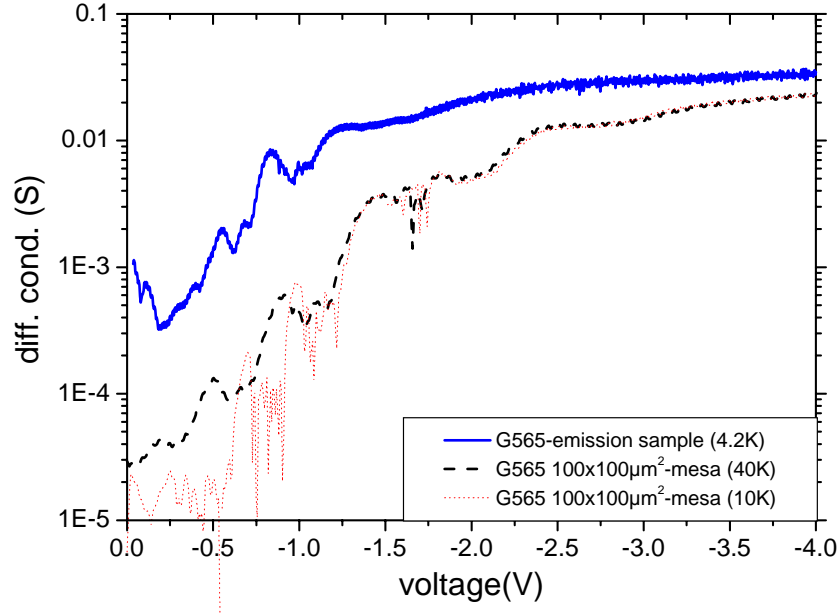


FIG. 2.20: Current density versus voltage of a  $100\times 100\text{ }\mu\text{m}$ -mesa of G565 at different temperatures and an emission sample at  $4.2\text{ K}$

## G564: new material system

The second low doped sample (G564) is based on a different material system.  $\text{In}_{0.05}\text{Ga}_{0.95}\text{As}$  layers are used as prewell and RTD-well instead of GaAs while the drift region before the active region consists of GaAs. Fig. 2.21 shows the unbiased “unit cell” Fig. 2.22 shows the “unit cell” with an applied bias of  $100\text{ mV}$ . One can see that the InGaAs prewell work as efficient electron trap. This ensures that the lowest level is filled even at high biases.

The AlGaAs barriers are substituted by AlAs barriers to prevent parasitical current due to hot electrons which cross the RTD at higher levels than the ground state. The width of the prewell was enlarged to  $285\text{ }\mu\text{m}$  to match an energy difference of  $36\text{ meV}$  (optical phonon energy) between the first and third level.

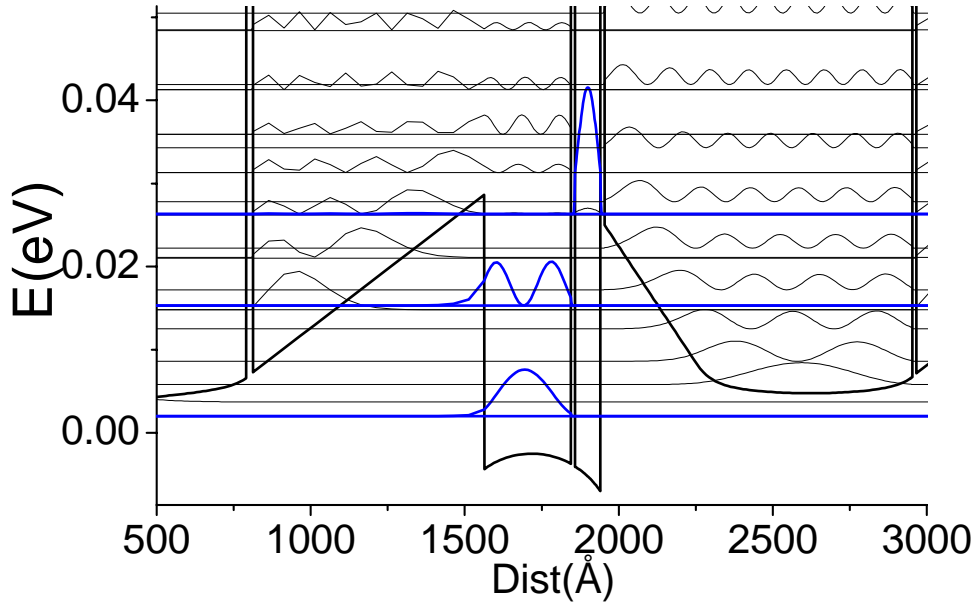


FIG. 2.21: Conduction band of the unbiased G564

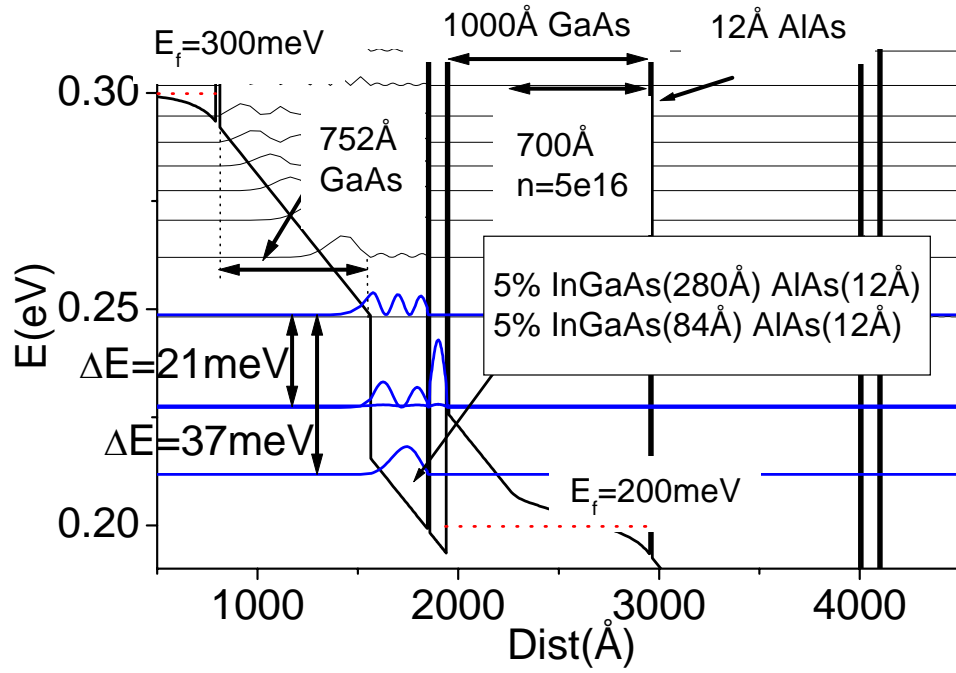


FIG. 2.22: Conduction band of G564 at working bias



This “unit cell” is cascaded 10 times. To prevent flooding most of the cascades with electrons like in G534 the internal doping was reduced to  $5 \cdot 10^{16} \text{ cm}^{-3}$

To resolve the current voltage behavior of this sample,  $100 \times 100 \mu\text{m}^2$ -mesas were prepared. In a first step the material over the contact layer below the structure was partly removed by reactive ion etching (RIE). The RIE was used to get perpendicular edges of the devices. After this GeAuNiAu-contacts were evaporated and annealed by heating the samples at  $430^\circ\text{C}$  for three minutes.

Fig. 2.23 shows the current density and the differential conductivity of G564 at  $T=4 \text{ K}$

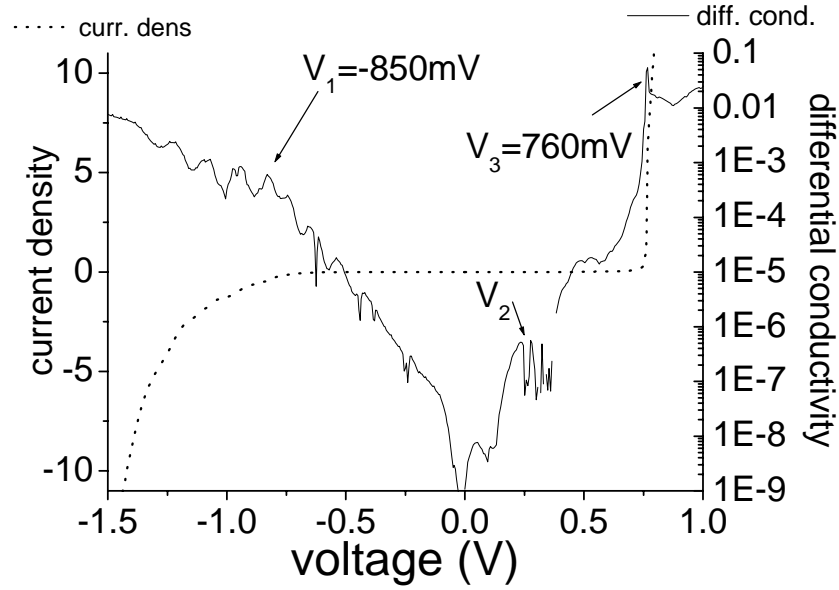


FIG. 2.23: Current density and differential conductivity at low currents

Three biases were marked as  $V_1$ ,  $V_2$  and  $V_3$ . At positive biases one can see a domain formation region between 300 mV and 400 mV ( $V_2$ ), which is known from quantum cascade structures. For each cascade the bias changes separately with raising voltage. Outside of this region the cascades are biased homogenously. At the positive bias  $V_3$  the second level of the prewell links to the continuum. This leads to a rise of the current and the differential conductivity of several magnitudes in a small bias range. At the bias  $V_1$  the second level gets aligned with the RTD-level. This also leads to a strong raise of the current.

The I-V measurements were performed by using the HP4155A which is limited to  $100 \text{ mA}$  ( $1000 \text{ A cm}^{-2}$  for  $100 \times 100 \mu\text{m}^2$ -mesas). Fig. 2.24 shows current density and the differential conductivity for the whole current range.

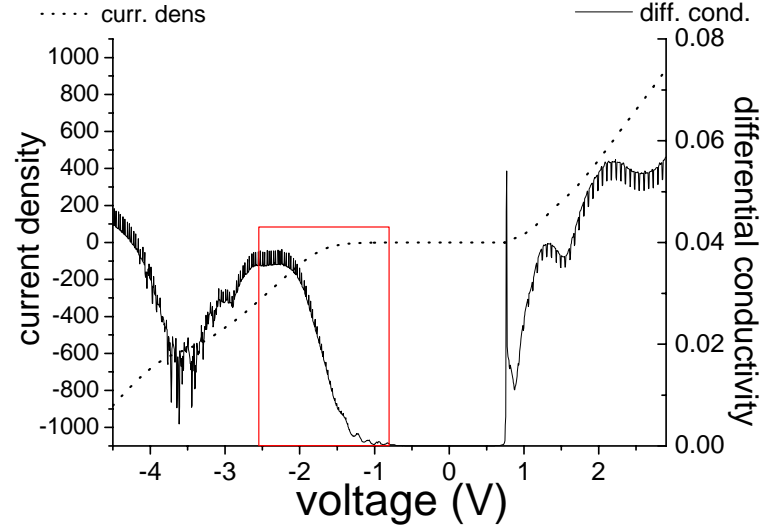


FIG. 2.24: Current density and differential conductivity of G564

The strong increase of current at a positive bias voltage of 760 mV can be clearly seen in the differential conductivity in Fig. 2.24. This feature is a sign for the homogeneous bias behavior of this structure. One can see also a domain formation region between  $V = -2.5$  V and  $V = -4$  V. In this bias range the lowest level in the prewell of each cascade gets aligned to the RTD-level separately. The bias range between 0.85 mV and 2.5 V which is marked by a rectangle is the region where emission may occur.

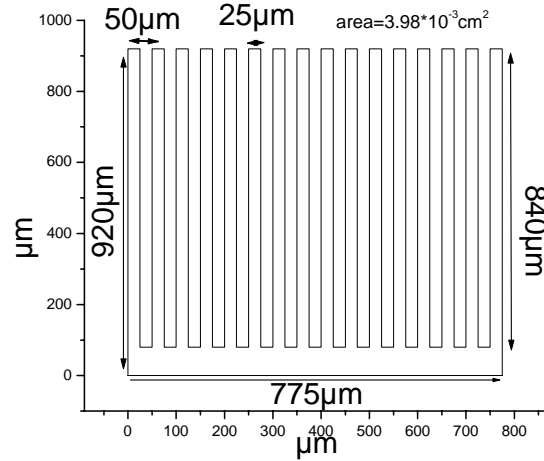


FIG. 2.25: Geometry of a 16 finger emission device

To perform emission measurements we used devices with a comb like shape (Fig. 2.25). These devices consist of  $840 \times 25 \mu\text{m}^2$ -fingers which are connected by an  $80 \mu\text{m}$  broad ridge

at one end. The length of this ridge depends on the number of fingers. The used device consists of 16 fingers. Therefore the ridge length is  $775 \mu\text{m}$ .

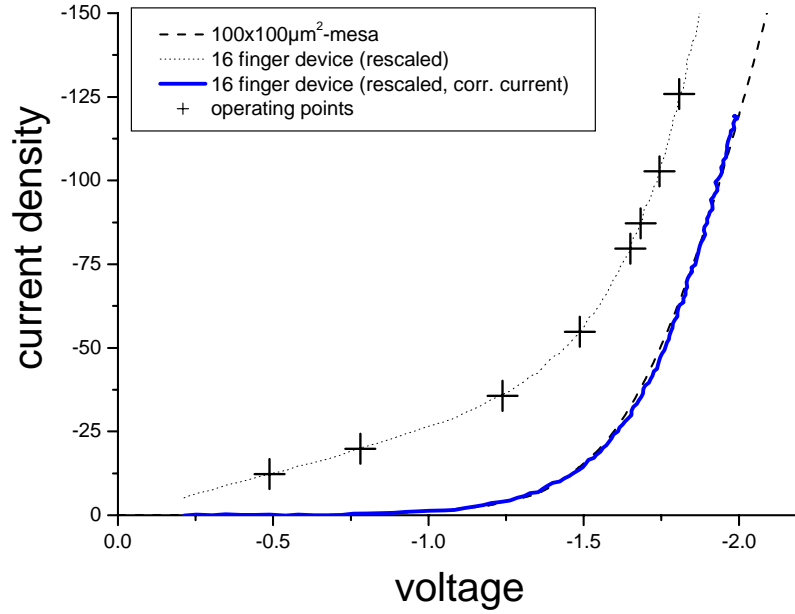


FIG. 2.26: Current voltage behavior of a 16 finger device of G564 and a mesa structure

Current voltage and step scan measurements were also performed at a 16 finger device. Fig. 2.26 shows the IV-curve of this device compared to the IV of a  $100 \times 100 \mu\text{m}^2$ -mesa. The dotted line in Fig. 2.26 shows the I-V of the 16 finger device versus the voltage taking a serial resistance of  $2.9 \Omega$  into account. Subtracting an internal parallel leakage current leads to the blue curve. The current voltage behavior of this device is in very good agreement with the mesa IV (dashed line) taking these to effects into account. The operating points for step scan measurements (Fig. 2.27) are marked with crosses.

All spectra show three sharp emission lines at  $118 \text{ cm}^{-2}$ ,  $124 \text{ cm}^{-2}$  and  $126 \text{ cm}^{-2}$ . Contrary to the following spectra the measurement at the lowest bias values does not show the intersubband emission. Between  $20 \text{ Acm}^{-2}$  and  $100 \text{ Acm}^{-2}$  one finds a broader peak at which is shifted between  $135 \text{ cm}^{-1}$  and  $145 \text{ cm}^{-1}$ . Instead of this emission one can see an absorption peak at  $129 \text{ cm}^{-2}$  at the lowest bias.

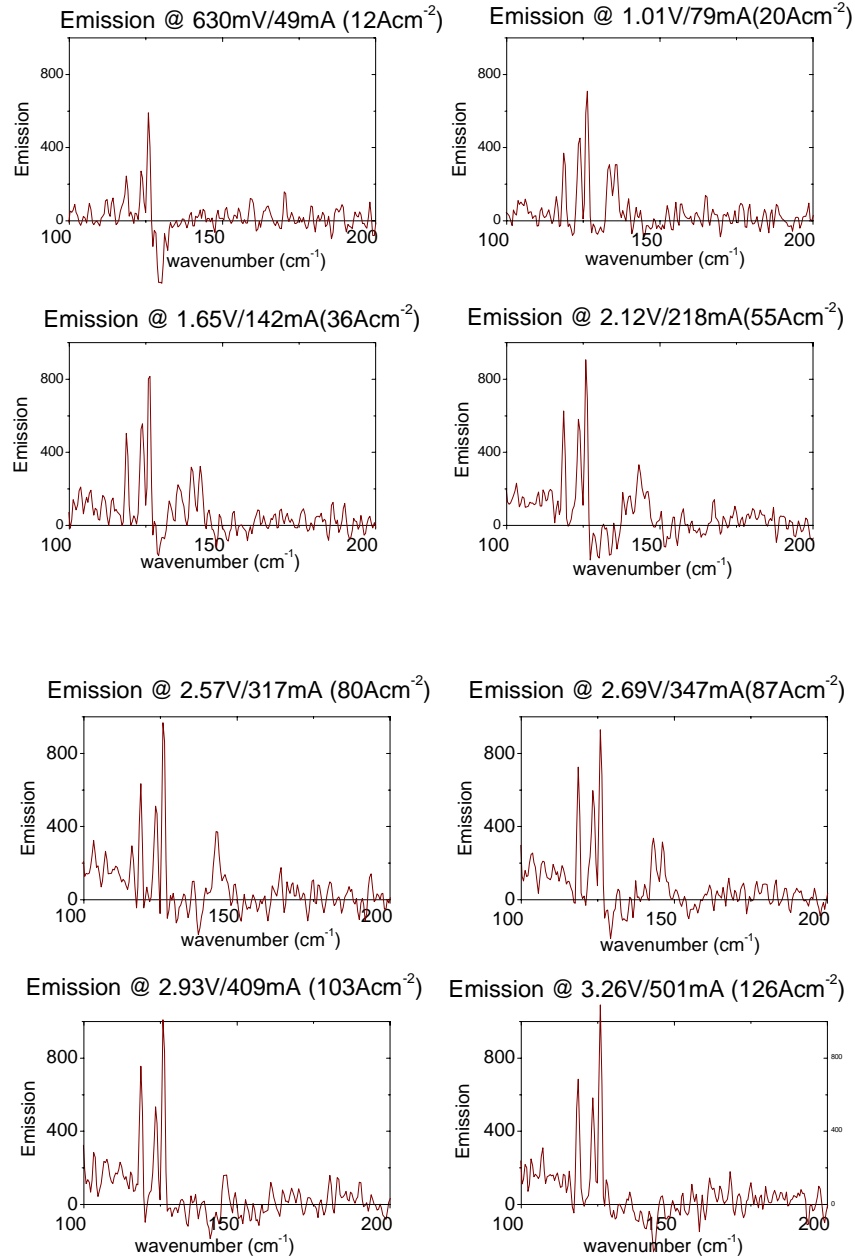


FIG. 2.27: Step scan measurements on a 16 finger device of G564

The position of this emission is plotted in Fig. 2.28 versus the current density. In the ranges between  $15 \text{ Acm}^{-2}$  and  $30 \text{ Acm}^{-2}$  and up to  $35 \text{ Acm}^{-2}$  one finds plateaus, where the shift of the peak position is smaller. In this ranges the peak width gets smaller. The emission reaches its maximum at the current density of  $30 \text{ Acm}^{-2}$ , where the peak width becomes minimal. The effect, which leads to a sharpening of the peak, can be explained as a weak growth rate. Due to the low intensity of the signal, compared to the noise level, these

results are in the order of the error. Due to this a 30 cascade structure of G564, which is described in the following chapter, was grown, to increase the emission.

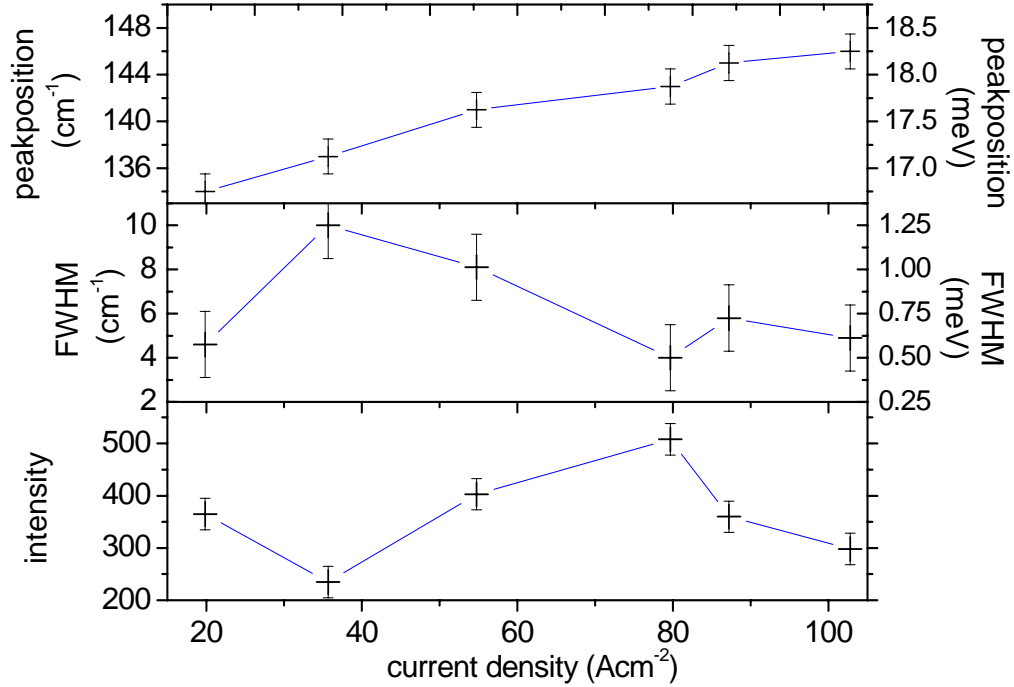


FIG. 2.28: Peak positions, width and intensity of the intersubband emission of the 16 finger device G564 versus the current density

The design of the investigated samples is asymmetric. The concept of these samples is to get inversion by extracting the electrons from the second level of the prewell through the RTD level, while electrons with higher energies cannot cross the RTD. Thus the emission shall only occur if we apply a negative bias between top and bottom contact. Fig. 2.29 shows the emission of the 16 finger device at three different reverse (positive) bias voltages. The broad emission does not occur. This means that the sample emits due to transmissions between the third and the second level of the prewell. Contrary to this emission the sharp lines at lower energies can be found also for the positive biased sample. Therefore these emission lines seem not to be caused by the plasma instabilities.

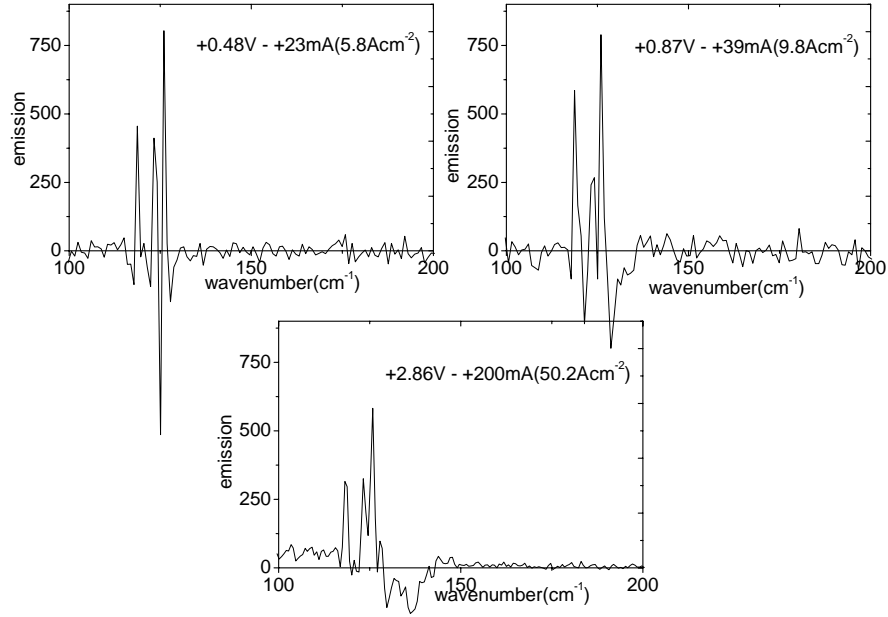


FIG. 2.29: Emission of an 8 finger device of G564 (reverse bias)

The emission of a 16 finger device of G564 was also measured by using the InSb-setup. The resulting spectrum at a current density of  $22 \text{ Acm}^{-2}$  (Fig. 2.30) shows a clearly resolved emission peak, which is placed on the trailing edge of the thermal background. The peak position is approximately at  $134 \text{ cm}^{-1}$ . This value is in good agreement to the expected position of the intersubband emission taking the resolution of the setup into account.

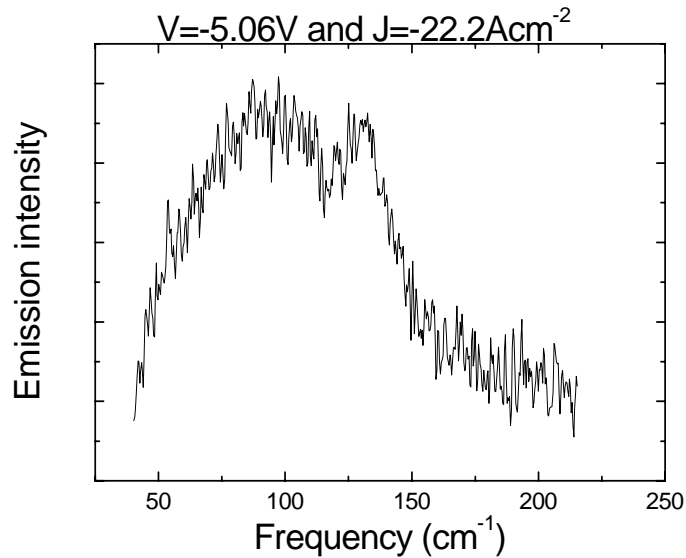
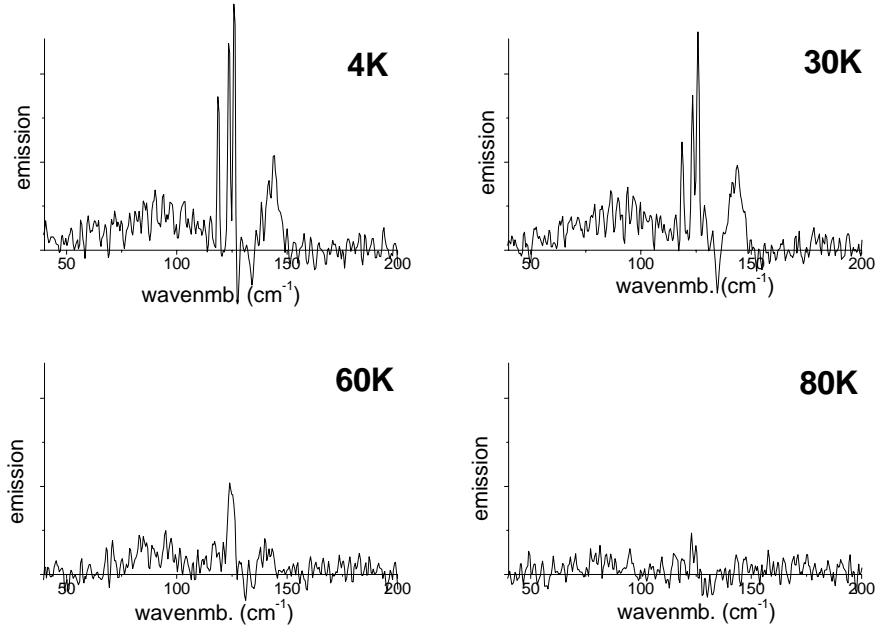


FIG. 2.30: InSb measurement on a 16 finger device of g564

Another parameter, which give information about plasmon instability is the temperature dependence of the emission, because the instability is a many body effect and therefore it less sensitive to high temperatures than intersubband emission. Fig. 2.31 shows the emission of G564 at different temperatures. One can see that the emission of G564 decreases at higher temperatures and vanishes at around 80 K. Therefore the intersubband plasmon effect is to weak to reach a remarkable insensitivity to high temperatures.



*FIG. 2.31: Emission of G564 at different temperatures*

## **W2: increasing emission due to more cascades**

To increase the emission of this structure and to learn more about the origin of the sharp lines another sample called W2 with the same “unit cell” repeated 30 times was grown and prepared for emission measurements. The sample was grown at the weitzmann institute. Thus we can also test the reproducibility of unit cell design, taking the characteristics of the growth process into account.

In contrary to the mesa devices, which showed no reproducible behavior the emission structures showed useable IV characteristics for performing emission measurements. The used structures are 16 finger devices (see Fig. 2.25) and 2 finger devices shown in Fig. 2.32.

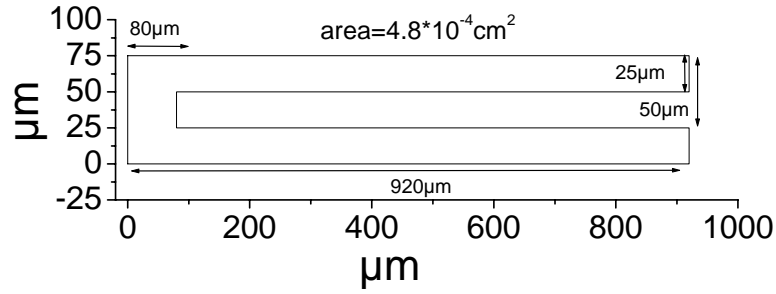


FIG. 2.32: Geometry of a two finger device

The small area of the two finger device allows measurements at current densities in the order of several  $100 \text{ Acm}^{-2}$ , while the current is still in a suitable range.

Fig. 2.33 shows the current density of the 16 finger device plotted versus the bias voltage. Step scan measurements were performed  $50 \text{ mA}$  and  $350 \text{ mA}$ . The applied biases are limited by heating due to higher currents. The crosses in Fig. 2.33 mark the bias values of the step scan measurements.

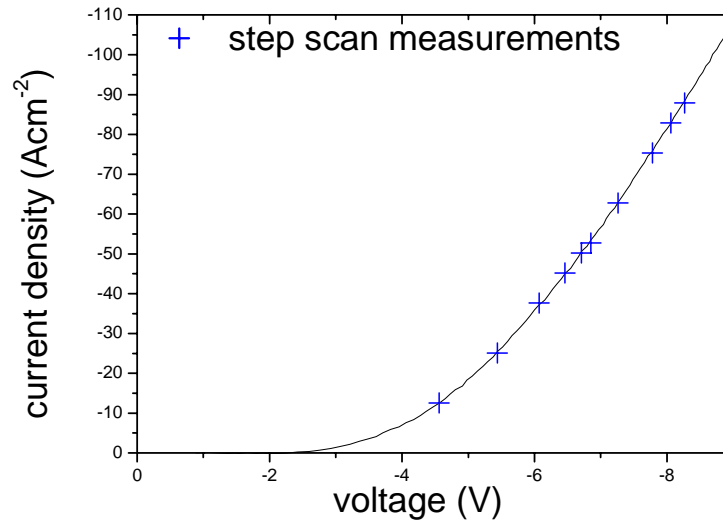


FIG. 2.33: Current voltage behavior of a 16 finger device of W2

The step scan measurements are shown in Figures 2.34-36. In Fig. 2.36 one can see also two measurements in inverse bias direction (positive bias). One can see a broad (the full width at half maximum (FWHM) is around  $55 \text{ cm}^{-1}$ ) peak at around  $90 \text{ cm}^{-1}$  and another peak, which is shifted between  $150 \text{ cm}^{-1}$  and  $160 \text{ cm}^{-1}$  (FWHM:  $20 \text{ cm}^{-1}$ ), in each spectrum at negative operating points. Both peaks reach a maximum at  $200 \text{ mA}$ . At  $200 \text{ mA}$  a sharp peak (FWHM:  $8 \text{ cm}^{-1}$ ) occurs at  $125 \text{ cm}^{-1}$ , which gets stronger up to the highest applied bias. At higher biases these features sit on the background of low energy peak. In contrary to previous measurements the spectra of the reverse biased sample do not show the same behavior.



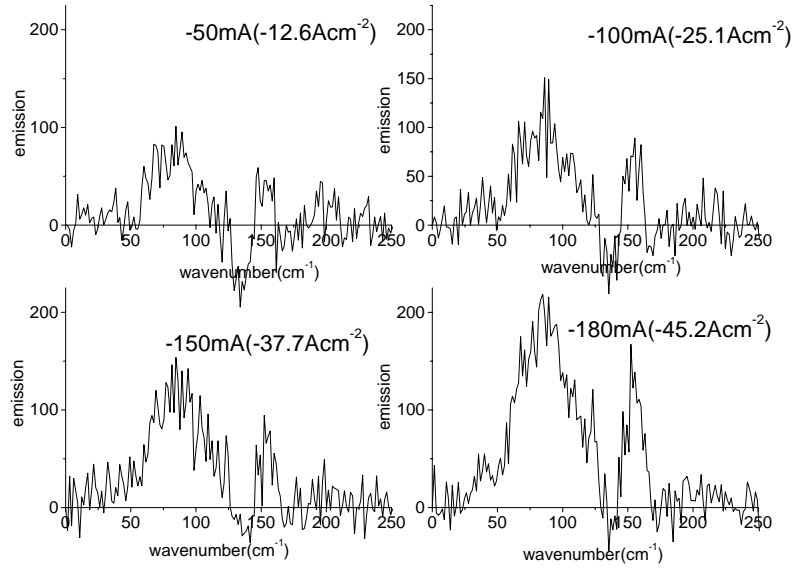


FIG. 2.34: Step scan measurements on a 16 finger device of W2 (low biases)

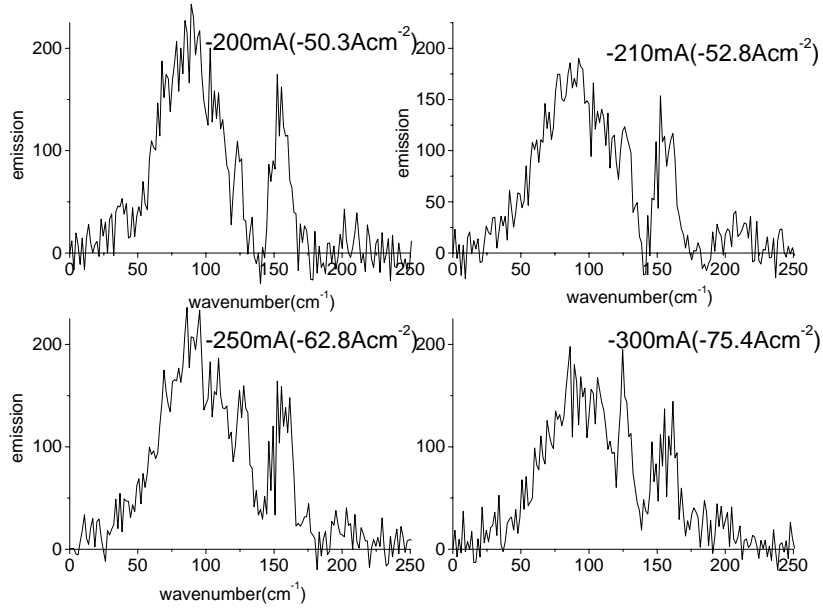


FIG. 2.35: Step scan measurements on a 16 finger device of W2 (mid biases)

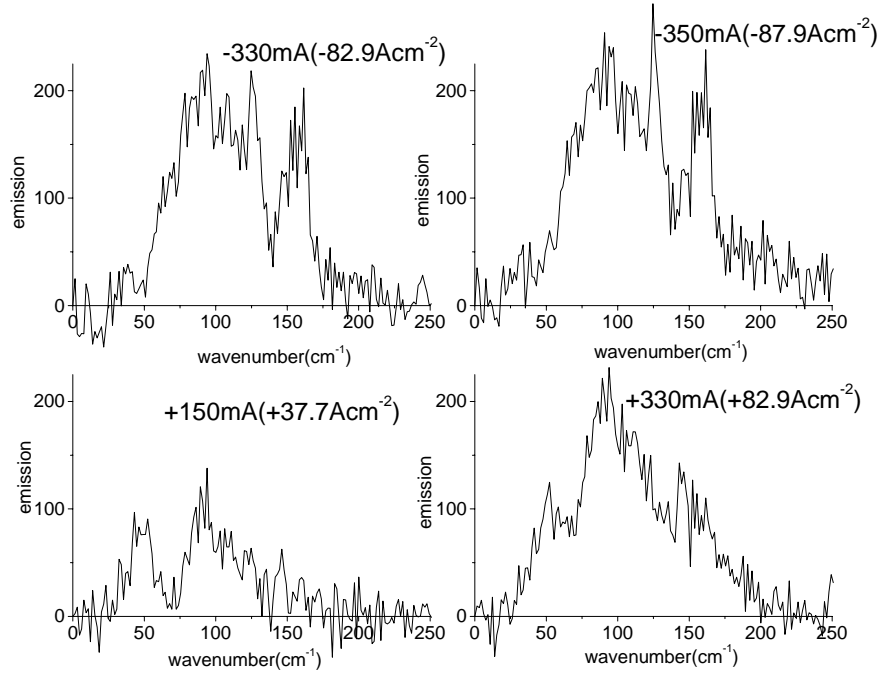


FIG. 2.36: Step scan measurements on a 16 finger device of W2 (high and inverse biases)

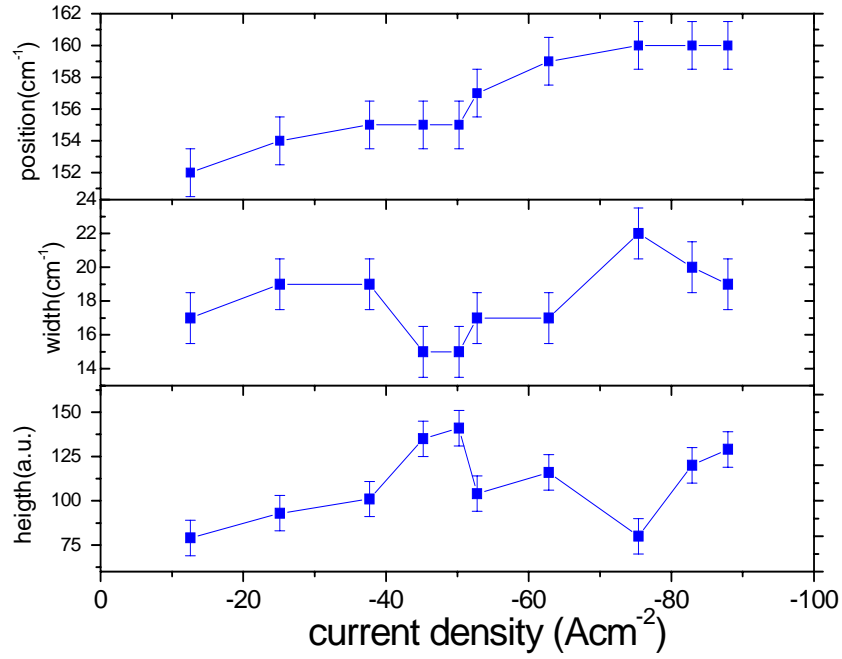


FIG. 2.37: Peak positions, full width at half maximum and peak height of the high energy emission peak of the structure W2

The peak position and the width of the peak at energies around  $160\text{ cm}^{-1}$  is shown in Fig. 2.37. One can see two ranges, where the peak position stays almost constant. At biases between  $4.5\text{ V}$  and  $6.8\text{ V}$  the position is at  $155\text{ cm}^{-1}$  and at biases higher than  $7.8\text{ V}$  one finds the emission peak at  $161\text{ cm}^{-1}$ . While the peak position stays constant the width of the peaks decreases. The peaks become sharper. While the peak position increases with increasing bias, the width of the peaks increases also. The intensity of the peak shows the inverse behavior of the FWHM. The intensity shows a strong increase when the lines get sharper. This can be explained with a weak ( $0.5\text{ meV}$ ) plasma instability growth [66].

The peak position is found at higher energies than for G564. This can be caused the common deviations of growth parameters between two samples and of course between two different MBE`s.

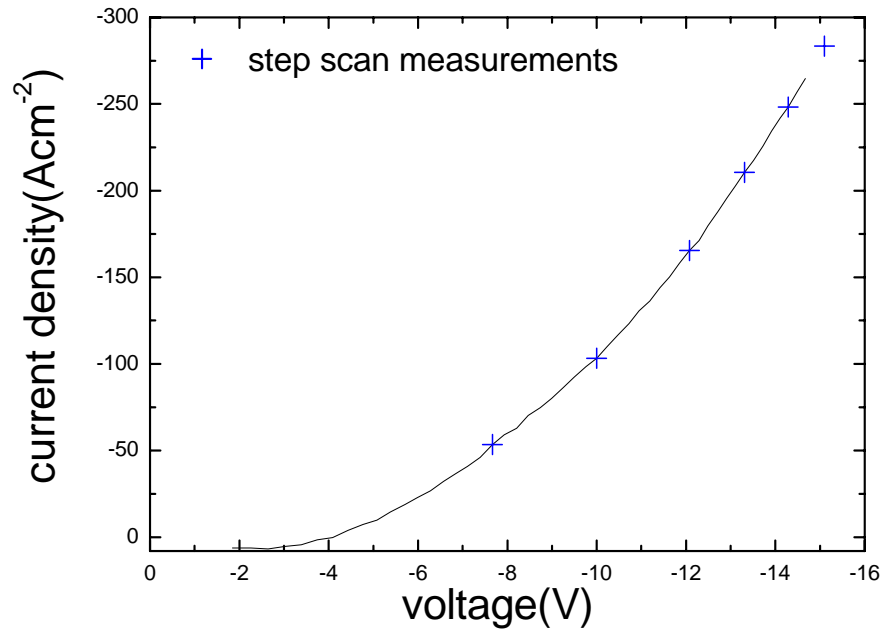


FIG. 2.38: Current density versus voltage of a 2 finger device of W2 at 5K

To measure spectra at higher current densities two finger devices were used for step scan measurements. Fig. 2.38 shows the current density of the 2 finger device plotted versus the bias voltage. Step scan measurements were performed  $25\text{ mA}$  and  $200\text{ mA}$ . The crosses in Fig. 2.38 mark the bias values of the step scan measurements which are plotted in Fig. 2.39.

One can see a strong and sharp ( $2.5\text{ cm}^{-1}$ ) emission line at  $127\text{ cm}^{-1}$  and broader a absorption peak at  $135\text{ cm}^{-1}$ . The position of these peaks fits to the position of the two sharp lines in the FTIR-spectra of G564 and the sharp line in the 16 finger device measurements of W2. Also the absorption peak can be found in several of the spectra of G564. The

position of the sharp line does not change at different biases. The intensity of this line reaches its maximum at between  $100 \text{ Acm}^{-2}$  and  $170 \text{ Acm}^{-2}$ . At higher biases it decreases until it disappears at current densities higher than  $400 \text{ Acm}^{-2}$ . This value is in good agreement to the cut off of the bias range for G564 (see Fig. 2.24), which contains the same “unit cell” like w2. The emission spectrum at  $211 \text{ Acm}^{-2}$  shows a broad thermal emission which has vanished at  $275 \text{ cm}^{-1}$  due to LO-phonon scattering. The last graph in Fig. 2.39 shows the emission of the reverse biased sample at current densities of  $87 \text{ Acm}^{-2}$  and  $108 \text{ Acm}^{-2}$ . One finds also a sharp emission peak followed by strong absorption. The origin of this behavior is still not clear.

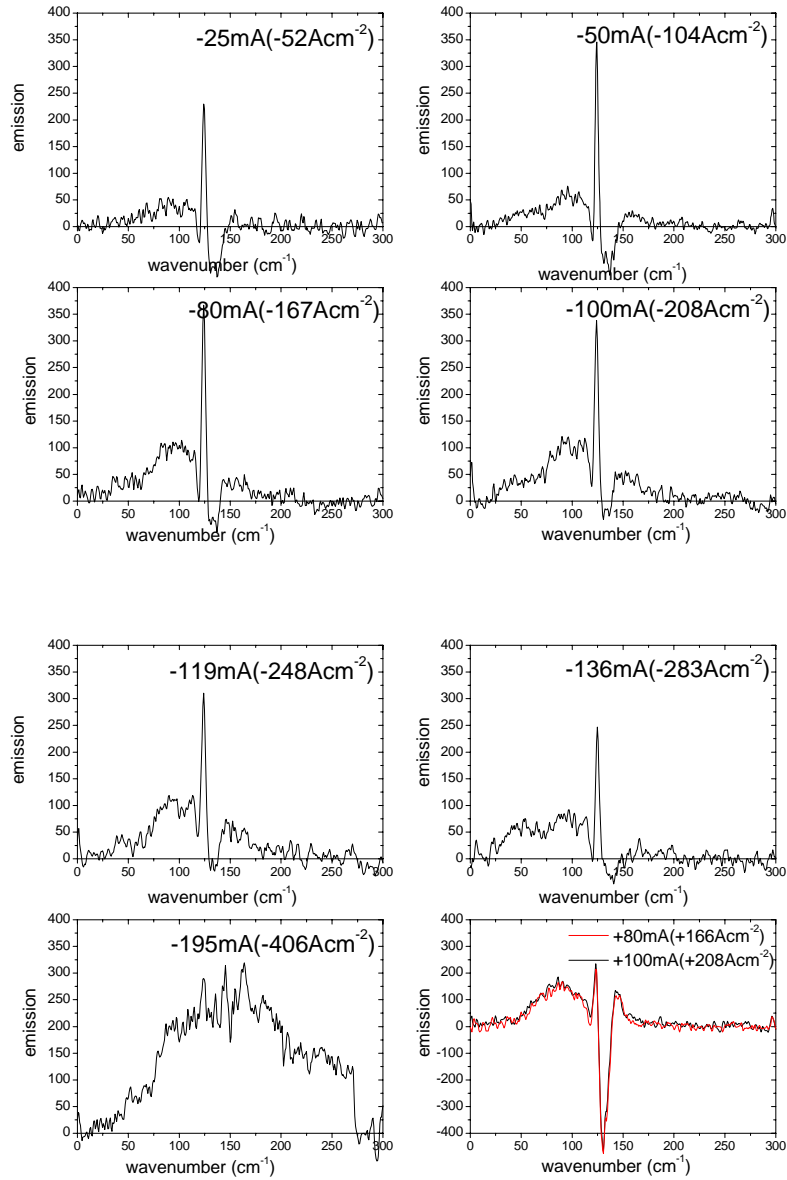


FIG. 2.39: Step scan measurements on a 2 finger device of sample W2

## G672: increasing current densities

To learn more about the origin of the emission of G564 and W2 another sample based on the same material system was grown. Fig. 2.40 shows the conduction band of the new sample (G672) This sample consists of 20 cascades of a G564 “unit cell” with a smaller prewell (26.8 nm instead of 28.5 nm). To reduce the resistance of the sample the internal doping was increased from  $5 \times 10^{16} \text{ cm}^{-3}$  to  $8 \times 10^{16} \text{ cm}^{-3}$ . Fig. 2.41 shows the current density versus the voltage of a  $100 \times 100 \mu\text{m}$ -mesa of G672, compared to the current density of G564 plotted versus 2 times the bias voltage to take the different number of cascades into account. One can see a good agreement of current voltage behavior at low currents. In contrary to G564 the new sample does not show the cut off behavior of G564. This means, that this sample is still working at current densities higher than  $1000 \text{ Acm}^{-2}$

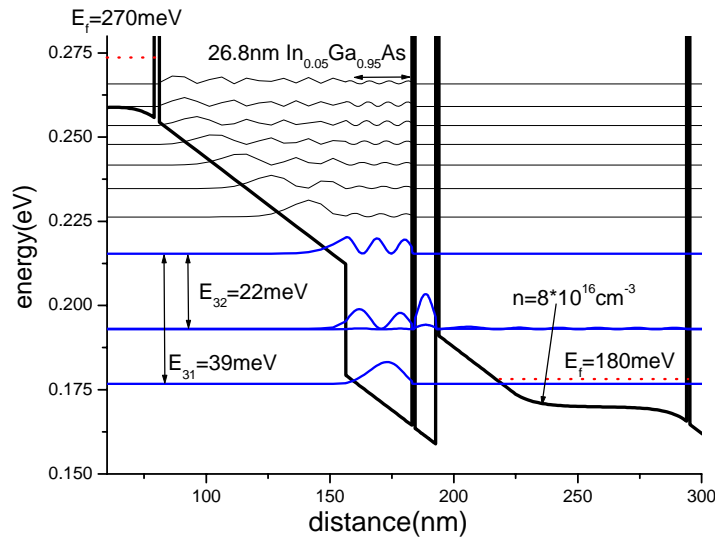


FIG. 2.40: Conduction band of G672

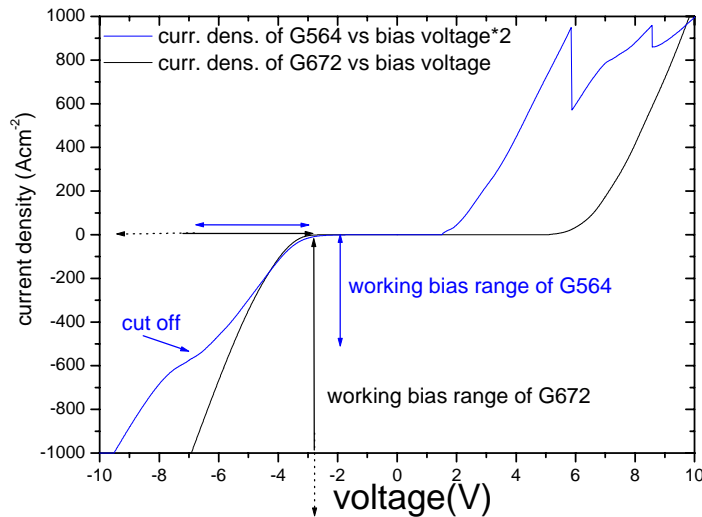


FIG. 2.41: Current density versus voltage of G672 compared to G564

The first emission measurements were obtained from a 16 finger device using the FTIR-setup. The current voltage behavior and the total emission is plotted in Fig. 2.42. Up to 6 V no significant current is measured and therefore the sample does not show emission. At higher biases the device opens. The total emission rises with increasing current density and saturates at 12 V, which means a current density of  $22 \text{ Acm}^{-2}$ . The crosses in Fig. 2.46 indicate the operating points of the obtained step scan measurements (Fig. 2.47).

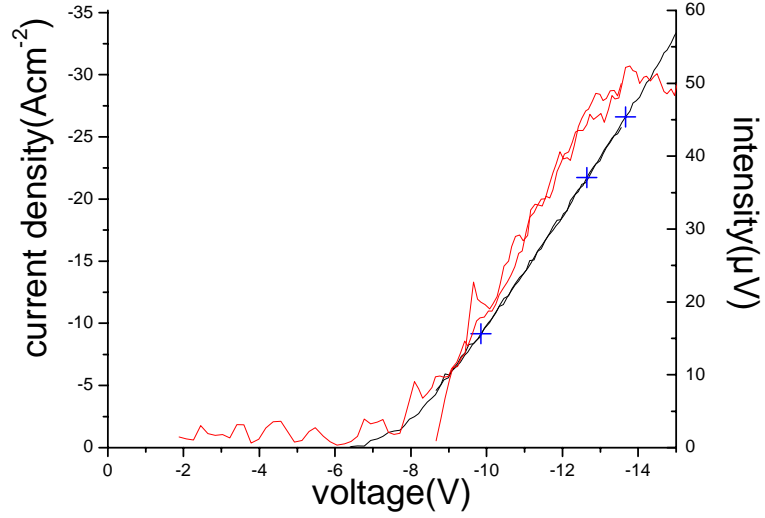


Fig .2.42: Current density and total emission versus sample voltage of a 16 finger device of G672

The spectra shown in Fig. 2.43 are obtained at current densities (between  $9 \text{ Acm}^{-2}$  and  $50 \text{ Acm}^{-2}$ ) from a 16 finger emission device. One finds in all spectra two broad peaks.

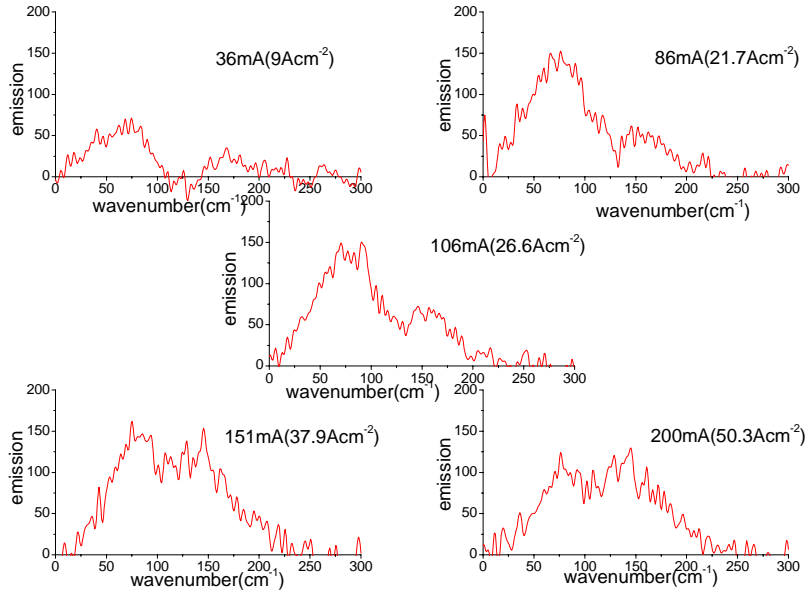


FIG. 2.43: Emission spectra of a 16 finger device of G672

The first peak can be found around  $80\text{ cm}^{-1}$  (FWHM  $65\text{ cm}^{-1}$ ) and the second one around  $165\text{ cm}^{-1}$  (FWHM  $50\text{ cm}^{-1}$ ).

The first peak can be identified as intersubband emission in the drift region. It is shifted to lower energies compared to W2 measurements, because the higher internal doping leads to a higher charging of the prewell, and therefore to a lower bias between injector barrier and prewell. The second peak can be explained as intersubband emission due to scattering between the third and second prewell level. This peak is shifted to higher energies compared to the results from W2 (see Figures 2.34-37), due to the lower width of the prewell. Fig. 2.44 shows the emission of 2 finger device (see Fig 2.36). One can see that the low energy peak gets much smaller compared to the intersubband emission. Due to the broad peak we still could not observe a remarkable bias dependend behavior. G672 was the first sample, which was grown, after the MBE was opened. After opening the MBE, it last several month to get samples of optimal quality. The broad peak can be caused by a lower quality of the sample, due to this.

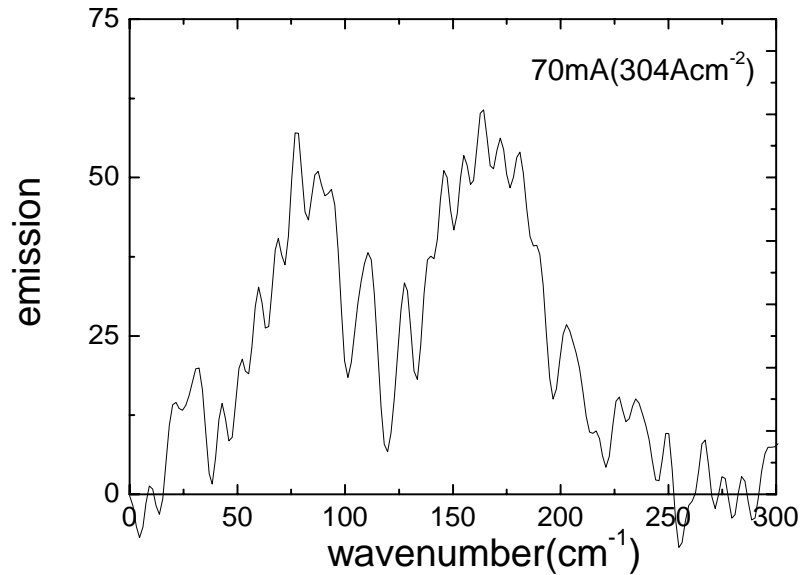


FIG. 2.44: Emission spectra of a 2 finger device of G672

## References

- [1] see e.g. *Terahertz Sources and Systems*, R.E. Miles et al. (eds), Kluwer Academic publishers, Netherlands, (2001)
- [2] R. Köhler, A. Tredicucci, F. Beltram, H. E. Beere, E. H. Linfield, A. G. Davies, D. A. Ritchie, R. C. Iotti, and F. Rossi, *Nature* (London) **417**, 156 (2002)
- [3] G. Scalari, L. Ajili, J. Faist, H. Beere, E. Linfield, D. Ritchie, and G. Davies, *Appl. Phys. Lett.* **82**, 3165 (2003)
- [4] B. S. Williams, S. Kumar, H. Callebaut, Q. Hu, and S. Reno, *Appl. Phys. Lett.* **83**, 5142 (2003)
- [5] P. Bakshi and K. Kempa, *Superlatt. Microstruct.* **17**, 363 (1995).
- [6] P. Bakshi and K. Kempa "Mathematical Signatures of Plasma Instabilities in Low-Dimensional Solid State Systems" in *Condensed Matter Theories* J. Clark and P. Panat (eds.), NOVA Science Publishers, Vol. 2, 399 (1997)
- [7] F. F. Chen, *Introduction to Plasma Physics and Controlled Fusion*, Plenum Press, NY (1984).
- [8] S. Ichimaru, *Basic Principles of Plasma Physics*, Benjamin/Cummings, Reading Mass. (1973).
- [9] A. B. Mikhailovskii, *Theory of Plasma Instabilities*, Consultant Bureau, NY, (1974).
- [10] N. Krall and A. Trivelpiece, *Principles of Plasma Physics*, McGraw-Hill, NY (1973)
- [11] E. Gornik and D. C. Tsui, *Phys. Rev. Lett.* **37**, 1425 (1976).
- [12] K. D. Maranowski, A. C. Gossard, K. Unterrainer, and E. Gornik, *Appl. Phys. Lett.* **69**, 3522 (1996).
- [13] J. Ulrich, R. Zobl, K. Unterrainer, G. Strasser, E. Gornik, K. D. Maranowski, and A. C. Gossard, *Appl. Phys. Lett.* **74**, 3158 (1999).
- [14] R. Kersting, K. Unterrainer, G. Strasser, H. F. Kauffmann, and E. Gornik, *Phys. Rev. Lett.* **79**, 3038 (1997)
- [15] P. Bakshi; K. Kempa, A. Scorupsky, C. G. Du, G. Feng, R. Zobl, G. Strasser, C. Rauch, Ch. Pacher, K. Unterrainer, and E. Gornik, *Appl. Phys. Lett.* **75**, 1685 (1999).
- [16] O. Madelung, *Introduction to Solid-State Theory*, Springer series in solid-state sciences, Vol.2,(1978)
- [17] R.D. Mattuck, "A Guide to Feynman Diagrams in the Many-Body Problem", Dover Publications, New York 1976
- [18] S. J. Allen, Jr, D. C. Tsui, and B. Vinter, *Solid State Commun.* **20**, 425 (1976).
- [19] T. Ando, A. B. Fowler, and F. Stern, *Rev. Mod. Phys.* **54**, 437 (1982)
- [20] M. Zaluzny, *J. Appl. Phys.* **74**, 4716 (1993)
- [21] K. Craig, B. Galdrikian, J. N. Heyman, A. G. Markelz, J. B. Williams, M. S. Sherwin, K. Campman, P. F. Hopkins, and A. C. Gossard, *Phys. Rev. Lett.* **76**, 2382 (1996).
- [22] G. Feng, PhD Thesis, Boston College, Boston USA 2002



- [23] A. Wixforth, M. Kaloudis, C. Rocke, K. Ennslin, M. Sundaram, J. H. English, and A. C. Gossard, *Semicond. Sci. Technol.* **9**, 215 (1994)
- [24] Z. Ando, *Z. Phys. B* **24**, 33 (1976)
- [25] W. Kohn, *Phys. Rev.* **123**, 1242 (1961)
- [26] R. Zobl, PHD Thesis, Vienna University of Technology, Vienna, Austria 2002
- [27] R Zobl, K. Unterrainer, G. Strasser, E. Gornik, *Semicond. Sci. Technol.* **15**, 315 (2000)
- [28] J. Ulrich, PHD Thesis, Vienna University of Technology, Vienna, Austria 2002
- [29] D. Pines, *Elementary Excitations in Solids*, Perseus Books, Reading, Mass. (1999).
- [30] S. Das Sarma, *Phys. Rev. B* **29**, 2334 (1984).
- [31] F. Stern, *Phys. Rev. Lett.* **18**, 546 (1967).
- [32] F. Forstmann, R. R. Gerhardts, *Metal Optics Near the Plasma Frequency*, Springer tracts in modern physics., Vol.109, (1986).
- [33] M. Dyakonov and M. Shur, *Phys. Rev. Lett.* **71**, 2465 (1993)
- [34] S. A. Mikhailov, *Phys. Rev. B* **54**, 10335 (1996)
- [35] R. Zobl, M. Fuchshuber, G. Strasser, K. Unterrainer, E. Gornik, K. D. Maranowski, and A. C. Gossard, *Sixth International conference on THz Electronics Proceedings*, P. Harrison editor, IEEE (1998)
- [36] S. K. Yip, *Phys. Rev. B* **43**, 1707 (1991).
- [37] K. Hirakawa, M. Grayson, D. C. Tsui, and C. Kurdak, *Phys. Rev. B* **47**, R16651 (1993).
- [38] K. Hirakawa, K. Yamanaka, M. Grayson, and D. C. Tsui, *Appl. Phys. Lett.* **67**, 2326 (1995).
- [39] P. Hyldgaard, J. W. Wilkins, *Phys. Rev. B* **53**, 6889 (1996)
- [40] J. H. Smet, C. G. Fonstad, and Q. Hu, *J. Appl. Phys.* **79**, 9305 (1996)
- [41] S.-C. Lee, I. Galbraith, and C. R. Pidgeon, *Phys. Rev. B* **52**, 1874 (1995)
- [42] R. C. Iotti, F. Rossi, *Phys. Rev B* **87**, 146603 (2001)
- [43] J. Ulrich, R.Zobl, K. Unterrainer, G. Strasser, and E. Gornik, *Appl. Phys. Lett.* **76** 19 (2000)
- [44] J. Ulrich, R. Zobl, N. Finger, K. Unterrainer, G. Strasser, and E. Gornik, *Physica B*, **272**, 216 (1999)
- [45] A. Katalsky, A. L. Efros, *J. Appl. Phys.* **69**, 841 (1991); A. Blank, S. Feng, *J. Appl. Phys.* **74**, 4795 (1993)
- [46] E. H. Putley, *Phys. Status Solidi* **6**, 571 (1964)
- [47] M. Rochat, J. Faist, M. Beck, U. Oesterle, M. Ilegems, *Appl. Phys. Lett.* **73**, 3724 (1998)
- [48] E. Gornik, in *"Landau Level Spectroscopy"*, G. Landwehr (ed.) Elsevier (1991)
- [49] P.D. Buckle, J. W. Cockburn, M. S. Skolnick, R. Grey, G. Hill, and M. A. Pate, *Phys. Rev. B* **53**, 13651 (1996)
- [50] D. Bertram, K. v. Klitzing, O. Kuhn, D. K. Maude, J. C. Portal, H. T. Grahn, and K. H. Ploog, *Phys. Rev. B* **56**, R7084 (1997)
- [51] H. T. Grahn, *Physica Scripta T* **49**, 507 (1993)
- [52] T. H. Sander, S. N. Holmes, J. J. Harris, D. K. Maude, and J. C. Portal, *Phys. Rev. B* **58**, 13856 (1998)

- [53] M. E. Raikh, T. V. Shahbazyan, *Phys. Rev. B* **49**, 5531 (1994)
- [54] M. Rochat, J. Faist, M. Beck, U. Oesterle, *Physica E* **7**, 44 (2000)
- [55] P. Kinsler, P. Harrison, and R. W. Kelsall, *Phys. Rev. B* **58**, 4771 (1998)
- [56] K. Kempa, Y. Zhou, J. R. Engelbrecht, P. Bakshi, H. I. Ha, J. Moser, M. J. Naughton, J. Ulrich, G. Strasser, E. Gornik, and K. Unterrainer *Phys. Rev. Lett.* **88**, 226803 (2002)
- [57] K. Kempa, E. Gornik, K. Unterrainer, M. Kast, and G. Strasser, *Phys. Rev. Lett.* **86**, 2850 (2001)
- [58] Das Sarma, *Phys. Rev. Lett.* **52**, 859 (1984)
- [59] H. Drexler, J.S. Scott, S. J. Allen, K. L. Campman, and A. C. Gossard, *Appl. Phys. Lett.* **67**, 2816 (1995)
- [60] C. Zhang, M. L. F. Lerch, A. D. Martin, P. E. Simmonds, and L. Eaves, *Phys. Rev. Lett.* **72**, 3397 (1994)
- [61] K. Kempa, D. A. Broido, C. Beckwith, and J. Cen, *Phys. Rev. B* **40**, 8385 (1989)
- [62] K. Kempa, P. Bakshi, J. Engelbrecht, Y. Zhou, *Phys. Rev. B* **61**, 11083 (2000)
- [63] A. C. Gossard, M. Sundaram, and P. F. Hopkins, *Epitaxial microstructures* ed A C Gossard, Boston: Academic 153 (1994).
- [64] K. D. Maranowski, and A. C. Gossard, *J. Appl. Phys.* **88**, 172 (2000)
- [65] B. C. Smith, *Fourier Transform Infrared Spectroscopy*, CRC Press, Boca Raton (1996).
- [66] M. Coquelin et al. to be published